

Microtubule mechanics and the implications for their assembly



Von der Fakultät für Physik und Geowissenschaften
der Universität Leipzig
genehmigte

DISSERTATION

zur Erlangung des akademischen Grades

doctor rerum naturalium
Dr. rer. nat

vorgelegt von

M.Sc. Katja Marie Taute

geboren am 4. Mai 1982 in Westerstede

Gutachter: Prof. Dr. Josef Käs
Prof. Dr. Marileen Dogterom

Tag der Verleihung: 2. Mai 2012

Microtubule mechanics and the implications for their assembly

Katja Marie Taute

Thesis Advisor: Prof. Dr. Josef Käs

Katja M. Taute

Education

10/2001 - 12/2006	International Physics Studies Program, University of Leipzig. Intermediate Examinations, grade 1.0, 2003. Master of Science in Physics, with Distinction, grade 1.0, 8.12.2006.
02/2004 - 12/2004	Graduate Studies at the University of Canterbury, Christchurch, New Zealand. Postgraduate Diploma with Distinction in Physics, 2005.
06/2008 - 08/2008	Physiology Course, Marine Biology Laboratory, Woods Hole, MA, USA.
07/2007 - 05/2012	Pursuing Dr. rer. nat. in Physics, University of Leipzig.

Research Experience

03/2004 - 09/2004	Astrophysics research at the Department of Physics & Astronomy, University of Canterbury, Christchurch, New Zealand.
10/2003 - 01/2004	Lab experience at the Active Polymer Networks Group, University of Leipzig.
04/2006	Visitor at the European Molecular Biology Laboratory, Heidelberg.
05/2006 - 05/2011	Biophysics research at the Center for Nonlinear Dynamics, University of Texas at Austin, USA.

Scholarships

02/2004 - 12/2004	DAAD fellowship for studies at the University of Canterbury, Christchurch, New Zealand.
02/2004 - 12/2006	Fellow of the Studienstiftung des Deutschen Volkes.
07/2007 - 07/2009	Daimler-Benz Foundation Doctoral Fellowship for research at the University of Texas at Austin, USA.
07/2008	The Bruce and Betty Alberts Endowed Scholarship in Physiology.
07/2008	The Mountain Memorial Scholarship.

To my teachers

Herbert Niemeyer
‡ *Prof. Dr. Herbert Schmiedel*

Abstract

Microtubules are cytoskeletal protein polymers relevant to a wide range of cell functions. In order to polymerize, the constituent tubulin subunits need to bind the nucleotide GTP, but its subsequent hydrolysis to GDP in the microtubule lattice induces depolymerization. The resulting behaviour of stochastic switching between growth and shrinkage is called dynamic instability. Both dynamic instability and microtubule mechanical properties are integral to many cell functions, yet are poorly understood.

The present study uses thermal fluctuation measurements of grafted microtubules with different nucleotide contents to extract stiffnesses, relaxation times, and drag coefficients with an unprecedented precision. Both the stiffness and the relaxation time data indicate that stiffness is a function of length for GDP microtubules stabilized with the chemotherapy drug taxol. By contrast, measurements on microtubules polymerized with the non-hydrolyzable GTP-analogue GMPCPP show a significantly higher, but constant, stiffness. The addition of taxol is shown to not significantly affect the properties of these microtubules, but a lowering of the GMPCPP content restores the length-dependent stiffness seen for taxol microtubules.

The data are interpreted on the basis of a recent biopolymer model that takes into account the anisotropic architecture of microtubules which consist of loosely coupled protofilaments arranged in a tube. Using taxol microtubules and GMPCPP microtubules as the respective analogues of the GDP and GTP state of microtubules, evidence is presented that shear coupling between neighbouring protofilaments is at least two orders of magnitude stiffer in the GTP state than in the GDP state. Previous studies of nucleotide effects on tubulin have focussed on protofilament bending, and the present study is the first to be able to show a dramatic effect on interprotofilament bonds. The finding's profound implications for dynamic instability are discussed.

In addition, internal friction is found to dominate over hydrodynamic drag for microtubules shorter than $\sim 4\text{ }\mu\text{m}$ and, like stiffness, to be affected by the bound nucleotide, but not by taxol.

Furthermore, the thermal shape fluctuations of free microtubules are imaged, and the intrinsic curvatures of microtubules are shown for the first time to follow a spectrum reminiscent of thermal bending. Regarding the extraction of mechanical data, this assay, though previously described in the literature, is shown to suffer from systematic flaws.

Acknowledgements

Many people were of invaluable help in the completion of this work.

Foremost, I am indebted to my advisor Prof. Dr. Josef Käs for backing me in my decision to conduct my doctoral research at the Center for Nonlinear Dynamics at The University of Texas at Austin in the US.

There, I have enjoyed the support of my mentor Prof. Dr. Ernst-Ludwig Florin and the Biophysics Groups. I am grateful to Prof. Florin for giving me a lot of freedom in my work as well as the room to grow in the face of challenges while offering valuable advice as well as a brilliant motivational scheme. I have enjoyed working in the Florin Group and recall countless lively debates both in the lab and at the Spiderhouse.

In addition, I am grateful to Dr. Francesco Pampaloni, now at the Frankfurt Institute for Molecular Life Sciences, for first introducing me to microtubule mechanics assays, and to Prof. Dr. Ken Johnson of the Institute for Cell and Molecular Biology at UT Austin as well as Prof. Dr. Tim Mitchison of Harvard Medical School for helpful advice on microtubule biochemistry. In addition, I have also benefited from discussions with Prof. Dr. Erwin Frey of the Ludwig Maximilians University in Munich.

Furthermore, I would like to acknowledge two teachers who were very influential in my physics education. Herbert Niemeyer at the Gymnasium Westerstede, with his emphasis on logical reasoning rather than computation, helped me in developing the mindset of a physicist. At the University of Leipzig, my experimental physics teacher Prof. Dr. Herbert Schmiedel was a source of inspiration in his rare combination of an impressive intellect and kind patience.

The greatest thanks is owed to my partner Stuart for his love and support despite my long nights at the lab and his long commutes across continents. Thank you also to the Astrovolley team in Austin for providing a welcome distraction.

I am grateful to the German National Academic Foundation for supporting me in my first move to The University of Texas at Austin, and the Gottlieb Daimler and Karl Benz Foundation for awarding me a doctoral fellowship. Additional funding was provided by the National Science Foundation in the form of the grants CMMI-0728166 and CMMI-1031106. The author gratefully acknowledges the use of ImageJ [1], Gimp, and VMD [2].

Contents

Figures	xiii
Tables	xv
1 Introduction and overview	1
1.1 Thesis outline	1
1.2 Microtubules	2
1.2.1 Relevance	2
1.2.2 Architecture	5
1.3 Microtubule mechanics	9
1.3.1 Relevance of microtubule mechanical properties	9
1.3.2 Theory of semiflexible polymers	10
1.3.3 Previous experimental work	17
2 Experimental procedures	20
2.1 Thermal fluctuation measurements on grafted microtubules	20
2.1.1 Assay	20
2.1.2 Microtubule polymerization	21
2.1.3 Sample preparation	24
2.1.4 Instrumentation	27
2.1.5 Recordings	27
2.2 Thermal fluctuation measurements on free microtubules	28
2.2.1 Microtubule polymerization	28
2.2.2 Sample preparation	29
2.2.3 Microscopy	31
3 Data analysis	34
3.1 Error sources in time series measurements	34
3.1.1 Low-pass filtering corrections	34
3.1.2 Correlated measurements	37
3.1.3 Measurement errors	39
3.1.4 Drift	40
3.2 Measurements on grafted filaments	40
3.2.1 Single particle tracking	40
3.2.2 Extraction of mechanical parameters	41
3.3 Measurements on free filaments	44

3.3.1	Microtubule shape tracking	44
3.3.2	Mode amplitude extraction	44
3.3.3	Extracting mechanical parameters	47
4	Results and Discussion	53
4.1	Grafted microtubules	53
4.1.1	Taxol microtubules	53
4.1.2	GMPCPP microtubules	66
4.1.3	Mixed nucleotide microtubules	72
4.1.4	An interpretation based on the Wormlike Bundle Model	76
4.1.5	Mechanical and architectural heterogeneity	83
4.1.6	Consistency checks	86
4.2	Free microtubules	91
4.2.1	Intrinsic shapes	91
4.2.2	Stiffness estimates	94
4.2.3	Relaxation times	98
4.2.4	Drag coefficients	98
4.3	Comparison of the two approaches	101
5	Conclusions and outlook	103
5.1	Summary	103
5.2	Conclusions	105
5.3	Outlook	106
	References	107
A	Reagents	117

Figures

1.1	The cytoskeleton	3
1.2	Microtubules in cell division	3
1.3	Motor proteins	3
1.4	Cilia in the human oviduct	3
1.5	Microtubule organization in different organisms	4
1.6	Microtubule molecular architecture	6
1.7	Microtubule growth and shrinkage	7
1.8	Microtubule doublets and triplets	9
1.9	Wormlike Chain Model	11
1.10	Shape fluctuation modes	13
1.11	MSD for grafted filament	17
2.1	Assay for experiments on grafted microtubules	20
2.2	Sample chamber	25
2.3	Microtubule attached to substrate	28
2.4	Assay for experiments on free microtubules	29
2.5	APTES	30
2.6	mPEG-SVA	31
2.7	Shutter lag time diagram	32
2.8	Shutter lag time measurement	32
3.1	Low-pass filtering	34
3.2	Blur factor S	36
3.3	Low-pass filtered MSD	37
3.4	Experimental position distribution	42
3.5	Example MSD	43
3.6	Shape tracking procedure	45
3.7	Mode decomposition	46
3.8	Amplitude variances	47
3.9	Mode amplitude MSDs	50
3.10	Persistence length corrections	51
4.1	Stiffness of taxol microtubules	54
4.2	Stiffness of taxol microtubules	55
4.3	Monte Carlo simulation of undersampling	56
4.4	Wormlike Bundle Model	58

4.5	Bending stiffness in the WLB model	60
4.6	Parameter dependence of WLB stiffness	62
4.7	Relaxation times of taxol microtubules	63
4.8	Two regimes for taxol microtubule relaxation times	64
4.9	Friction contributions for taxol microtubules	65
4.10	Stiffness of GMPCPP microtubules	67
4.11	Stiffness of taxol GMPCPP microtubules	69
4.12	Relaxation times for GMPCPP microtubules	71
4.13	Drag coefficients for GMPCPP microtubules	72
4.14	Drag coefficients for GMPCPP/taxol microtubules	73
4.15	Stiffness estimates for different nucleotide contents	75
4.16	Drag estimates for different nucleotide contents	76
4.17	Nucleotide effects on microtubule stiffness	79
4.18	Catastrophe	80
4.19	Molecular representation of the tubulin dimer	81
4.20	Microtubule with two attached beads	87
4.21	Persistence length estimates from different eigenmode models	87
4.22	1 st and 2 nd mode MSD fits	88
4.23	2 nd mode stiffness	89
4.24	1 st and 2 nd mode drag coefficients	90
4.25	Intrinsic shape	91
4.26	Rotating vs. nonrotating microtubules	92
4.27	Intrinsic microtubule shape spectrum	93
4.28	Stiffness estimates from free and grafted microtubules	95
4.29	Stiffness estimates by batch and sample	96
4.30	Relaxation times for free microtubules	98
4.31	Relaxation times by sample	99
4.32	Drag for free and grafted microtubules	100
4.33	Drag estimates by batch and sample	100

Tables

1.1	Microtubule supertwist	9
1.2	Previous experimental results	18
4.1	Stiffness statistics for GMPCPP lots	68
4.2	Stiffness of GMPCPP microtubules with taxol	70
4.3	Comparison of the two techniques	102
A.1	Reagents	118

Chapter 1

Introduction and overview

1.1 Thesis outline

Microtubules are cytoskeletal filaments that are a prime target of chemotherapy drugs due to their role in cell division. Despite being integral to this cell function, microtubule mechanics as well as their assembly properties are still poorly understood even after decades of research directed at the problem.

This thesis presents mechanical measurements of unprecedented precision which reveal a range of hitherto unseen features of microtubule mechanical properties with profound implications for an understanding of microtubule assembly.

The data are obtained using an elegant assay which harnesses the thermal fluctuations of microtubules for the extraction of mechanical parameters. Thermal fluctuations not only continue to be a subject of research [3], but can also be used as a tool (see Ref. [4] for a review). Information on mechanical properties is deduced from both the equilibrium and the dynamic properties of the thermal fluctuations of grafted and free microtubules. While the results for free microtubules are shown to suffer from artefacts although mirroring procedures previously used in the literature, the results for grafted microtubules are shown to be reliable by a range of consistency checks.

The results support the notion that the stiffness of microtubules is a function of microtubule length, and are interpreted on the basis of the Wormlike Bundle Model [5, 6]. This new biopolymer mechanical model predicts a length-dependent effective stiffness as a result of the anisotropic protofilament architecture of microtubules. The model is then applied to the interpretation of mechanical data obtained for microtubules of varying chemical conditions. Specifically, the effect of the bound nucleotide is studied by comparison of microtubules with modified nucleotide contents.

The binding of the nucleotide GTP and its hydrolysis to GDP regulates the stochastic growth and shrinkage of microtubules in a process called dynamic instability. Dynamic instability is so integral to cell division that a common anti-mitotic chemotherapy drug, taxol, functions solely by sabotaging this process. Despite decades of research, the mechanisms underly-

ing nucleotide-regulated microtubule assembly and disassembly as well as their stabilization by taxol are still not completely understood. This thesis presents a novel approach to studying the problem by utilizing mechanical data of microtubules polymerized with different nucleotide and taxol contents to draw conclusions with respect to the effects of these agents on the molecular interactions in the microtubule lattice.

The conclusions for the first time identify a major change in the lateral interactions between protofilaments as a result of the bound nucleotide. These parts of the microtubule lattice have so far been very difficult to access by other experimental means and, as a result, have been neglected in the quest for an understanding of microtubule dynamic instability. The results of this thesis hence give rise to a novel perspective on how microtubule assembly is regulated.

1.2 Microtubules

1.2.1 Relevance

Cells owe a large part of their mechanical integrity and biological functionality to a set of filaments called the cytoskeleton. Key members of the eukaryotic cytoskeleton are microtubules, actin, and intermediate filaments. Each of these types of filaments are polymers that self-assemble from specific proteins, and have distinct physical properties and roles in the cell. Fig. 1.1 shows an image of a typical animal cell with microtubules and actin filaments marked by fluorescent labels.

Intermediate filaments are very soft with persistence lengths on the order of $1\text{ }\mu\text{m}$ [8] and are considered to be supplying tensile strength to cells [9]. Actin filaments are somewhat stiffer with a persistence length of $17\text{ }\mu\text{m}$ [10, 11], and are involved in cell motility and intracellular transport [9]. Microtubules in turn are about 2 orders of magnitude stiffer and fulfil a wide range of different functions in different cells.

In all eukaryotic cells, microtubules are involved in cell division. Together with many auxiliary proteins, they form a structure called the mitotic spindle which is tasked with the arrangement of chromosome doublets on the division plane and their subsequent segregation into the two daughter cells [9]. Fig. 1.2 shows a fluorescence microscopy image of the mitotic spindle. It is this involvement in cell division that makes microtubules a major target for chemotherapy drugs such as Taxol (paclitaxel) and the epothilones [12].

In addition, microtubules form tracks for motor proteins to travel on. These molecular motors bind cargo and transport it over long distances using the microtubule network inside the cell [9]. Active transport is necessary

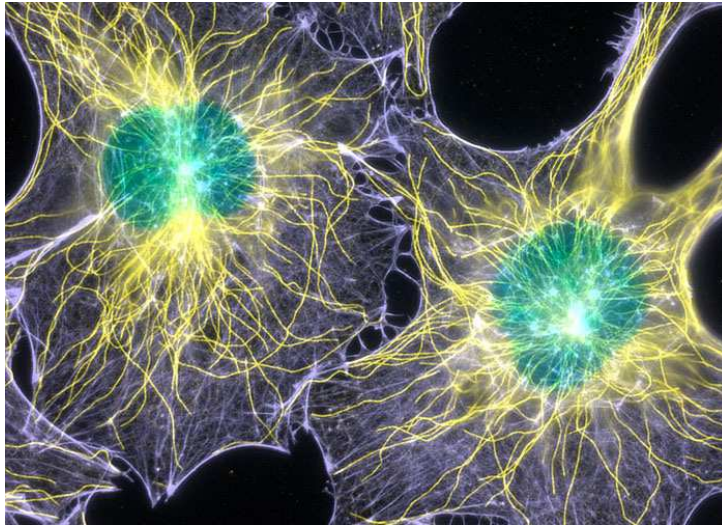


Figure 1.1: This fluorescence image of mouse fibroblast cells (from Ref. [7]) shows the nuclei in blue, microtubules in yellow and actin filaments in purple. Microtubules radiate out from a microtubule organization centre close to the nucleus, while a network of actin filaments spans the entirety of the cell.

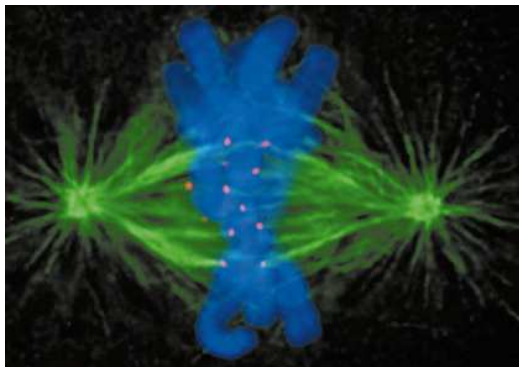


Figure 1.2: A fluorescence image of a vertebrate cell undergoing cell division, or mitosis (from Ref. [13]). Microtubules (green) form the mitotic spindle and bind the duplicated chromosomes (blue) at their kinetochores (pink). Once all chromosomes are bound, the sister chromatids are separated and pulled towards the respective spindle poles [9].

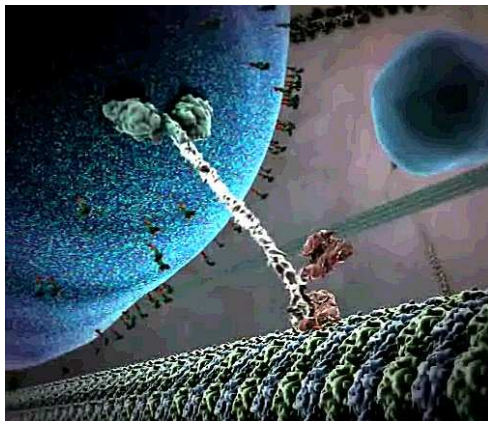


Figure 1.3: A cartoon of the motor protein kinesin walking along the surface of a microtubule (bottom) while pulling a vesicle payload (top). The image is a still from Ref. [14].

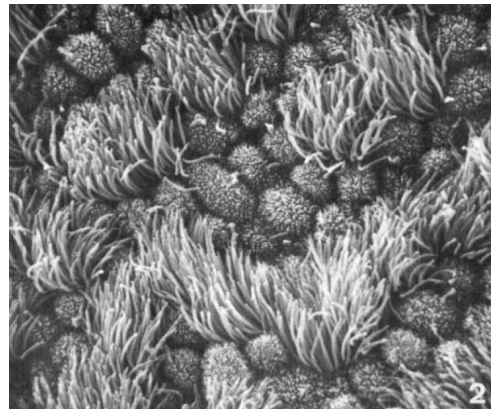


Figure 1.4: A scanning electron micrograph of ciliated cells in the human oviduct (from Ref. [15]). The cilia beating in a coherent pattern are thought to transport the egg to the uterus.

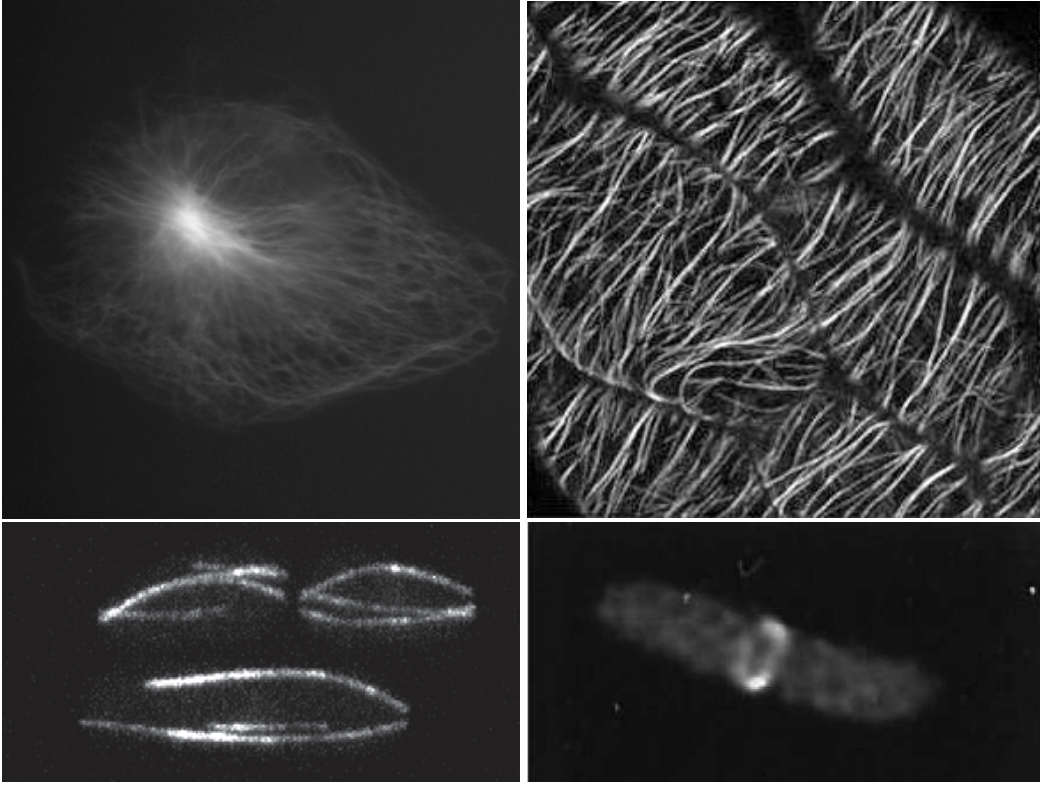


Figure 1.5: Microtubule organization in different biological kingdoms. Fluorescently labeled tubulin or its homologues in the cytoskeleton of an animal cell (top left, from Ref. [16]), a plant cell (top right, from Ref. [17]), a fission yeast cell (bottom left, from Ref. [18]), and a bacterial cell (bottom right, from Ref. [19]). Microtubules are radiating outward from a microtubule organization center close to the nucleus in the animal cell, but in the plant cell, they are arranged along the cell cortex. In animal and plant cells, the microtubules are numerous while in yeast cells they are generally limited to two bundles which are attached to the nucleus. In the bacterium *E. coli*, the tubulin homolog FtsZ forms a contractile ring during cytokinesis, the process in which the daughter cells separate at the end of cell division [20]. Length scales are decreasing from tens of microns in the animal cell to a couple of microns in the bacterial cell.

on length scales where simple diffusion would take too long, that is longer than a few micrometers. In neurons, microtubules support the transport of neurotransmitters along axons over distances of up to ~ 1 m. Two main classes of motor proteins travelling on microtubules are known: kinesin and dynein, and they preferentially travel in opposite directions. Fig. 1.3 shows a cartoon of a kinesin motor protein in action.

Microtubules in conjunction with dynein motor proteins also form the core structures of motile cellular appendages such as cilia and eukaryotic flagella which lend motility to microorganisms such as *Tetrahymena* as well as sperm,

and which enable stationary cells to move fluid around them [21]. The latter is relevant for instance for cells clearing the human respiratory tract, for the establishment of left-right asymmetry in human development [22], and for the transport of egg cells in the oviduct (see Fig. 1.4) [15].

Furthermore, microtubules have recently been found to be involved in the establishment and maintenance of polarity in epithelial cells and others [23], and continue to be discovered to be relevant for a multitude of other cell functions. It is of interest to note that the multitude of processes mentioned above only represents our current knowledge about microtubules in animal cells. Tubulin and its homologues are however widely conserved among all species and its cellular tasks may vary widely. As an example, Fig. 1.5 contrasts the organization of tubulin filaments in animal, plant, fungal and bacterial cells. Even bacteria are now known to possess homologues of tubulin and other cytoskeletal proteins [20], and their properties and tasks are a current subject of study.

1.2.2 Architecture

Helix structure

The molecular architecture of microtubules is described in their name: they truly are microscopic tubes. Their building blocks are the globular proteins α - and β -tubulin with a diameter of about 4 nm each. Together, they form a heterodimer that is inseparable. Dimers can assemble longitudinally into so-called protofilaments, which are arranged in parallel to form a tube with a diameter of approximately 25 nm. As they are slightly offset from one another, the polymer has an intrinsic left-handed helicity with respect to the arrangement of like monomers around the circumference of the microtubule. Most commonly, 13 protofilaments are arranged in a 3-start helix as shown in Fig. 1.6.

Dynamic Instability

Both the α - and the β -tubulin monomer are capable of binding the nucleotide guanosine triphosphate (GTP), but while a GTP molecule bound to the α -monomer is essentially irreversibly bound, the GTP bound to the β -monomer is exchangeable as long as the dimer is free in solution.

In order to be able to form a polymer, both monomers need to have bound a molecule of GTP. Microtubules can grow on either end, but the end with the exposed β -tubulin monomers, called the $+$ -end, generally grows significantly faster. Once a dimer is incorporated into the microtubule lattice, the

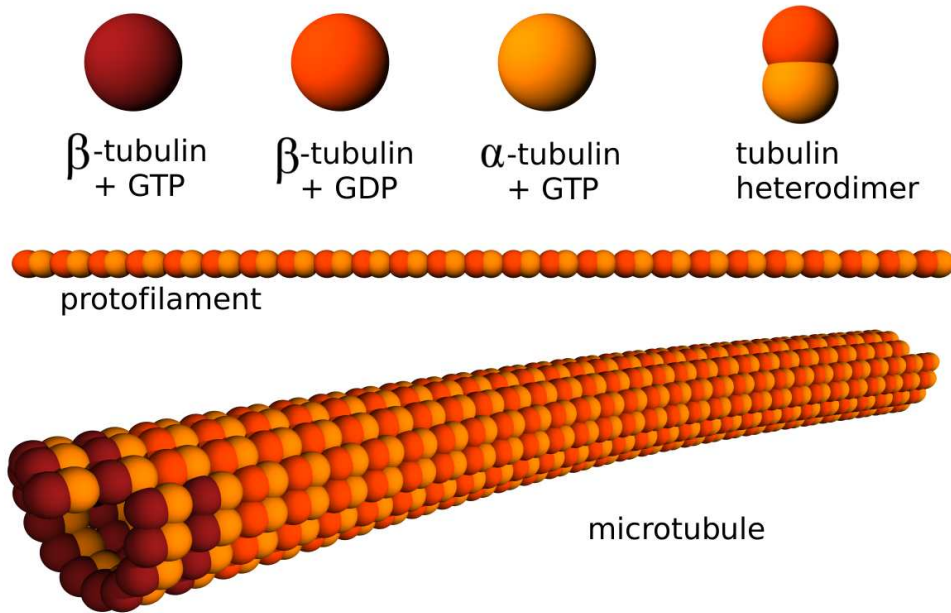


Figure 1.6: Microtubule molecular architecture. Protofilaments consist of chains of tubulin dimers and are arranged in parallel, but slightly offset from each other, in a microtubule. Polymerization occurs primarily at the $+$ -end (left) and requires GTP to be bound to the β -monomer. Shortly after incorporation into the microtubule, the GTP is hydrolyzed to GDP. The GDP microtubule lattice is not stable, requiring a GTP cap at the $+$ -end to prevent depolymerization. A GTP cap can only be maintained by constant addition of GTP subunits.

GTP bound to the β -monomer is quickly hydrolyzed to guanosine diphosphate (GDP). The lattice formed by dimers with GDP-bound β -tubulin is unstable and prone to undergo spontaneous depolymerization in a process termed catastrophe. It can however be stabilized by constant addition of further GTP dimers, maintaining a so-called GTP cap that prevents the polymer from falling apart. Once hydrolysis catches up with polymerization, the GTP cap is eliminated and the polymer shrinks rapidly. Electron microscopy images of depolymerizing microtubules often show characteristic ram's horns at the end, with the protofilaments curling outwards away from each other [24, 25, 26].

Fig. 1.7 shows a cartoon of microtubule growth and shrinkage. Shrinkage continues until either the microtubule has disappeared entirely or it is halted

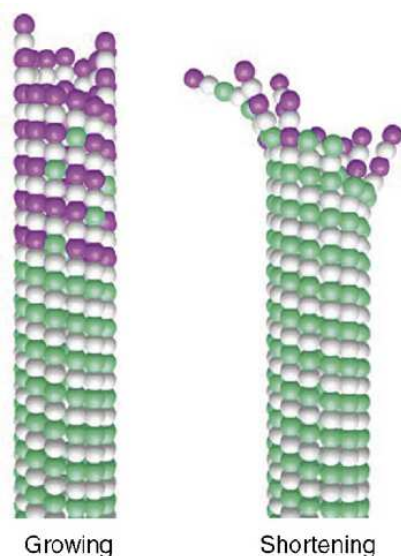


Figure 1.7: Model of microtubule growth and shrinkage (from Ref. [27]). During growth, GTP-bound units (purple) are added to the tip of the microtubule. Sometime after incorporation, the GTP is hydrolyzed to GDP (green). If there is not a sufficient cap of GTP units at the tip of the microtubule, depolymerization begins.

in an event termed rescue. Rescues are poorly understood but are generally thought to be caused by GTP dimer remnants in the lattice that failed to undergo hydrolysis for unknown reasons [28]. This resulting behaviour of stochastic growth and shrinkage has been termed dynamic instability [29] and is a key requirement for many cellular processes that microtubules are involved in (see Ref. [30] for a review). The chemotherapy drugs taxol and epothilone both prevent microtubules from depolymerizing, thereby hindering their participation in the process of cell division.

Nevertheless, the process of dynamic instability and the role of the bound nucleotide in its regulation are still a subject of intense study and debate. For example, the size and nature of the hypothesized stabilizing cap is still an open question, with some studies favouring an intermediate hydrolyzation state termed GDP-Pi rather than GTP as the main component [31].

The role of the bound nucleotide

Various approaches have been pursued in order to gain information on the regulation of microtubule assembly by nucleotides, but progress has been limited due to a number of experimental difficulties.

Biochemical studies [32, 33] are hampered by their limited time resolution and the fact that they measure bulk averages rather than the dynamics of individual molecules. Single molecule studies [34, 35] have recently started to observe microtubule assembly at the molecular level by observing the displacement of a microtubule growing against a barrier, but as yet cannot resolve submolecular conformational changes.

Electron microscopy [36] studies can resolve microtubules, but the resolution is limited and can only be improved by averaging based on the helical symmetry of microtubules as well as computational docking of high resolution diffraction structures. High resolution diffraction studies [37] have only been possible on select artificial structures that are able to form crystals but have dimer contacts that are not necessarily representative of those in the microtubule lattice. In addition, diffraction studies only provide a map of electron density rather than information on the strength of interactions in the structure.

Variations in microtubule architecture

In vivo, microtubule architecture appears to be tightly controlled. This control is probably partly achieved by the use of a template as a nucleation site. In most animal and plant cells, the result is a 13 protofilament [38], 3-start helix. There are however some startling exceptions. While most cells in the worm *C. elegans* exclusively make 11-protofilament microtubules, a class of neurons specialized on touch sensing use arrays of 15-protofilament microtubules [39]. Wing cells in the fruit fly *Drosophila* also use 15-protofilament microtubules during a specific developmental stage. Several other known examples are mentioned in Ref. [40]. Some organelles such as cilia contain intricate arrangements of microtubule doublets and triplets as shown in Fig. 1.8 [41], and even more complex structures have been documented to exist, for instance the conoid fibres in the parasite *Toxoplasma gondii* which seem to be woven from comma-shaped arrangements of protofilaments [42].

In contrast, microtubules grown in vitro from purified tubulin tend to grow in a variety of different architectures. Under typical polymerization conditions, protofilament numbers anywhere between 8 and 19 have been observed ([43] and references therein) as well as transitions in protofilament number along one microtubule, called lattice defects [44]. Different growth conditions have been reported to bias the distribution of protofilaments in certain ways [44].

While for a 13-protofilament microtubule, the protofilaments are straight and parallel to the microtubule axis, different protofilament numbers force the microtubule lattice into a supertwist in order to maintain similar lateral contacts. This supertwist means that protofilaments follow a helical path around the microtubule axis. Table 1.1 shows predicted values for this supertwist.

In addition to these findings, different chemical conditions have been shown to influence not just the number of protofilaments, but also the subunit spacing along the protofilaments, and as a consequence the lattice supertwist.



Figure 1.8: Electron micrograph of microtubule doublets and triplets in cross sections of the cilia of the flagellated protozoan *Pseudotrypanosoma* (from Fig. 20 in Ref. [41]). The structures vary dependent on the position from the base of the cilium. Dynein motor proteins interconnect the doublets and self-organize into a beating pattern.

PF number	helix start	pitch (μm)
8	2	-2.76
9	2	6.98
10	2	2.15
11	3	-1.74
12	3	-4.14
13	3	-
14	3	5.63
15	3	-3.23
16	4	-5.52
17	4	-24.91
18	4	13.96
19	4	6.22

Table 1.1: Theoretical microtubule supertwist parameters as presented in Ref. [45]. Only microtubules with 13 protofilaments are expected to have no supertwist.

Both taxol [46] and the GTP-analogue GMPCPP [47] were found to increase the subunits spacing, but by different, albeit small, amounts.

1.3 Microtubule mechanics

1.3.1 Relevance of microtubule mechanical properties

Many of the biological functions of microtubules pose requirements on their mechanical properties. For instance, a very soft filament would not be able to establish and maintain a direction of polarization inside a cell. On the

other hand, a very stiff filament would fail to find a chromosome in cell division. In order to find a kinetochore, microtubules in the mitotic spindle need to sample space through the use of both dynamic instability and thermal fluctuations. The width of the latter depends inversely on the stiffness. Furthermore, pushing and pulling forces transmitted through microtubules are of key importance for the positioning of organelles inside the cell [48].

Satisfying mechanical requirements for vastly different sets of cell functions on varying spatial scales poses obvious challenges. The combination of tight control and high specialization seen for the molecular architecture of microtubules suggests that this structure provides an advantage towards meeting these requirements.

Not surprisingly, for all above reasons, the mechanical properties of microtubules have been the subject of scientific studies for the past three decades.

1.3.2 Theory of semiflexible polymers

The Wormlike Chain Model

Many synthetic polymers are very soft and can hence be described as freely jointed chains. In contrast, many biological polymers and especially members of the cytoskeleton are quite stiff and show correlations length l_p on the order of their contour length L or even longer. Such filaments are referred to as semiflexible, and have often been successfully described by the so-called Wormlike Chain Model [49, 50, 51]. This model derives from linear elasticity theory applied to the bending of a slender filament with a length much longer than its thickness. Fig. 1.9 shows a sketch. The resulting bending energy is proportional to the square of the curvature, integrated along the length of the filament:

$$E_b = \frac{\kappa}{2} \int_0^L ds \left(\frac{\partial^2 \vec{r}(s)}{\partial s^2} \right)^2, \quad (1.1)$$

where $s \in [0, L]$ is the arc length marking the position along the polymer contour and κ is a material parameter called the flexural rigidity or bending stiffness. If the filament consists of a homogeneous and isotropic material with Young's modulus E , then

$$\kappa = EI, \quad (1.2)$$

where I refers to the second area moment of the filament's cross section, defined as

$$I = \int_A d^2dA \quad (1.3)$$

with d being the distance to the axis about which the filament is bent, and the integral being over the cross section A . For a tubular cross section, as appropriate in the case of microtubules, the result is

$$I = \pi (R_{\text{outer}}^4 - R_{\text{inner}}^4) / 4, \quad (1.4)$$

with R_{outer} and R_{inner} referring to the outer and inner radii of the tube, respectively.

Assuming the filament to be inextensible, the tangent vector $\vec{t} = \frac{\partial \vec{r}(s)}{\partial s}$ has a fixed length:

$$|\vec{t}(s)| = 1. \quad (1.5)$$

When the filament is in a solution of temperature $T > 0$, the surrounding fluid molecules exert random thermal forces on the filament. As a result, its shape fluctuates. It can be shown that the tangent-tangent correlation function decays exponentially along the filament contour:

$$\langle \vec{t}(s) \cdot \vec{t}(s') \rangle = \exp \left(-\frac{|s - s'|}{l_p} \right). \quad (1.6)$$

The length scale set by l_p is called the persistence length of the polymer and is related to the bending stiffness κ via the temperature:

$$\kappa = l_p k_B T. \quad (1.7)$$

Shape fluctuation eigenmodes

In order to analytically describe the shape fluctuations of a semiflexible polymer in solution, a balance between elastic and drag forces needs to be con-

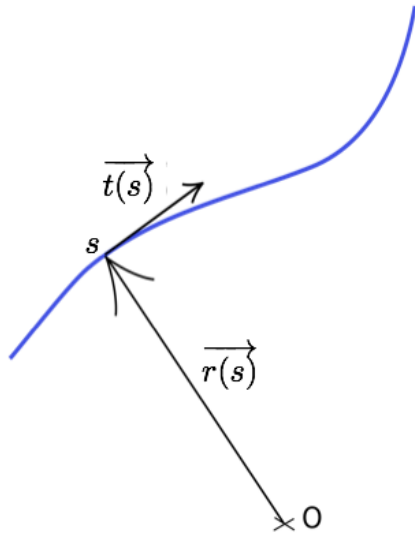


Figure 1.9: Parameters in the Wormlike Chain Model. The contour of a slender filament is parametrized in terms of the parameter s . $\vec{r}(s)$ is the position of the filament in space, and $\vec{t}(s)$ is the tangent vector.

sidered [52, 53]:

$$\kappa \frac{\partial^4 y}{\partial s^4} = -\zeta \frac{\partial y}{\partial t}. \quad (1.8)$$

Here $y(s, t)$ is the transverse deflection of the filament at position s and time t , and ζ denotes a drag coefficient that is normalized per unit length. This equation neglects inertia because the dynamics are completely overdamped: The drag forces are much larger than inertial contributions, and all movement occurs at low Reynold's numbers. In addition, this equation assumes that the polymer is stiff enough such that its bending angles are small [52, 51]. This is a reasonable assumption for microtubules where $l_p/L \approx 10^2$, but is less applicable to actin filaments where $L \sim l_p$. Separating the solution into a spatial and a temporal part:

$$y(s, t) = ay^s(s)y^t(t) \quad (1.9)$$

where a is a multiplicative factor corresponding to an amplitude, it follows that the temporal parts $y^t(t)$ must correspond to an exponential decay. For the spatial part $y^s(s)$, a set of countable orthogonal solutions $W_n(s)$, so-called modes, is given by superpositions of sine and cosine functions and their hyperbolic counterparts. Their composition and wave number is subject to a solvability condition determined by the boundary conditions.

Grafted Filament In the case of a grafted filament, the boundary conditions are

$$y|_{s=0} = 0 \quad (1.10)$$

$$\left. \frac{\partial y}{\partial s} \right|_{s=0} = 0 \quad (1.11)$$

$$\left. \frac{\partial^2 y}{\partial s^2} \right|_{s=L} = 0 \quad (1.12)$$

$$\left. \frac{\partial^3 y}{\partial s^3} \right|_{s=L} = 0. \quad (1.13)$$

These correspond to no fluctuations and a tangent of 0 at the grafted end, and neither forces nor torques at the free end. Inserting an ansatz of the type

$$W_n(s) = A \cos\left(q_n \frac{s}{L}\right) + B \sin\left(q_n \frac{s}{L}\right) + C \cosh\left(q_n \frac{s}{L}\right) + D \sinh\left(q_n \frac{s}{L}\right) \quad (1.14)$$

$$y_n(s) = a_n W_n(s), \quad (1.15)$$

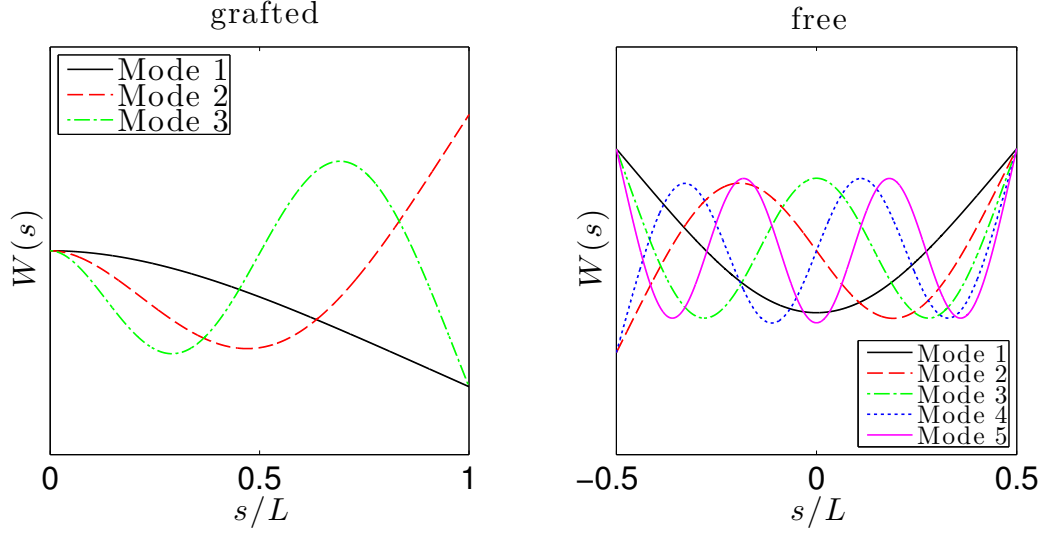


Figure 1.10: The shapes of the first few modes for grafted boundary conditions (left, see Eq. 1.17) and free ends (right, see Eq. 1.28). Note that the parameter s runs along the contour of the filament, it is not the cartesian coordinate along the axis of the filament. In practice, however, amplitudes for filaments as stiff as microtubules are typically so small that the distinction can be neglected.

where a_n is the amplitude for the n th mode, then yields the condition

$$\cos(q_n) \cosh(q_n) = -1 \quad (1.16)$$

for the mode numbers q_n . The solutions are $q_1 \approx 1.875$, $q_2 \approx 4.694$, $q_3 \approx 7.855$, and $q_n \approx (n - 1/2)\pi$ for higher modes. The shapes can be shown to take the form [54]

$$W_n(s) = \frac{-\cos(q_n) - \cosh(q_n)}{\sin(q_n) + \sinh(q_n)} \left(\sin\left(q_n \frac{s}{L}\right) - \sinh\left(q_n \frac{s}{L}\right) \right) + \cos\left(q_n \frac{s}{L}\right) - \cosh\left(q_n \frac{s}{L}\right) \quad (1.17)$$

Fig. 1.10 shows their approximate shapes. Any shape of the filament can then be written as

$$y(s, t) = \sum_n a_n(t) W_n(s). \quad (1.18)$$

In turn, the mode amplitudes can be recovered from any given shape $y(s, t)$ as [54]

$$a_n = \frac{1}{L} \int_0^L y(s, t) W_n(s) ds, \quad (1.19)$$

where the orthogonality of the modes has been made use of:

$$\int_0^L W_n(s)W_m(s)ds = L\delta_{n,m}. \quad (1.20)$$

Free filament For a free filament, it is more convenient to parametrize the contour length as $s \in [-L/2, L/2]$ in order to exploit the symmetry of the arrangement. The boundary conditions of no forces and torques at the ends read

$$\frac{\partial^2 y}{\partial s^2} \Big|_{s=L/2} = \frac{\partial^2 y}{\partial s^2} \Big|_{s=-L/2} = 0 \quad (1.21)$$

$$\frac{\partial^3 y}{\partial s^3} \Big|_{s=L/2} = \frac{\partial^3 y}{\partial s^3} \Big|_{s=-L/2} = 0. \quad (1.22)$$

$$(1.23)$$

The ansatz of

$$W_n(s) = \begin{cases} A \cos\left(q_n \frac{s}{L}\right) + B \cosh\left(q_n \frac{s}{L}\right) & \text{for even shapes} \\ C \sin\left(q_n \frac{s}{L}\right) + D \sinh\left(q_n \frac{s}{L}\right) & \text{for odd shapes} \end{cases} \quad (1.24)$$

yields the condition

$$\tan(q_n/2) = -\tanh(q_n/2) \quad \text{for } n = 1, 3, \dots \quad (1.25)$$

$$\tan(q_n/2) = \tanh(q_n/2) \quad \text{for } n = 2, 4, \dots \quad (1.26)$$

or

$$\cos(q_n) \cosh(q_n) = 1 \quad (1.27)$$

and the solutions [52]

$$W_n(s) = \begin{cases} \frac{\cos(q_n \frac{s}{L})}{\cos(q_n/2)} + \frac{\cosh(q_n \frac{s}{L})}{\cosh(q_n/2)} & \text{for } n = 1, 3, \dots \\ \frac{\sin(q_n \frac{s}{L})}{\sin(q_n/2)} + \frac{\sinh(q_n \frac{s}{L})}{\sinh(q_n/2)} & \text{for } n = 2, 4, \dots \end{cases}. \quad (1.28)$$

The modes numbers are $q_n \approx (n + 1/2)\pi$ and converge to this expression much faster than in the grafted case. For the first mode, $q_1 \approx 4.730$ while $1.5\pi \approx 4.712$. Fig. 1.10 shows the corresponding shapes.

Following a deformation, the different modes decay individually with a relaxation time of [52, 55, 53]:

$$\tau_n = \frac{\zeta L^4}{\kappa q_n^4}. \quad (1.29)$$

It follows that relaxation times decrease rapidly with the mode number: The second mode is already $(q_2/q_1)^4 \approx 40$ times faster than the first in the case of a grafted filament. For a free filament, the ratio is much less extreme with $(q_2/q_1)^4 \approx 7.6$. Note also that the first mode of a free filament is about as fast as the second mode for a grafted filament.

Alternative views It has also been argued [56] that the correct eigenmodes for a fluctuating filament are not the biharmonic modes, but just the harmonic modes. The reason is that the shapes of a filament could be viewed in terms of its tangent vector diffusing on a unit sphere. The diffusion equation, however, has harmonic eigenfunctions. While for equipartition arguments, any set of orthogonal functions can be used to describe the filaments shape, the dynamics will only be correctly described by the true eigenmodes. The experimental evidence will be weighed against this view in the Section 4.1.6.

Equipartition

Equipartition demands that every quadratic degree of freedom receive an average of $\frac{1}{2}k_B T$ of thermal energy. The degrees of freedom are the amplitudes of the modes. To show that the energy in Eq. 1.1 is indeed harmonic in the mode amplitudes, the explicit expressions for Eq. 1.18 can be inserted directly into Eq. 1.1. Evaluating the integral, while considering the orthogonality of the modes as well as the solvability conditions Eqs. 1.16 and 1.25, yields

$$E_b = \frac{\kappa}{2} \sum_n a_n^2 \frac{q_n^4}{L^3} \quad (1.30)$$

which is quadratic in the mode amplitudes a_n . Equipartition hence demands that

$$\sigma^2(a_n) = \frac{k_B T L^3}{\kappa q_n^4} = \frac{L^3}{l_p q_n^4}. \quad (1.31)$$

The transverse position variance at any point s along the contour hence is

$$\sigma^2(y(s)) = \sum_n \sigma^2(a_n) W_n^2(s) = \sum_n V_n(s) = \frac{s^3}{3l_p}, \quad (1.32)$$

where $V_n(s)$ refers to the position variance due to the n^{th} mode at position s .

All cross terms drop out because the modes are fluctuating independently of each other, $\langle a_n(t)a_m(t) \rangle \propto \delta_{n,m}$. For the grafted filament, this leads to

$$\sigma^2(y|_{s=L}) = \frac{L^3}{3l_p}, \quad (1.33)$$

an expression that has repeatedly surfaced in the literature [57, 58, 59].

Dynamic expressions

Common measures of the dynamical behaviour of a stochastic variable $x(t)$ are the autocorrelation function

$$A(t) = \left\langle (x(t'+t) - \langle x(t'') \rangle_{t''}) (x(t') - \langle x(t'') \rangle_{t''}) \right\rangle_{t'} = \langle x(t'+t)x(t') \rangle_{t'} - \langle x(t') \rangle_{t'}^2 \quad (1.34)$$

and the mean square displacement

$$\text{MSD}(t) = \langle (x(t' + t) - x(t'))^2 \rangle_{t'}. \quad (1.35)$$

The two are related:

$$\text{MSD}(t) = 2\sigma^2(x) - 2A(t), \quad (1.36)$$

where $\sigma^2(x)$ is the variance of x .

Eq. 1.30 is a harmonic function of the mode amplitudes a_n . Their fluctuations can hence be described as random walks in harmonic potentials, completely analogous to more common scenarios such as the diffusion of a particle in an optical trap.

Each mode has its own characteristic correlation time τ_n [52, 53]:

$$A_{a_n}(t) = \sigma^2(a_n)e^{-t/\tau_n} = \frac{L^3}{q_n^4 l_p} e^{-t/\tau_n}. \quad (1.37)$$

The transverse position autocorrelation at position s along the contour then becomes

$$A_{y(s)}(t) = \sum_n A_{a_n}(t) W_n^2(s) = \sum_n \frac{L^3}{q_n^4 l_p} e^{-t/\tau_n} W_n^2(s). \quad (1.38)$$

Similarly, the transverse position MSD is

$$\text{MSD}_{y(s)}(t) = \sum_n \text{MSD}_{a_n}(t) W_n^2(s) = \sum_n \frac{2L^3}{q_n^4 l_p} W_n^2(s) (1 - e^{-t/\tau_n}). \quad (1.39)$$

Fig. 1.11 shows a plot of this equation and its mode contributions for one position along a grafted filament.

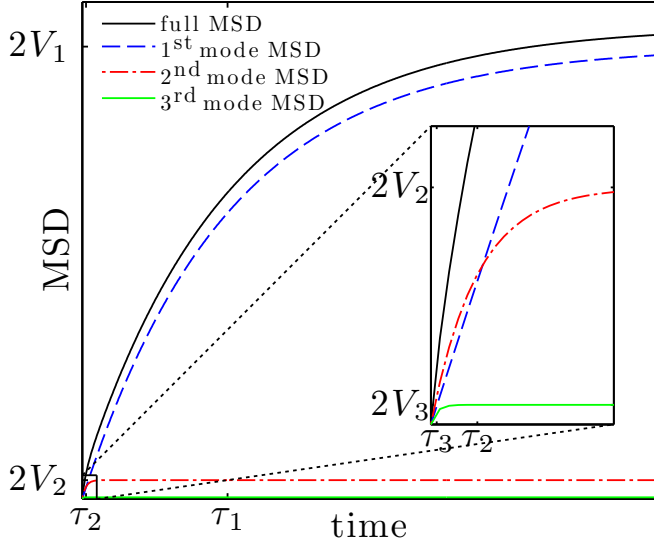


Figure 1.11: Transverse position MSD for a grafted filament at position $s = 0.6L$ [60]. V_n refers to the position variance due to the n^{th} mode (Eq. 1.39). The first mode dominates the MSD, and the higher modes only contribute minor corrections. Because they saturate at short timescales, they effectively only offset the total MSD from the first mode MSD. At positions $s \ll L$, the higher modes have a higher relative contribution.

1.3.3 Previous experimental work

In order to measure microtubules stiffness, a deformation has to be imposed on the microtubule and its response measured. The force causing the deformation could either be an active source such as an optical trap, or the random forces of thermal fluctuations. While active methods require a well-calibrated force and need to impart large deformations in order to dominate over thermal fluctuations, the use of the inevitably present thermal fluctuations themselves elegantly does away with the need for either. Both avenues have been pursued to obtain stiffness estimates, though with varying success. Table 1.2 shows an overview of some of the previous results.

The first studies of microtubule stiffness [61, 62] attempted to extract information from statistical analyses of the end-to-end distances R of microtubules free in solution or stuck to coverslips, and yielded results that seem astonishingly small compared to later studies. Because microtubules are very stiff, R is expected to be very similar to the filament length L , requiring very high measurement precision. Given that the width of the thermal fluctuations in R they measured seem independent of the length of the filaments, it seems likely that these authors measured mostly noise.

The remaining data, however, still show a very large scatter of results of approximately two orders of magnitude. One explanation that has been suggested [54] is that the stiffness depends on the speed at which the microtubules were grown. Janson & Dogterom [54] found evidence that faster grown microtubules are softer.

In addition, microtubule stiffness depends strongly on biochemical varia-

source	method	conditions	L (μ)	l_p (mm)	κ (10^{-24} Nm ²)
[61]	T	U	12-24	0.051 ± 0.021	$2.1 \pm 0.9^*$
[62]	T	U	5-23	0.074 ± 0.009	$3.0 \pm 0.4^*$
[63]	A	X	5-25	$0.05\text{-}12^*$	$0.2\text{-}50$
[64]	A	X	3.8-6.3	$0.465 \pm 0.025^*$	1.9 ± 0.1
[64]	A	X	6-14	$0.22 \pm 0.07^*$	0.9 ± 0.3
[64]	A	M	3.8-6.3	$4.4 \pm 0.7^*$	18 ± 3
[64]	A	M	6-14	$3.9 \pm 0.7^*$	16 ± 3
[64]	A	U	3.8-6.3	$1.2 \pm 0.1^*$	4.7 ± 0.4
[64]	A	U	6-14	$0.9 \pm 0.2^*$	3.7 ± 0.8
[65]	A	U	8.8-16	$1.7 - 2.1^*$	$7.1 - 8.5$
[65]	A	X	8.4-17.3	$0.47 - 0.61^*$	$1.9 - 2.5$
[54]	T	U	27.6-34.5	$2.8 - 9.3$	$11\text{-}38^*$
[10]	T	X	25-57	5.4^*	22
[10]	T	XR	38-64	5.1^*	21
[66]	T	R	24-68	$6.4 \pm 0.5^*$	26 ± 2
[66]	T	XR	24-68	$7.8 \pm 0.5^*$	32 ± 2
[66]	T	CR	24-68	$15 \pm 2^*$	62 ± 9
[66]	T	MR	24-68	$8.3 \pm 0.7^*$	34 ± 3

Table 1.2: Previous experimental results. The table lists microtubule flexural rigidities κ and persistence lengths l_p obtained for given length ranges by either analysis of thermal shape fluctuations (T) or active deformation (A). An asterisk marks numbers that were calculated from the neighbouring column using the relation $\kappa = l_p k_B T$. Condition codings are unstabilized (U), taxol-stabilized (X), stabilized with the nucleotide analogue GMPCPP (C), stabilized with microtubule-associated proteins (M), and rhodamine-labeled (R).

tions. But here, too, different studies have come to very different conclusions. For instance, while Mickey et al. [66] present evidence that stabilization with the chemotherapy drug taxol increases microtubule stiffness, several other groups obtain the opposite result [67, 68, 65].

While these factors may certainly be a source of scatter between values obtained by different groups, they are not sufficient to explain the observed scatter seen even between results within each individual study. There is, however, an alternative explanation that has recently attracted more attention and credibility. Several studies using both active and passive techniques have presented evidence that the measured stiffness may be a function of length [69, 70, 59, 63, 71], and new models of microtubule mechanics have been proposed that explain the observed length dependence as a consequence of mechanical anisotropy in microtubule architecture [70, 59, 5, 6]. Contacts between dimers along one protofilament have large contact areas dominated

by strong electrostatic and hydrophobic interactions, while interactions between adjacent protofilaments are relatively weak [36]. Those weak interactions are hypothesized to facilitate interprotofilament shear, thereby causing shorter microtubules to be able to support larger deformations than would otherwise be expected. The proposed length dependence is largely consistent with the results listed in Table 1.2.

Chapter 2

Experimental procedures

2.1 Thermal fluctuation measurements on grafted microtubules

2.1.1 Assay

Fig. 2.1 shows a schematic of the assay employed for thermal fluctuation measurements on grafted microtubules. Microtubules are covalently attached with one end to a gold substrate such that position and tangent orientation at that end are fixed. The advantages of the grafted boundary conditions

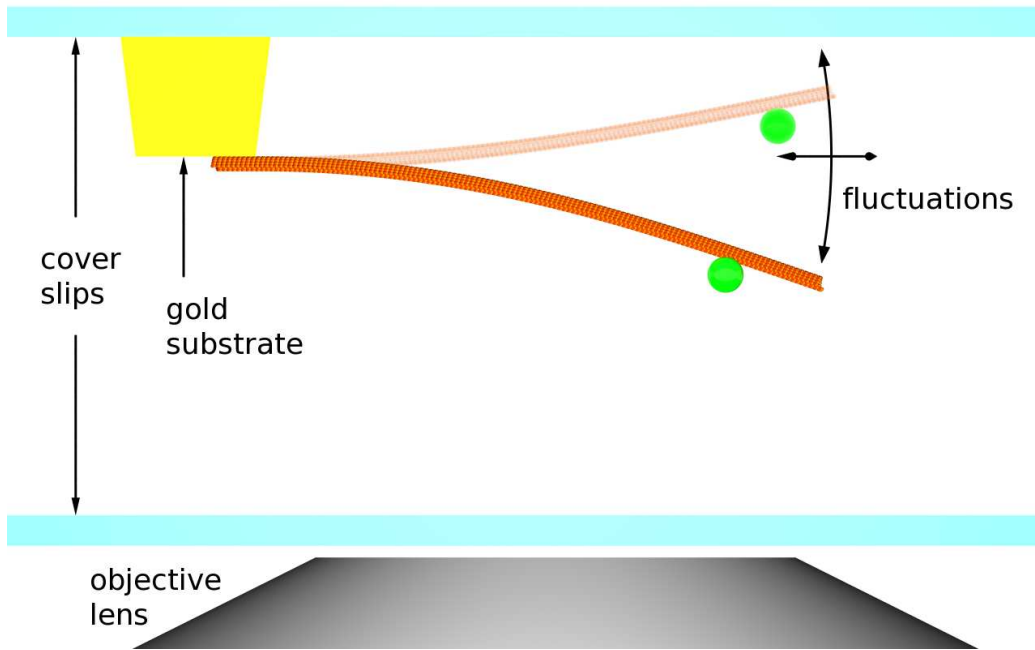


Figure 2.1: Schematic of the assay for measurements on grafted microtubules [60]. Inside a sample chamber, one end of the microtubule is covalently attached to a gold substrate, while the other end is free to fluctuate in 3D. Using epifluorescence microscopy, the sample is imaged from below and a 2D projection of the fluctuations is observed. The attached fluorescent bead serves as a tracer of the fluctuations.

are that there is a fixed reference frame for the assignment of coordinates and that the filament is prevented from diffusing away. Covalent binding of microtubules to the substrate is achieved using a standard protocol based on thiol chemistry [72, 73, 59].

The free end of the microtubule fluctuates in 3D, and a fluorescent bead attached somewhere along the length of the microtubule serves as a tracer of these fluctuations. Attachment of the bead is achieved using specific binding between the vitamin biotin, chemically bound to the tubulin, and the protein neutravidine, coating the fluorescent beads. Biotin-avidin binding represents the strongest known non-covalent specific bond. The use of the tracer bead as opposed to direct shape analysis of the fluctuating filament provides a two-fold advantage: Not only is the bright bead easier to track because of its higher fluorescence labelling density, but it is also less prone to photobleaching. While the phenomenon of phototoxicity in fluorescence imaging is not completely understood, it is thought to result from damage caused by free radicals in the solution that are generated by the fluorescence excitation itself. As fluorophores are being excited, there is a possibility of excited electrons getting stuck in a triplet state from where they cannot decay easily, leaving them to be collected by oxygen in the solution which thereby becomes a reactive oxygen radical that may in turn damage the fluorophores or the biological material they are attached to [74]. The fluorophores inside a bead are shielded from reactive agents in the solution and bleach only very slowly, while fluorescently labelled microtubules in particular have been reported to easily break up in fluorescence illumination [75, 76]. Even with the use of oxygen scavengers, the photon budget for microtubule shape fluctuation measurements via fluorescence microscopy is very limited, hence the localization precision is typically about an order of magnitude lower than for the single particle tracking of fluorescent beads.

The use of the substrate provides a spacer of $\sim 15\ \mu\text{m}$, ensuring that hydrodynamic interactions between the microtubule and the surface are minimal. Using epifluorescence microscopy, a 2D projection of the fluctuations can be observed from below. The microtubule and the bead are labelled with rhodamine and yellow-green fluorophores, respectively.

2.1.2 Microtubule polymerization

Taxol microtubules

Lyophilized bovine and porcine brain tubulin was purchased from a commercial vendor (Cytoskeleton Inc, Colorado, USA). See Appendix A for a detailed list of suppliers and product codes for the reagents used. Unlabelled and bi-

otinilated tubulin were suspended in ice cold 1mM GTP/BRB80 (80mM PIPES, 1mM EGTA, 1mM MgCl_2 , pH 6.8) supplemented with additional MgCl_2 to 5 mM. Experiment-sized aliquots of 10 μl and 2 μl at 10 mg/ml and 5 mg/ml, respectively, were flash-frozen in liquid nitrogen before being stored at -80°C .

For each experiment, one aliquot of both the unlabelled and the biotinilated tubulin were thawed quickly and kept on ice. One 20 μg vial of lyophilized rhodamine tubulin was suspended in a few μl of ice-cold 4mM MgCl_2 , 1mM GTP/BRB80 and then mixed with the contents of the other two aliquots. The volume of the sample was increased to $\sim 30 \mu\text{l}$ by adding more buffer.

As fluorescently labelled tubulin is prone to aggregation, a 5 min clear spin at 90,000 rpm and 2°C was performed using a TLA-100 rotor in a temperature-controlled ultracentrifuge (Beckman TL100, Beckman Coulter, Brea, CA, USA) to free the solution of denatured protein. Following the spin, the pellet of denatured tubulin was discarded and the supernatant incubated for 20-45 min at 37°C for polymerization.

In steady state, a solution of polymerizing microtubules still contains a significant fraction of free tubulin. These free dimers can both act as a fluorescent background and compete with microtubules for binding sites on the substrate. To separate the microtubules from the solution of free dimers, the sample was centrifuged at 35°C and 30,000-70,000 rpm for 5 – 10 min. The microtubule pellet was then twice washed gently with 50 μl of 20 μM taxol/BRB80 before being resuspended in the same solution and volume by gentle pipetting. The pipet tips used for transferring and mixing microtubule solutions were always cut to avoid breaking the filaments with shear forces.

Taxol microtubules were stored at room temperature in a dark container, and used within 5 days. For all experiments, microtubules were freshly diluted into 20 μM taxol/BRB80. Taxol solution was also prepared freshly from aliquots each day as taxol is poorly soluble in water and tends to crystallize. Taxol crystals bind tubulin aggressively and can even be confused with microtubule bundles [77]. Aliquots were prepared at 10 mM in anhydrous dimethylsulfoxide (DMSO) and stored at -80°C . Before being diluted 500 \times into BRB80, both the aliquot and the buffer were warmed to 37°C before mixing, and after vigorous pipetting the solution was cleared of taxol precipitates by centrifugation in a tabletop centrifuge and used within hours.

GMPCPP microtubules

The nucleotide analogue guanosine-5'-[(α , β)-methyleno]triphosphate (GMPCPP) has an affinity for tubulin that is lower than that of GTP (~ 4 -8 times [78],

~ 10 times [79]). As the tubulin that is available commercially is supplied with an excess of GTP, it is necessary to free the tubulin solution of GTP in order to be able to incorporate a significant amount of GMPCPP.

To this end, a lot of $\sim 300 \mu\text{g}$ of tubulin with a labelling ratio as before was subjected to a buffer exchange into a GMPCPP buffer using a protein desalting spin column (89849, Thermo Scientific, Rockford, IL, USA). In order to rid the sample of the last traces of GTP that may still be bound to the tubulin, the sample was incubated at 37°C for polymerization. In this step, any GTP that is incorporated into a microtubule is expected to be hydrolyzed to GDP which - although it has an affinity for tubulin only 2-6 times lower than that of GTP [32, 80] and hence similar to that of GMPCPP - is less likely to be incorporated into microtubules later. The polymerized microtubules are then pelleted and depolymerized by the addition of CaCl_2 to 2 mM. Because of the presence of 1 mM EGTA in the solution, the effective calcium concentration is then 1 mM. After ~ 20 min on ice, the CaCl_2 is neutralized by the addition of further EGTA to 3 mM, and the solution is pipetted vigorously to break up any remaining microtubules. After a clear spin as in Section 2.1.2, the tubulin solution is aliquoted in units of $5 \mu\text{l}$. Several such lots were prepared, and stored at -80°C .

Because GMPCPP is a potent microtubule nucleator [78], polymerization must occur at low concentrations in order to yield microtubules long enough for experiments. Since at low concentration the growth speed is very low, the solution must be left to polymerize for a long time, e.g. overnight. As tubulin is very labile and prone to aggregate when left at warm temperature for a long time, the polymerization temperature was decreased to 30°C instead of 37°C , and the solution was replenished with fresh GMPCPP and tubulin several times.

Typically, one GMPCPP aliquot would be diluted into $30 \mu\text{l}$ of 4 mM MgCl_2 , 1 mM GMPCPP/BRB80 and incubated at 30°C . After ~ 3 h, another 2 aliquots diluted into $60 \mu\text{l}$ 4 mM MgCl_2 , 0.5 mM GMPCPP/BRB80 would be added to the sample and left to polymerize overnight. Since GMPCPP microtubules were found to be very sensitive to breakage during pelleting and resuspension, they were pelleted by centrifugation in a table top centrifuge (Beckman 6415C, Beckman Coulter, Brea, CA, USA) at 14,000 rpm for ~ 40 min, and then gently resuspended in $40 \mu\text{l}$ BRB80.

Mixed nucleotide content

In order to produce microtubules with a mixed nucleotide content, unlabelled, rhodamine-labelled and biotinilated tubulin were mixed exactly as for taxol polymerization, except that instead of 1 mM GTP, 1 mM GMPCPP was

added. Because the aliquots of tubulin already contained some GTP, a concentration of ~ 0.4 mM GTP remains. This value is an estimate based only on the nucleotide added during aliquoting, and neglects any GTP already present in the lyophilized product.

After a cold spin performed as before, 4 mM MgCl_2 /BRB80 was added to a total volume of 80 μl . The resulting solution of 1.6 mg/ml tubulin, 0.375 mM GMPCPP, 0.15 mM GTP, 4 mM MgCl_2 /BRB80 was flash frozen in 5 μl units in liquid nitrogen and stored at -80°C .

For each experiment, 2 aliquots of the tubulin mix would be augmented with GMPCPP and 4 mM MgCl_2 /BRB80 to a volume of ~ 20 μl at a concentration of 0.8 mg/ml tubulin, 1 mM GMPCPP, 0.075 mM GTP.

The solution was then incubated at 33°C for 3 h. The time, temperature, and concentration range was found to suitably balance the constraints of lower stability compared to pure GMPCPP microtubules and higher nucleation rate compared to GTP microtubules. The microtubules were then gently pelleted at 35°C , 20,000 rpm, for 5 min, and resuspended in 40 μl warm BRB80. The resulting nucleotide composition is doubtful as some of the GTP is likely to have been turned over during polymerization, and the nucleotide affinities for tubulin as well as their affinity for the microtubule lattice are not known precisely. Given the limited stability of the resulting microtubules, it is however likely that their nucleotide content was dominated by GDP.

2.1.3 Sample preparation

Glass cleaning

All coverslips used for experiments were cleaned by repeated sonication in a 2% solution of the detergent Hellmanex (Hellma GmbH & Co. KG, Müllheim, Germany). Coverslips were placed vertically in a custom-made stainless steel holder sitting in glass container. The container was filled with detergent solution and sonicated for 15 min. After flushing the glass container with purified water for 5 min, the coverslips were sonicated in water for another 15 min and then flushed again. This procedure was repeated three times. Afterwards, the coverslips were dried with a flow of purified nitrogen gas.

Flow chamber

Parallel bar gold grids for electron microscopy are available commercially (G1016A, Ted Pella Inc., Redding, CA). These grids have an outer diameter of 3.05 mm, are 14-18 μm thick, and feature parallel bars with a pitch of 60 μm and a width of 12 μm . The grids were glued onto round 15 mm coverslips (Menzel Gläser, Germany) using a chemically inert, solvent-free silicone glue

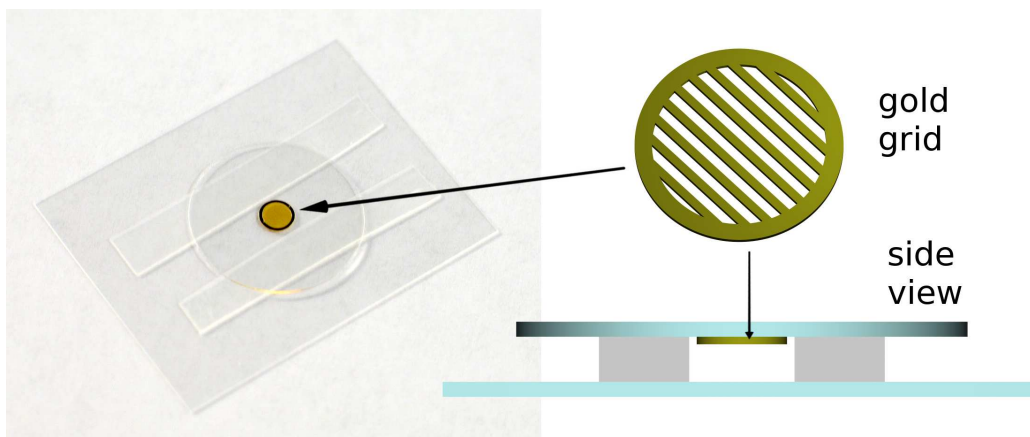


Figure 2.2: The sample chamber for measurements on grafted microtubules [60]. An electron microscopy gold grid with microscopic parallel bars is glued onto a round coverslip. Parafilm spacers between it and a rectangular coverslip create a simple flow chamber with a volume of 10-20 μl .

(Elastosil N10, Wacker Chemie, Germany) and left to dry for at least a day. Prior to use, the grids were cleaned by immersing them in a solution of 5% ammonia and 5% hydrogen peroxide in water for 15 min and successively rinsing them with copious amounts of water and ethanol. Before each day of experiments, three freshly cleaned grids were immersed overnight in a freshly prepared 5 mM solution of 11-mercaptoundecanoic acid (11-MUA) in ethanol to facilitate formation of a monolayer on the gold surface. These procedures were performed in custom-built teflon wells with a volume of 1 ml.

The next day, the gold grids were rinsed with copious amounts of ethanol, dried with pure nitrogen gas, and quickly assembled into a flow chamber. The flow chambers consisted of a 24×32 mm coverslip (Menzel Gläser, Germany) with spacers made of either double-sided adhesive tape or parafilm that the round coverslip is inverted onto, with the grid facing down and its bars oriented perpendicular to the direction of flow in the chamber (see Fig. 2.2).

Initial experiments using adhesive tape found that some brands produced highly variable results, presumably due to solvents leaching into the chamber and reacting with the microtubules. Parafilm has the advantage that it is relatively inert chemically, but requires the chamber to be heated and compressed briefly in order to seal.

The resulting volume of the sample chamber was on the order of 10 μl , and solutions could easily be exchanged by blotting with lab tissue. In order to avoid bubble formation, parafilm chambers were briefly flushed with ethanol before flushing with BRB80. The monolayer on the gold surface was then activated by flushing in a freshly prepared solution of 100 mM

N-hydroxysuccinimide (NHS) and 100 mM N-(3-Dimethylaminopropyl)-N-ethylcarbodiimide hydrochloride (EDC) in BRB80. In order to prevent the samples from drying, they were stored inside a petri dish containing some lab tissues soaked in water between preparation steps.

After 20-30 min of activation, the chamber was thoroughly flushed with 500 μ l of BRB80 and, in the case of taxol microtubules, 100 μ l of taxol/BRB80 before 20-40 μ l of a 10-100 \times diluted microtubule solution were flushed in. For taxol microtubules, all dilutions of the microtubule solutions and subsequent flushes of the sample chamber were performed with taxol/BRB80. For other microtubules, plain BRB80 was used. The microtubule solution was then incubated for 30-60 min in order to allow time for the formation of covalent bonds between microtubules and the gold substrate. In the meantime, a 20 \times diluted solution of 200 nm neutravidine-coated, yellow-green fluorescent beads (F-8774, Molecular Probes, Invitrogen, Carlsbad, CA) in BRB80 was sonicated for 20 min to be flushed in after microtubule incubation. The beads were then diluted another 20 \times into BRB80 or taxol/BRB80, and 40 μ l of the solution were flushed into the sample chamber to be incubated with the microtubules for 30-60 min in order to facilitate bond formation between the biotin on the microtubules and the neutravidine on the beads. After the incubation, the flow chamber was flushed with 200 μ l of buffer to remove all unbound microtubules and beads.

In order to limit photobleaching [75, 76], an oxygen scavenging system was employed. Solutions of \sim 10 mg/ml glucose oxidase/BRB80 and \sim 10 mg/ml catalase/BRB80 as well as saturated hemoglobin solution were prepared daily, and stored on ice. A saturated solution of hemoglobin was prepared by adding 100 μ l of BRB80 to a 1.5 ml reaction tube filled to about 1/3 with hemoglobin, and spinning the mixture for 10 min at 10,000 rpm in a tabletop centrifuge (Eppendorf 6415C). For each sample, a fresh mixture of equal parts of the glucose oxidase solution, catalase solution, and 1 M dextrose was supplemented with 1/10 of the volume from the top of the centrifuged hemoglobin solution. The resulting mixture was added at 10% to the final solution being flushed into the sample chamber before sealing with valap.

Valap is a waxy mixture of vaseline, lanolin, and paraffin, which is commonly used in the biological science community because of its chemical inertness. Liquid when hot, it can be applied with a brush and will almost instantaneously solidify in place. Early experiments used vacuum grease instead which is similarly chemically inert, but has the disadvantage of remaining soft and not providing as good a seal. Samples sealed with valap were often found to be still intact after days.

The sample was then mounted with vacuum grease on a custom-built sample holder designed to match the custom-built stage of the epifluorescence

microscope.

2.1.4 Instrumentation

All experiments were performed on a modified Zeiss Axiovert 10 inverted epifluorescence microscope (Zeiss, Jena, Germany) with a custom-built stage optimized for high mechanical stability. For fluorescence illumination, an X-Cite 120 light source (EXFO life sciences, now Lumen Dynamics, Ontario, Canada) was used in conjunction with fluorescence filters for optimized for yellow-green fluorescence/GFP (HQ470/40x, 495DCXT, HQ525/50m+750LP) and rhodamine (HQ535/50x, Q565LP, HQ615/60m+1064; Chroma, Vermont, USA). While the rhodamine filter set allowed for some residual yellow-green fluorescence to be observed, the yellow-green/GFP filter set prevented excitation of the rhodamine dye. As a result, microtubules could be imaged at the same time as attached yellow-green beads, but long term observations on the beads could be performed without photodamage to the microtubules.

A Sensicam QE high sensitivity CCD camera (PCO AG, Kelheim, Germany) was attached to the custom-built bottom port of the microscope rather than the manufacturer-supplied top port. This arrangement minimized the number of optical components in the light path as well as the potential for mechanical instability.

In order to avoid distortions imaging tens of μm deep into the sample, a high numerical aperture (NA=1.2) water lens (Olympus UPlanSApo60xW) was used. Because the tube lens in the Zeiss microscope has a focal length of 164.5 mm rather than the 180 mm corresponding to the Olympus standard, the effective magnification of the objective lens in this setup is not $60\times$, but $164.5/3 \approx 55\times$. In addition, the difference in colour correction strategies between Zeiss and Olympus leads to slight lateral and longitudinal colour aberrations. The effect is however small and not critical to this application.

The camera pixel size of $6.45 \mu\text{m}$ yields a calibration of $\approx 118 \text{ nm/pixel}$.

2.1.5 Recordings

Using the rhodamine filter set, both microtubules and beads were visible. This allowed for inspection of the geometry, and the selection of suitable microtubules. Single microtubules with a bead attached somewhere along their contour were chosen. Fig. 2.3 shows an example.

Typically, 100-300 frames at exposures of 100-200 ms of the arrangement were recorded using the rhodamine filter set. These data allow for measurements of microtubule length and the position of the bead along the contour.

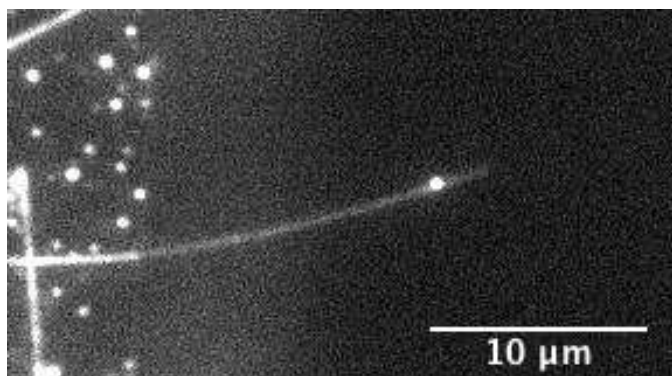


Figure 2.3: Example of a microtubule attached to a bar of the gold grid (left) and with one 200 nm bead attached close to its tip, imaged using the rhodamine filter set. Other microtubules and beads are seen stuck to the surface of the bar.

Then, using the GFP filter set, 10,000 – 40,000 frames of only the bead were recorded at typical exposure times ranging from 14 to 80 ms. By reducing the read-out region to the immediate vicinity of the bead, often as small as 32×32 pixels, frame rates up to ~ 70 Hz could be achieved, depending on the location on the chip. Exposure times and frame rates were adjusted depending on the length of the microtubule under consideration. Speed was a priority for measurements of very short microtubules which fluctuate on short timescales, while for longer microtubules exposure times were increased to compensate for loss of resolution due to the bead transiently moving out of focus due to the microtubule's fluctuations in the vertical direction.

An optimally prepared sample generally yielded an average of about 4 microtubules with a suitable geometry.

2.2 Thermal fluctuation measurements on free microtubules

In order to be able to check the consistency of the results for different boundary conditions as well as for comparison with previous results from the literature, an assay based on shape fluctuations of free, rather than grafted, microtubules was implemented as well.

2.2.1 Microtubule polymerization

Taxol microtubules were prepared as described in Section 2.1.2. Because of changes in the commercial availability of bovine tubulin, all experiments on free microtubule shape fluctuations were performed with porcine brain tubulin. Although biotinylation was not required for these experiments, it was retained in order to provide exactly the same conditions as for the grafted microtubules.

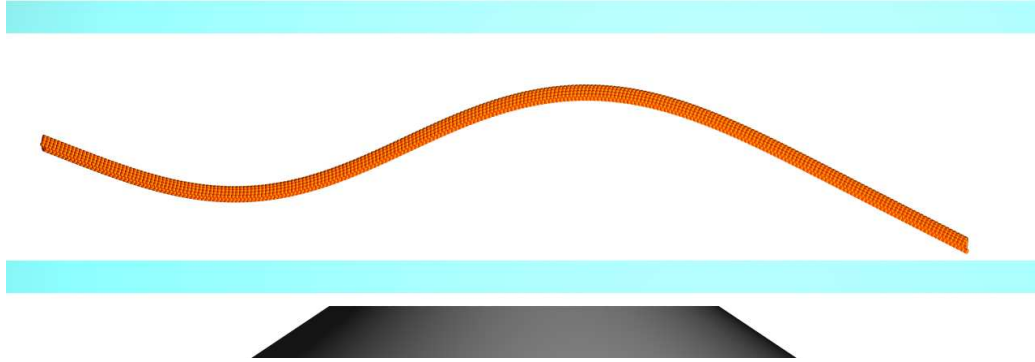


Figure 2.4: Schematic of the assay for measurements on free microtubules. The shape fluctuations of the microtubule are constrained to the image plane by the only $\sim 1\ \mu\text{m}$ thick sample chamber.

2.2.2 Sample preparation

In order to be able to image the shape fluctuations of a free microtubule in solution with a wide-field microscope, the fluctuations have to be constrained to the image plane. To this end, the sample chambers, built from a $24 \times 32\ \text{mm}$ and a $18 \times 18\ \text{mm}$ coverslip, had to be limited to a thickness of $\sim 1\ \mu\text{m}$. In order to avoid interactions between the microtubules and the glass coverslips, the glass surfaces had to be passivated. Common methods of shielding surfaces against unspecific interactions include coating with the blocking proteins bovine serum albumin (BSA) or casein, or functionalizing the surface with chemical groups such as polyethylene glycol (PEG). Both avenues were pursued for the experiments described here.

Coating with blocking proteins

If a solution of BSA and casein is brought into contact with a glass surface, the proteins readily adsorb to it. Unfortunately, proteins become labile when exposed to air so that once a surface is coated, it has to be kept wet. This presents a challenge when trying to construct very thin sample chambers.

Two approaches were undertaken: One can coat the glass surfaces first by applying BSA or casein solution to the clean coverslips, rinsing them with buffer solution after 10 min of incubation, placing a drop of microtubule solution on one coverslip, putting the other one on top, and then squeezing out as much solution as possible to produce a thin sample chamber. Unfortunately, this approach only produced chambers that were still several μm thick but broke all the microtubules into small fragments, presumably due to the shear forces generated when squeezing.

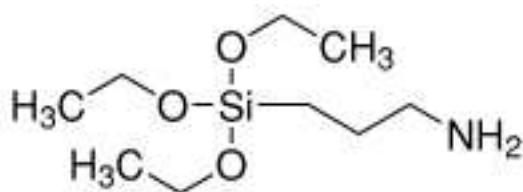


Figure 2.5: 3-Aminopropyltriethoxysilane (APTES).

Alternatively, one can start out with dry clean glass surfaces and limit the thickness of the sample chamber by limiting the volume of solution confined between the two coverslips. In this case, both the microtubules and the blocking proteins have to be in the solution at the same time, and the blocking proteins have to be more efficient in coating the surface than the microtubules. This approach was successful with 2-5 mg/ml casein, but not with BSA solutions. Interestingly, the shielding did not work best when the initial coverslips were cleaned as thoroughly with Hellmanex detergent as described in Section 2.1.3. In this case, the interaction between the microtubules and the clean glass surface was so strong that they would stick to the surface immediately before the casein was able to coat it. Optimal results were achieved by rinsing uncleaned coverslips briefly with ethanol and then blow-drying them with nitrogen immediately before $\sim 0.7 \mu\text{l}$ of solution were placed between them. The sample was then sealed with either valap or mineral oil.

Coating with PEG

Polyethylene glycol (PEG) is a hydrophilic chain molecule that blocks non-specific adhesion. In order to covalently attach the chain to a glass surface, the surface is first functionalized with a layer of an aminosilane. The amino groups of this layer are then coupled to a PEG succinimidyl ester.

First, the glass was thoroughly cleaned by two steps of Hellmanex cleaning as described in Section 2.1.3. After thorough rinsing with purified H_2O , the coverslips were sonicated in HPLC grade acetone before being blow-dried with nitrogen. Immediately after this cleaning step, the coverslips were submerged in a 2% solution of APTES (see Fig. 2.5) in acetone for 4 min. They were then rinsed once with acetone and flushed with purified H_2O for 5 min before being baked in a vacuum oven at $\sim 120^\circ\text{C}$ until dry. Dried coverslips were stored in a nitrogen atmosphere until PEGylation.

For PEGylation, a 10 mM solution of mPEG-SVA (see Fig. 2.6) in 100 mM sodium bicarbonate (pH ~ 8.3) was prepared under a nitrogen atmosphere.

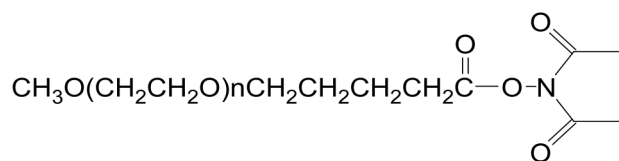


Figure 2.6: Methoxy poly(ethylene glycol) succinimidyl valerate (mPEG-SVA). A compound with a molecular weight of 5,000 Da was used, corresponding to a large polymer brush of $n \approx 100$ PEG units.

A few tens of μl solution were sandwiched between two APTES-functionalized coverslips and incubated in a darkened pipet tip box overnight. The bottom of the box was filled with water to avoid evaporation of the solution. The next morning, the coverslips were briefly rinsed with purified H_2O , blow-dried with nitrogen, and immediately assembled into a sample chamber. Microtubule stock solution was diluted 50-500 times in $20 \mu\text{M}$ taxol/BRB80 and augmented oxygen scavenger as for the experiments on grafted microtubules (see Section 2.1.3). Typically, about $0.4 \mu\text{l}$ of microtubule solution were placed between the coverslips, and then the sample was sealed with either valap or mineral oil.

The PEG coatings provided a more reproducible shielding effect than the casein coating, and, due to their higher hydrophilicity and therefore better wetting properties, were also capable of producing thinner samples. Hence only few data points were collected using casein shielding, and the largest part of the measurements used PEG shielding.

2.2.3 Microscopy

The same sample holder was used as for the experiments on grafted microtubules. The thin samples often needed hours to equilibrate all mechanical stresses. Data was recorded only after drift in the same chamber had visibly come to rest. Focussing on occasional pieces of denatured proteins stuck to the top and bottom coverslips, the thickness of the sample chamber could be tested. Values of $1\text{-}2 \mu\text{m}$ were typically found.

In order to be able to observe the microtubules over long time spans without bleaching, a camera-triggered high speed shutter (UniBlitz VS25, Vincent Associates, Rochester, NY, U.S.A.) was employed to limit fluorescence excitation to exposures. The shutter lag time was measured to be about 6 ms (see Fig. 2.8), comparable to the 5 ms expected from camera and shutter manufacturer information (see Fig. 2.7).

Exposure times, corrected for this lag effect, ranged from 14 ms to 200 ms. Typically, frame rates between 0.1 and 1 Hz were used in order to limit cor-

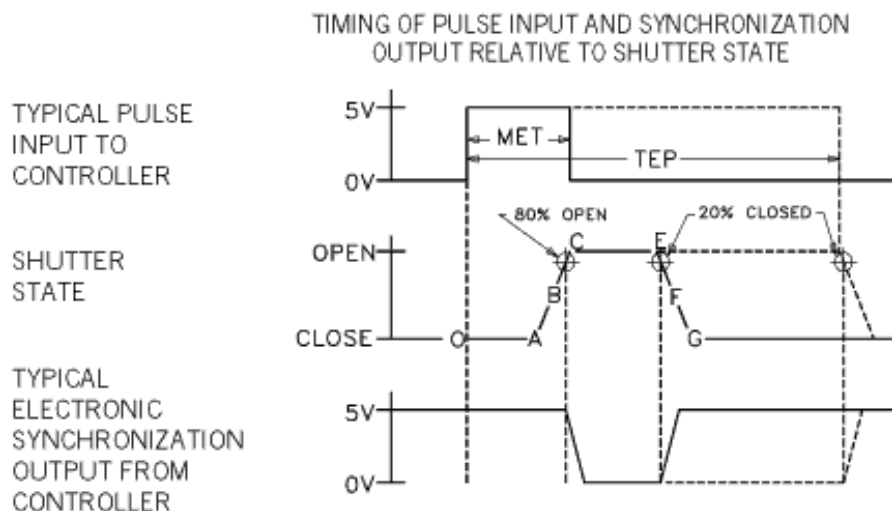


Figure 2.7: Shutter lag time diagram [81]. According to manufacturer's information, the total opening lag time (0-C) is 6 ms. Because the camera controller signal rises 1 ms before the exposure, an effective lag time of about 5 ms is expected.

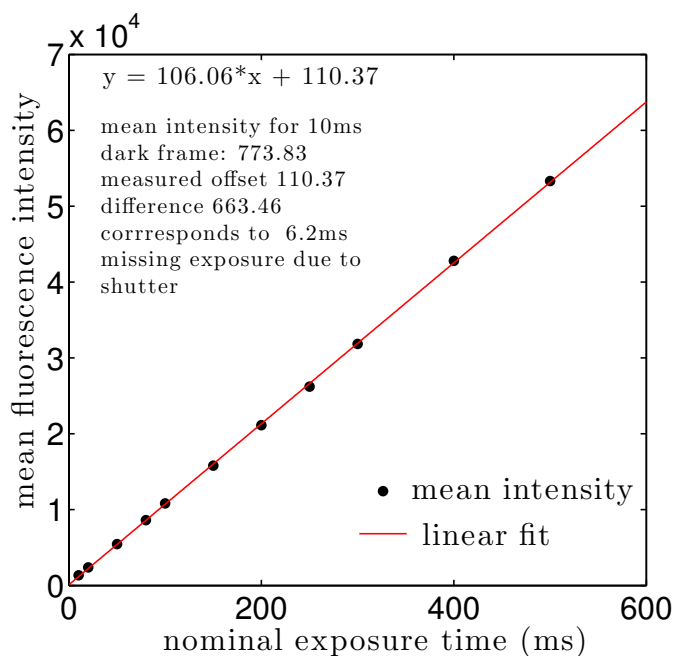


Figure 2.8: Shutter lag time measurements. Images of a fluorescent samples were taken at various exposure times. The camera offset was determined by taking a short exposure in the dark. This offset is subtracted from the measured offset of the linear relation between intensity and exposure time to extract the time span of the exposure that was dark due to the lag in shutter reaction.

relations between consecutive frames. For some microtubules, an additional high speed movie was recorded at frame rates in the range between 10 and 30 Hz in order to obtain an estimate of the dynamics. Up to 1500 frames could be gathered before the microtubule had bleached too much.

The microtubules generally showed some visible intrinsic curvature, but only few had sufficient intrinsic curvature to prevent them from rotating in the sample chamber.

Chapter 3

Data analysis

3.1 Error sources in time series measurements

3.1.1 Low-pass filtering corrections

Any measurement that relies on a finite integration time is subject to low-pass filtering. Fluctuations that occur during the integration time are averaged over, resulting in a blurred time series that is open to misinterpretation. For random motion in a harmonic potential, the result of low-pass filtering is a measured position distribution which is narrower than the true distribution. The narrowing occurs because the average of any section of a position time trace will be biased towards the centre of the position distribution. The size of the effect depends on how large the integration time W is compared to the autocorrelation time τ of the motion. Fig. 3.1 illustrates the effect for the case of $W = \tau$.

In order to derive a mathematical description of the effect, we consider a

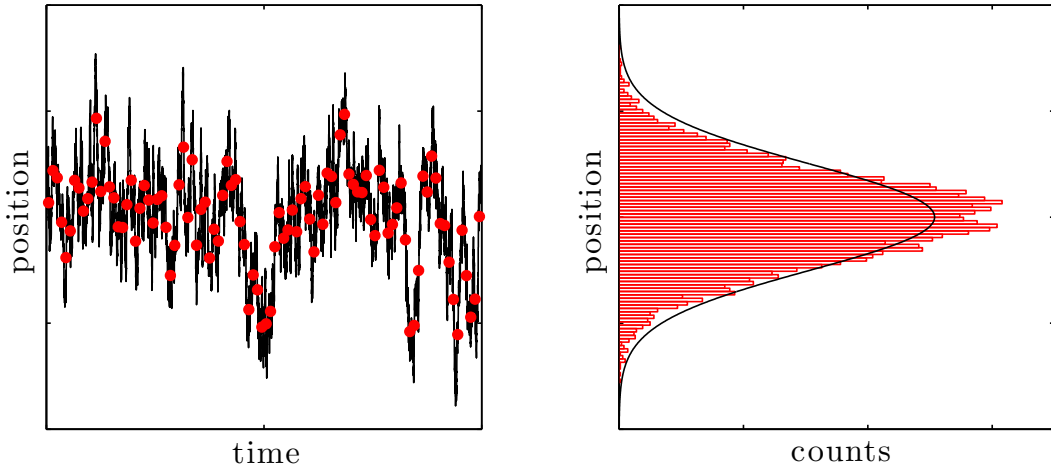


Figure 3.1: Low-pass filtering effects for a random walk in a harmonic potential. A random walk in a harmonic potential (black line) is measured with an integration time $W = \tau$ (red circles). As a result, a histogram of the measurements (red bars) is narrower than the true distribution (black line) by a factor of ~ 0.74 (see Eq. 3.8).

Brownian particle in a harmonic trap with force constant k and drag coefficient γ . Its autocorrelation time is given by $\tau = \gamma/k$, and its autocorrelation function is

$$A(t) = \langle x(t')x(t' + t) \rangle_{t'} - \langle x(t') \rangle_{t'}^2 = \frac{k_B T}{k} e^{-t/\tau}. \quad (3.1)$$

The power spectral density is given by the Fourier transform of the autocorrelation function:

$$P(\omega) = |\tilde{x}(\omega)|^2 = \frac{2\gamma k_B T}{\gamma^2 \omega^2 + k^2}. \quad (3.2)$$

If the particle's position is acquired with an integration time of W , then measured position x_m is related to the true position x via a convolution with the imaging function $h(t)$:

$$x_m(t) = \frac{1}{W} \int_{t-W}^t dt' x(t') = x(t) \star h(t), \quad (3.3)$$

where

$$h(t) = \begin{cases} 1/W & \text{if } 0 < t < W \\ 0 & \text{else} \end{cases}.$$

In Fourier space, the convolution becomes a product and the measured power spectral density becomes [82]

$$P_m(\omega) = |\tilde{x}_m(\omega)|^2 = |\tilde{x}(\omega)|^2 |\tilde{h}(\omega)|^2 = \frac{2\gamma k_B T}{\gamma^2 \omega^2 + k^2} \left(\frac{\sin(\omega W/2)}{\omega W/2} \right)^2. \quad (3.4)$$

Performing an inverse Fourier transform on the Eq. 3.4, we find the measured autocorrelation function [83]:

$$A_m(t) = \frac{1}{2\pi} \int_{-\infty}^{\infty} d\omega P_m(\omega) e^{-i\omega t} = \frac{1}{2\pi} \int_{-\infty}^{\infty} d\omega \frac{2\gamma k_B T}{\gamma^2 \omega^2 + k^2} \left(\frac{\sin(\omega W/2)}{\omega W/2} \right)^2 e^{-i\omega t} \quad (3.5)$$

$$= \begin{cases} \frac{k_B T}{k} e^{-t/\tau} \frac{\tau^2}{W^2} (e^{-W/\tau} (e^{2t/\tau} + 1) - 2 - 2 \frac{t-W}{\tau} e^{t/\tau}) & \text{if } 0 \leq t \leq W \\ \frac{k_B T}{k} e^{-t/\tau} \left(\frac{\sinh(\frac{W}{2\tau})}{\frac{W}{2\tau}} \right)^2 & \text{if } t > W \end{cases}. \quad (3.6)$$

From Eq. 3.3, the narrowing effect on the variance of the position distribution can be computed [82] to take the form

$$\sigma^2(x_m) = S(\alpha) \sigma^2(x), \quad (3.7)$$

where the factor S , plotted in Fig. 3.2, is given by the following, with $\alpha := W/\tau$:

$$S(\alpha) = \frac{2}{\alpha} - \frac{2}{\alpha^2} (1 - e^{-\alpha}) . \quad (3.8)$$

The measured mean square displacement (MSD) then follows [82]:

$$\text{MSD}_m(t) = 2\sigma^2(x_m) - 2A_m(t). \quad (3.9)$$

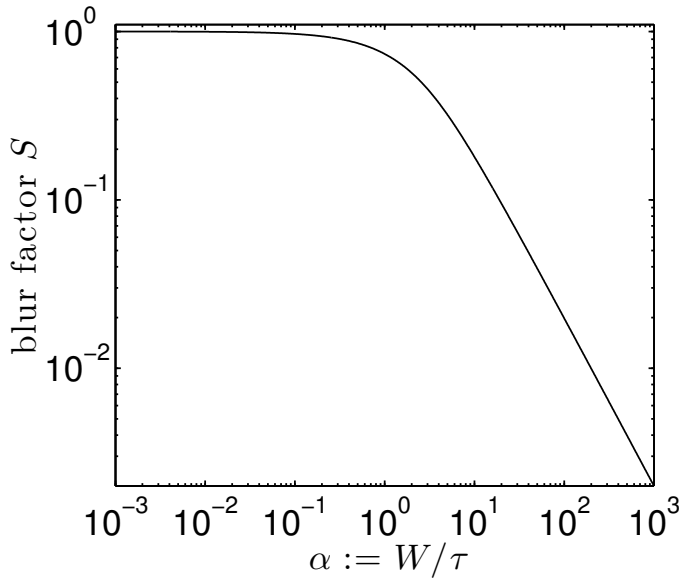


Figure 3.2: Blur factor S plotted against $\alpha := W/\tau$. For short exposure times W , $S \approx 1$ and the measured variance V_m is equal to the true variance V . For $W \gtrsim \tau$, S drops quickly, and $V_m < V$.

At first glance, the case distinction in Eq. (3.5) may seem superfluous as data points are taken for times larger than the integration time anyway. And indeed the correction formula for the measured autocorrelation for $t > W$ is only a multiplicative factor that is independent of time t and would therefore still allow for a correct determination of the relaxation time τ . This neglects however the data point $A(t = 0)$ which equals the position distribution variance and therefore has a different correction factor. As shown in Fig. 3.3, a fit of Eq. (3.1) to a blurred autocorrelation sequence will lead to an overestimation of the relaxation time. For the mean square displacements the effect is even more drastic. The measured curve is noticeably offset with respect to the true one, and the overestimation of the relaxation time is even more severe. The true relaxation time and position variance can however be recovered from a fit of the corrected expressions Eqs. 3.5 & 3.9.

It is important to note, however, that the sampling rate f has to be sufficiently high to at least partially resolve the dynamics in order for such a fit

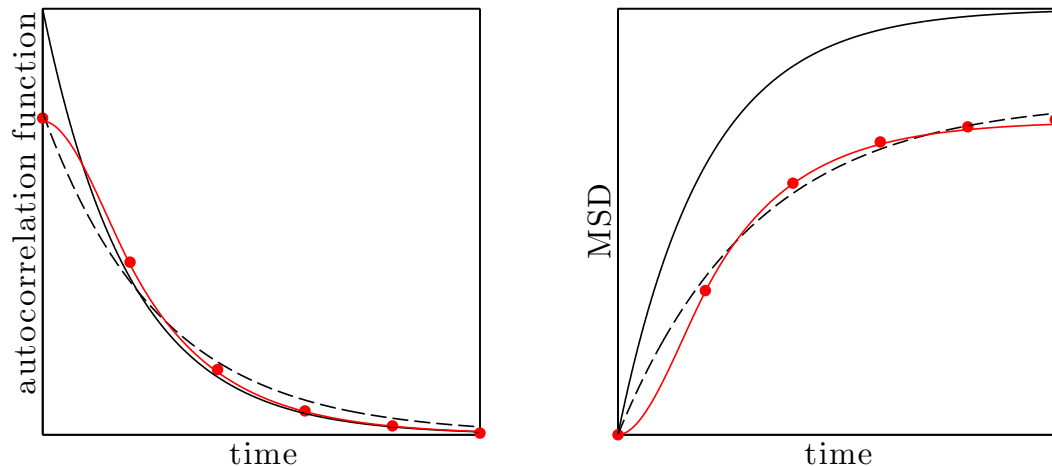


Figure 3.3: Low-pass filtering effects on dynamics measurements. The autocorrelation (left) and MSD (right), shown in red, are shown for the same case as in Fig. 3.1. The measured data (red circles) deviate significantly and by more than a multiplicative factor from the theoretical expectations (black lines). A fit of Eq. 3.1 (dashed black line) overestimates the relaxation time by $\sim 30\%$ and $\sim 50\%$, respectively, and underestimates the position variance by $\sim 25\%$ in both cases. The solid red line shows the corrected expressions Eqs. 3.5 & 3.9.

to be of use, meaning f cannot be much slower than $1/\tau$. Since the exposure time W can generally not be larger than $1/f$, this correction technique is only useful when $W \simeq \tau$. For $W \ll \tau$, the correction becomes unnecessary, and for $W \gg \tau$, the fit will fail. One technique that has been proposed for the latter case is to acquire data for more than one exposure time W , observe how the measured variance V_m changes as a function of W , and use a fit of Eq. 3.8 in order to extract V [82]. Surprisingly, these considerations have only sporadically surfaced in the literature despite their wide applicability to processes studied by video microscopy. Eq. 3.8 seems to first have been derived by Yasuda et al. [84] before being discussed in more detail by Wong & Halvorsen [82], and Savin & Doyle touch on the subject in their work on measurement errors [85, 86].

3.1.2 Correlated measurements

Many of the most useful statistical tools that are available to test the significance of a result pose the requirement that individual data points be independent of each other.

For instance, the Central Limit Theorem states that means m of sets of n independent samples drawn from any fixed distribution with a finite variance σ^2 will be normally distributed with a variance σ^2/n [87], if n is sufficiently

large. If the underlying distribution is itself normal, no restrictions apply on n . This result is most useful for establishing the standard error of the mean (SEM) $\sigma(m)$ for a set of n measurements as

$$\sigma^2(m) = \frac{s^2}{n}, \quad (3.10)$$

where s^2 is the sample variance here which is used as an estimate of the true variance σ^2 .

If, however, the n individual measurements are correlated, the necessary conditions for the Central Limit Theorem are violated, and the SEM will underestimate the actual error, leading to unwarranted confidence in the result of a measurement. As time series obtained from measurements of physical processes are often subject to correlations, such an underestimation constitutes one of the common pitfalls in the interpretation of measurement results, and often goes unnoticed because the data extracted from correlated measurements tend to look very smooth, giving no indication of the underlying error.

Fortunately, techniques exist to derive realistic error estimates in the face of correlations. A necessary condition for their success is that the overall length of the measurement is significantly larger than the longest correlation time of the process being investigated, that is $n/f > \tau$.

A particularly efficient method with origins in the computer simulations community has been described by Flyvbjerg [88]. The basic strategy of this technique, commonly referred to as the *bunching* or *blocking* technique, lies in reducing the number of data points by blocking or piecewise averaging of the data until all correlations have been averaged over and the remaining data points can be considered independent. The usual statistical methods applicable to independent data points can then be made use of. Specifically, an error on the mean of the data can be constructed analogously to the SEM.

The variance of the mean $\sigma^2(m)$ as well as the mean m itself are invariant under a blocking transform, and after the transform has been applied to the data sufficiently many times to remove correlation between consecutive data points, the formula for the SEM (Eq. 3.10) can be used. In order to determine how many blocking transforms are necessary, Eq. 3.10 is applied after each transform, and the results are accepted once the error estimate becomes constant within its error.

To determine error bounds for the variance of the mean, the same logic applies. By Cochran's theorem, the standard error of the sample variance s^2 of n independent measurements is given by

$$\sigma(s^2) = \sqrt{\frac{2}{n-1}} \sigma^2. \quad (3.11)$$

Analogously to $\sigma^2(m)$, $\sigma(s^2)$ will become stationary once the data have been sufficiently blocked.

Using this strategy, error bars can be determined for any quantity that can be represented as the mean of a correlated time series. This applies not only to the actual mean of the raw data, but also to quantities such as the variance and the autocorrelation function.

3.1.3 Measurement errors

Errors in the measurement of a variable are almost unavoidable. If they are normally distributed and independent, however, their influence can often be accounted if not corrected for. Suppose a parameter x , be that the position of a particle or the amplitude of a bending mode, is measured experimentally. It is subject to measurement errors x_e such that every measurement $x_m(t)$ is

$$x_m = x(t) + x_e(t). \quad (3.12)$$

As a result, the variance of x_m over time is

$$\sigma^2(x_m) = \sigma^2(x) + \sigma^2(x_e), \quad (3.13)$$

assuming that x_e and x are not correlated. The autocorrelation function of x_m is then the sum of the autocorrelation functions of the true value and the error:

$$A_m(t) = \langle x_m(t')x_m(t' + t) \rangle_{t'} - \langle x_m(t') \rangle_{t'}^2 = A(t) + A_e(t) \quad (3.14)$$

If there are no correlations in the error, the autocorrelation function is unaffected, except at $t = 0$ where Eq. 3.13 holds.

For the measured mean square displacement $\text{MSD}_m(t)$, the reverse holds: The only point not affected by the presence of errors is the first data point which is by definition 0. All other points are offset by $2\sigma^2(x_e)$ from their true values.

As a consequence, fitting the MSD or the autocorrelation function may not always yield the same result although they are mathematically equivalent. For the MSD, the first point can be ignored in any analysis since it contains no information, and for the remaining points an offset can be allowed to account for the presence of errors. In case of the autocorrelation function, however, the situation is less favourable. It is not advisable to discard the first data point since it does contain information, it is however difficult to fit it using the same expression as for other data points because it is affected by an offset. For this reason, fits to the MSD can be more reliable.

On the other hand, the autocorrelation has the advantage of immediately revealing the presence of long-lived correlations because it is expected to approach 0, while the MSD would need to be compared to the variance.

3.1.4 Drift

Drift is often unavoidable in long term measurements. In the measurements of position fluctuations of beads attached to grafted microtubules, for instance, slow movement of the sample on its holder can cause drift. Often, it can be corrected for by simply subtracting a linear fit to the data. Generally, however, it is advantageous to rely on data analysis techniques that are not too strongly affected by the presence of drift. The variance of a time series of a measured parameter x is expected to be strongly affected by drift, with the drift increasing the value. The MSD of x , however, is generally not strongly affected on short timescales if the drift is slow.

This follows because drift acts as a directed motion superimposed on the fluctuations of x . The MSD for directed movement is proportional to $(vt)^2$ where v is the drift velocity, while for diffusion the MSD is proportional to t :

$$\text{MSD}(t) = 2Dt \quad (3.15)$$

where D is the diffusion constant. While at long timescales, directed motion will always dominate the MSD, at short time scales, the MSD is dominated by diffusion. If the parameter x is for instance exhibiting diffusion in a harmonic potential, the MSD will initially grow linearly before saturating at $2\sigma^2(x)$. If the drift is slow enough, the added term $\propto t^2$ will not be significant on time scales relevant to the saturation of the MSD.

As a result, it can be advantageous to obtain the true variance of the process of interest from the MSD saturation level rather than computed the variance of the full time series. The value obtained in this way will be less affected by slow drift, and in addition, a fit of the MSD allows one to take into account any offsets due to measurement error, which, as discussed in Section 3.1.3, would add to the time series variance.

For these reasons, all the following analyses will make use of MSDs rather than time series variances whenever the dynamics are resolved.

3.2 Measurements on grafted filaments

3.2.1 Single particle tracking

Due to diffraction, no microscope can create an image that exactly matches the reality. Every point is blurred into a shape called the point-spread function (PSF). The theoretical PSF of an ideal optical system has the shape of an Airy function. According to the Rayleigh criterion, then, two point sources can be resolved from each other if they are separated by a distance

of

$$\delta r \approx 0.61\lambda/(\text{NA}) \quad (3.16)$$

where NA is the numerical aperture of the objective lens in use. Given that typical NAs for high powered objective lenses are about 1-1.4, this resolution limit translates to about half a wavelength, or 200-300 nm in the visual.

Single particle tracking relies on the fact that when it is known that only a single particle is present, a fit of the PSF can yield its centre position to a precision that is essentially only limited by the number of photons collected. Rather than matching a perfect Airy function, the shape of an experimental PSF is highly dependent on the specific optics and their imperfections, but it can generally be approximated very well by a Gaussian profile. Gaussian fits to extract position of small particles or even single molecules in fluorescence microscopy have been performed since the advent of video microscopy and routinely yield precisions in the nm range [89].

Ref. [71] shows that the MATLAB-based implementation used in this study provides a resolution of approximately 3 nm for a 200 nm fluorescent bead under typical experimental conditions.

3.2.2 Extraction of mechanical parameters

Position distributions

The particle tracking routine yields two-dimensional position time traces for the bead attached to the microtubule. Slight drift is corrected for by subtraction of a linear fit. Fig. 3.4 shows an example of the resulting position distributions. The transverse and longitudinal direction of the position fluctuations are determined by repeatedly fitting a line through the position distribution and rotating by the slope angle.

As expected, the transverse position has a Gaussian profile. According to Eq. 1.32, the width L_T of the full distribution is given by

$$L_T^2 = \frac{s^3}{3l_p}, \quad (3.17)$$

where s refers to the position of the bead measured along the microtubule contour. This equation is however only exactly valid if all modes are resolved, which is unlikely to be the case. More commonly, only the first mode is resolved, and the variance is given by the contribution of only that mode to Eq. 1.32.

The longitudinal position distribution is very asymmetric and described

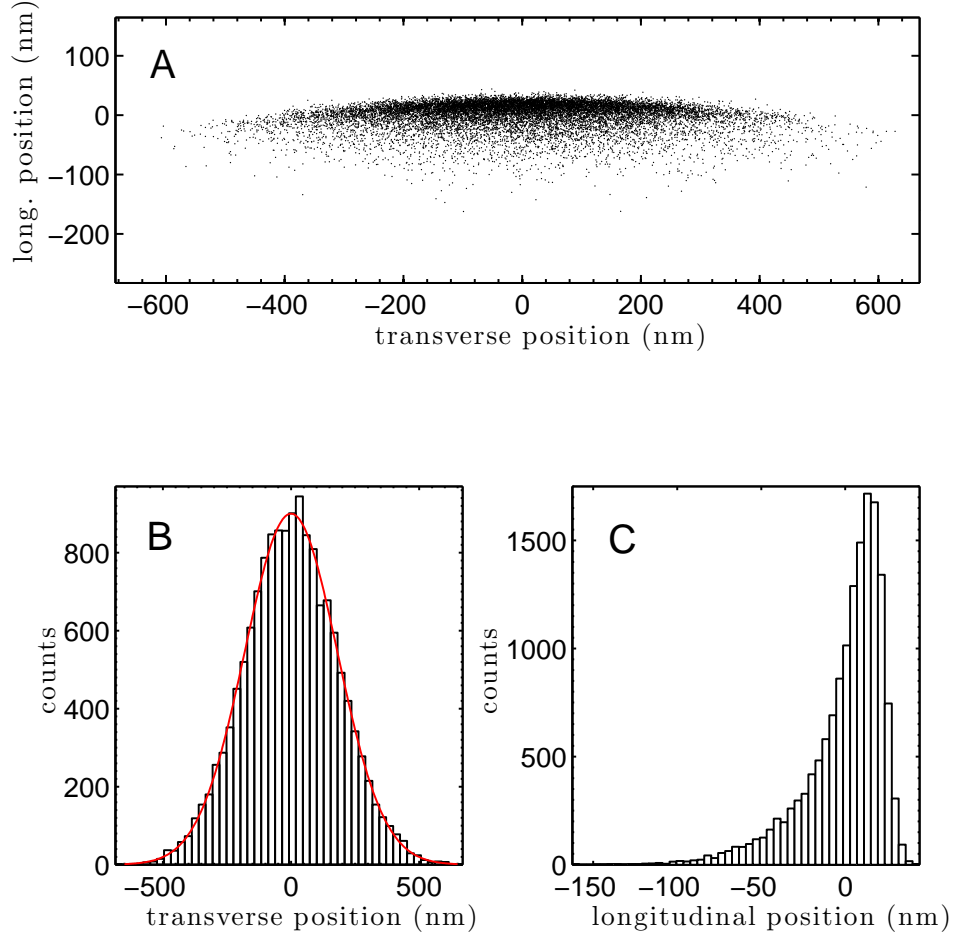


Figure 3.4: Example of an experimental position distribution for a bead attached to the tip of a microtubule of length $4.3 \pm 0.2 \mu\text{m}$ [60]. While the transverse position distribution has a Gaussian shape (red line), the longitudinal distribution is very asymmetric. The sharp decrease to the right reflects the inextensibility of the filament. The mean position is denoted as zero.

by a complicated infinite series expression with a characteristic length scale [58]

$$L_{\parallel} = \frac{L^2}{l_p}. \quad (3.18)$$

In principle, one could also use this longitudinal position distribution to extract mechanical information. In practice, however, the fluctuations in

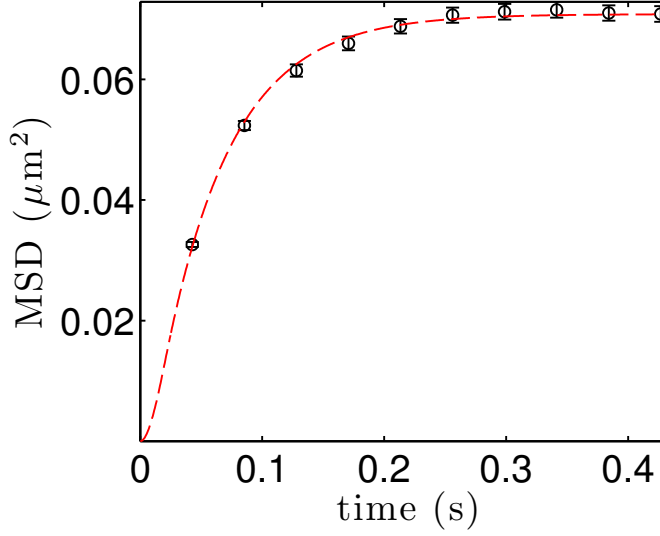


Figure 3.5: Example MSD for the microtubule in Fig. 3.4. A weighted fit of an offset version of Eq. 3.9 yields a relaxation time of 55 ± 3 ms and $V = 2.83 \pm 0.07 \text{ pix}^2 = 0.041 \pm 0.001 \mu\text{m}^2$. The offset corresponds to a position error of 3.5 nm.

this direction are so much smaller that errors would correspondingly become large. All further analysis presented here therefore exclusively makes use of the transverse positions.

Mean square displacements

MSDs are computed from the transverse position traces. Error bars for the individual data points are determined using the blocking procedure described in Section 3.1.2. Fig. 3.5 shows an example plot. The data are subject to a weighted fit of the low-pass filtering corrected Eq. 3.9 plus an offset to compensate for non-resolved higher modes and experimental error. Fit errors are determined from Monte Carlo simulations in which test MSD data sets are generated from the real data using the computed errors. The test data sets are subjected to the same fit, and the standard deviation of the fit parameters is taken as an estimate of the error.

The fit yields the low-pass filtering corrected first mode saturation level of the MSD, the first mode relaxation time τ_1 , and the offset. For measurements on grafted microtubules, only data sets were used where the MSD adequately resolved the dynamics. All stiffness estimates were based on the saturation level of the MSD and Eq. 1.32.

3.3 Measurements on free filaments

3.3.1 Microtubule shape tracking

From an optical viewpoint, tracking the transverse position of an extended filament is no more demanding than tracking the position of a point source. Practical problems however arise from the fact that only a limited labelling density can be achieved on a thin strand while a small bead can hold thousands of fluorophores. In addition, fluorophores decorating a filament are exposed to the solution and hence are prone to bleaching.

The basic algorithm implemented here consists of the following steps:

1. Threshold and segment the image to identify individual microtubules. Let the user select a microtubule in the first frame if more than one segment was found.
2. Cut out a region of interest (ROI) that tightly contains the selected segment. Overwrite other segments with the median intensity value of the image. Find the approximate orientation of the selected filament by 2D least squares fitting of a line through the pixels of maximum intensity for all rows and columns of the image.
3. Rotate the image such that the orientation of the filament is horizontal, and fit a Gaussian profile to each column.
4. For the remaining images, the same procedure is carried out for the segment with the center of mass closest to that of the previous one. A size cut-off is used to prevent erroneous tracking of small particles of denatured protein.

Fig. 3.6 illustrates the process using an example.

In some situations, it was necessary to apply further processing such as background subtraction and smoothing for reliable segmentation. Depending on the signal-to-noise ratio and other image quality factors such as defocus, the resolution achieved by this simple procedure is on the order of $1/8$ - $1/2$ of a pixel, corresponding to 30-100 nm. It is likely that the precision could be further improved by the expanding the tracking procedure, but such steps were not pursued because, as will be clear from Figs. 3.8 & 3.10, the limiting factor for the resolution is not the fitting algorithm, but the time resolution.

3.3.2 Mode amplitude extraction

The eigenmodes $W(s)$ described in Section 1.3.2 describe the shape of a filament in terms of the transverse position $y(s)$. In principle, however, an

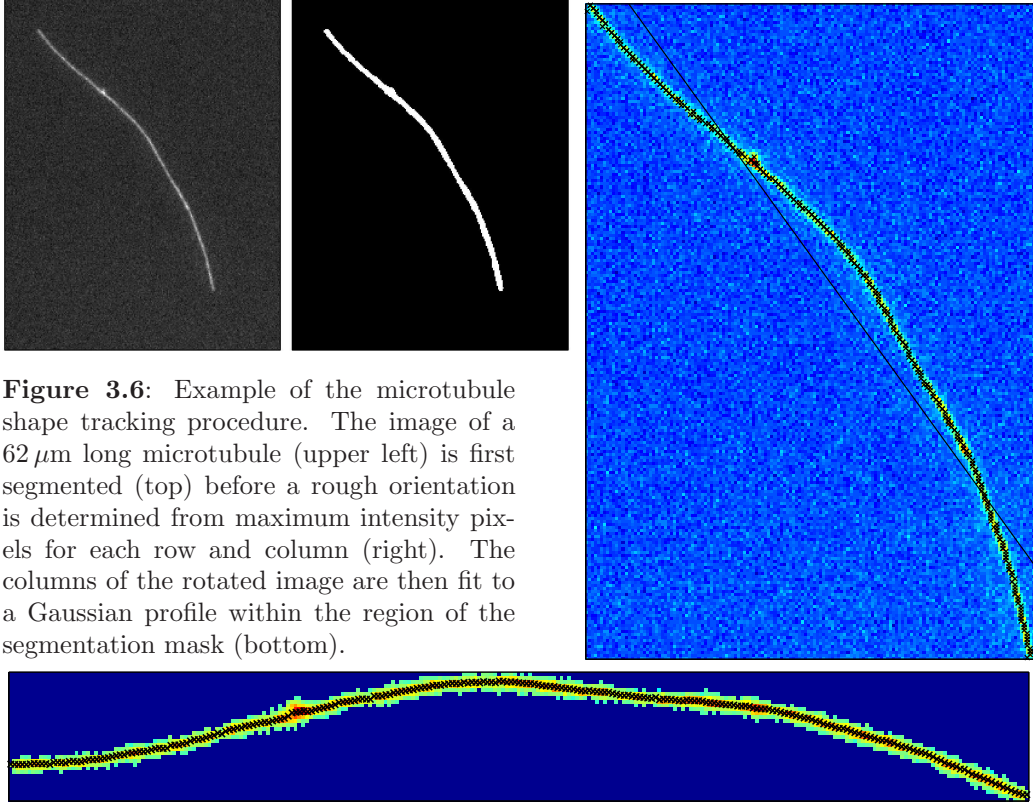


Figure 3.6: Example of the microtubule shape tracking procedure. The image of a $62\,\mu\text{m}$ long microtubule (upper left) is first segmented (top) before a rough orientation is determined from maximum intensity pixels for each row and column (right). The columns of the rotated image are then fit to a Gaussian profile within the region of the segmentation mask (bottom).

analogous description in terms of the bending angle θ is also possible [10]. The bending angle is the angle between the tangent $\overrightarrow{t(s)}$ of the filament and its longitudinal axis,

$$\overrightarrow{t(s)} = \begin{pmatrix} \cos \theta \\ \sin \theta \end{pmatrix} \quad (3.19)$$

Previous studies on the thermal fluctuations of free filaments have preferred an analysis in terms of the bending angle rather than the position [10, 66, 90]. Such a description does not require the longitudinal axis of the filament to be defined which can be an ambiguous task for filaments as soft as actin which were addressed in some of these studies [10, 90]. It does, however, have the disadvantage that angles are a differential measure and hence are inherently noisier than positions.

For microtubules, the bending angle are small and the filament is generally close to straight. This makes it much easier to assign a longitudinal axis for the filament while increasing the influence of position errors on angular measures. We therefore employ a mode decomposition based on transverse positions rather than tangent angles in this study. The longitudinal axis is defined by a simple linear fit to the extracted position coordinates. This

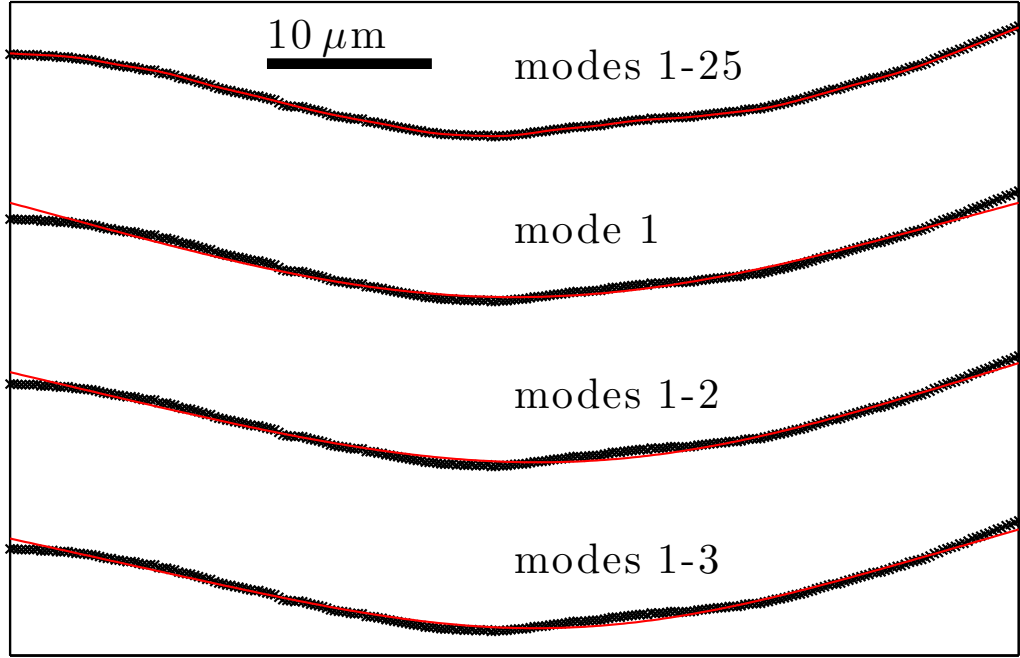


Figure 3.7: Mode decomposition of the microtubule traced in Fig. 3.6. The black symbols represent the raw data and the red line the decomposition result for the indicated modes. The first mode contributes the largest amplitude and already provides a good fit. 25 modes (top) capture the shape almost perfectly.

approach is validated by tests on artificially generated filament shapes as well as the rapid convergence (see Fig. 3.7) and a clear separation of the dynamics for different modes (see Fig. 3.9) that is obtained from the experimental data.

Because the eigenmodes $W(s)$ described in Section 1.3.2 describe the shape of the filament in terms of the parameter s rather than the Cartesian longitudinal coordinate $(x, y(x))$, a high order polynomial is fit through the extracted Cartesian coordinates $y(x)$ obtained from the fit in order to determine the pathlength s along the contour.

In principle, Eq. 1.19 could be used to then extract the mode amplitudes. In practice, however, it more precise to determine a least-squares solution based on Eq. 1.18. This is probably because $y(s, t)$ is only known at discrete positions along the contour while the orthogonality statement in Eq. 1.20 is based on the integral of a smooth function. Since the expression is linear in the mode amplitudes, the problem reduces to a set of linear equations which is easily solved using MATLAB's matrix division tool. Fig. 3.7 shows an example shape decomposition. Convergence can be seen to be fast. Typically, the first 20 modes were included, but only the first few are used to extract mechanical parameters.

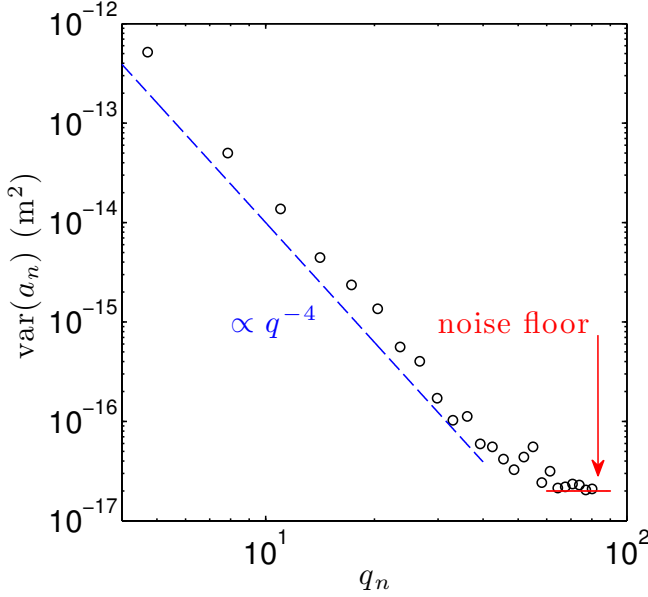


Figure 3.8: Mode amplitude variances of the first 25 modes for a movie of 300 frames of the microtubule shown in Fig. 3.6. Mode amplitudes initially decay roughly according to the power law expected for thermal fluctuations (compare Eq. 1.31) before levelling off to a plateau that is dominated by position noise. The level here corresponds to a standard deviation of 4 nm on the mode amplitude. Given that about 260 points contributed to this value, the noise on the individual points can be estimated to be about 70 nm, that is about 1/3 of a pixel.

Fig. 3.8 shows an example of the variances of the mode amplitudes plotted against mode number q_n for one data set. It is evident that position noise only becomes the dominant factor for very high modes, and the average of their mode variances can be used as an estimate of the noise. Typically, this noise lies in the nm range for the mode amplitudes. Because many position data points, typically 100-200, contribute to any extracted mode amplitude, the noise on the mode amplitudes is much smaller than the error on the individual position data points. The Central Limit Theorem can be applied to estimate the underlying position noise. Extraction of mode amplitudes from simulated filament shapes with defined position noise $\sigma^2(y_e)$ confirm that the resulting amplitude noise follows the expression

$$\sigma^2(a_e) = \sigma^2(y_e)/m, \quad (3.20)$$

where m is the number of position measurements along the filament.

3.3.3 Extracting mechanical parameters

Eq. 1.31 allows the extraction of a persistence length estimate l_p^n for each mode n :

$$l_p^n = \frac{L^3}{q^4 \sigma^2(a_n)}. \quad (3.21)$$

Because of the error sources discussed in Section 3.1, several corrections and error considerations are in order.

Limited sampling means that if all m measurements of a_n are independent, there is a stochastic relative error of $\sqrt{\frac{2}{m-1}}$ on the measured variance. In addition, the measured mode amplitude variance is larger than the true variance by an offset contributed by position determination noise (see Eq. 3.13). This offset can be determined from the variance of the highest measured modes (see Fig. 3.8) and subtracted from the measured amplitude variances. In the analysis, only modes are considered with a measured variance at least 10 times larger than the contribution from position noise.

More often, however, the factor limiting the usefulness of a mode is low-pass filtering. Typical exposure times for epifluorescence measurements of microtubule shapes lie in range of tens of ms. Relaxation times for a free filament however decrease with the inverse 4th power of the mode number. In order to judge whether a mode is affected by low-pass filtering or be able to correct for it, the corresponding relaxation time needs to be known. If the drag ζ is known, then the relaxation time can be inferred as the time τ that fulfils Eqs. 3.7, 3.8, 1.29, and 1.31:

$$\frac{\sigma^2(a_{n,m})\zeta L}{Wk_B T} = \left(\frac{2}{\alpha^2} - \frac{2}{\alpha^3} (1 - e^{-\alpha}) \right). \quad (3.22)$$

where $\alpha := W/\tau$. Since all parameters on the left are known, α and hence τ can be solved for numerically.

A priori knowledge of the drag coefficient ζ is however not easily possible. A reasonable estimate in this case is the expression for a cylinder moving at low Reynold's number in the vicinity of a surface [91]:

$$\zeta \approx \frac{4\pi\eta}{\ln(\frac{4h}{d})}, \quad (3.23)$$

where η is the viscosity of the surrounding medium, h is height of the cylinder above the surface, and d is its diameter. Since in this case the microtubule is in the vicinity of both the top and the bottom coverslip, one may introduce another factor of 2 into this equation [54]. It is, however, unlikely that this equation will give a precise estimate. Not only is the distance h to the two coverslips not precisely known because of variations between different sample chambers and even within one sample chamber, but previous studies have also noted excess drag at low wavelengths that was attributed to internal friction [54, 90].

A safer approach then lies in determining the relaxation times τ_n directly from measurements. This is possible only if the frame rate f is at least as

fast as $\approx 1/\tau_n$. In this case a meaningful MSD can be computed which allows for the extraction of the relaxation time. As this requirement conflicts with the requirement for independent data points for good sampling in the face of a limited photon budget, for some microtubules two movies with different sampling rates were recorded.

Fig. 3.9 shows example plots for MSDs obtained for the same microtubule as in Fig. 3.6. The error bars on the MSD are computed using the blocking procedure [88] discussed in Section 3.1.2. The lines show weighted fits of the low-pass filtering-corrected expression in Eq. 3.9 with an offset matching the average amplitude variance of the 5 highest modes to account for position error. Error estimates on the fits are obtained from Monte Carlo simulations as described in Section 3.2.2.

The fit of the MSD not only yields relaxation times but also an estimate of the amplitude variance of the bending fluctuations from the saturation level of the MSD. This value can also be used to compute a persistence length estimate for the respective mode using Eq. 1.31.

Fig. 3.10 shows persistence length estimates obtained from one movie with the various corrections applied. The following conditions are plotted:

1. Black x: Raw estimates are directly derived from Eq. 3.21 with an error estimate solely based on sampling error assuming all 300 frames to contribute independent measurements (compare Section 3.1.2, Eq. 3.11).
2. Blue +: Blue crosses mark estimates that are corrected for the presence of position errors according to Eq. 3.13. Error estimates contain sampling error as above as well as an error estimate from possible misjudging of the position noise. Only data are considered where the measured mode amplitude variance is at least 10 times larger than the position noise contribution.
3. Triangles: These show estimates based on an assumed friction law taking into account external friction (cyan) or external as well as internal friction (green). Values are extracted using the numerical procedure in Eq. 3.22. Error estimates are computed as above with a modification in the computation of the sampling errors. Instead of treating all m frames as independent, Eq. 3.11 is evaluated for a number of data points equal to $\frac{m}{f\tau}$.
4. Red circles: These are results based on MSD fits. For modes where the movie allows for an MSD extraction, the saturation level of the MSD is used as measure of the amplitude variance. This values is implicitly corrected for low-pass filtering because the fit corrects for it. For modes

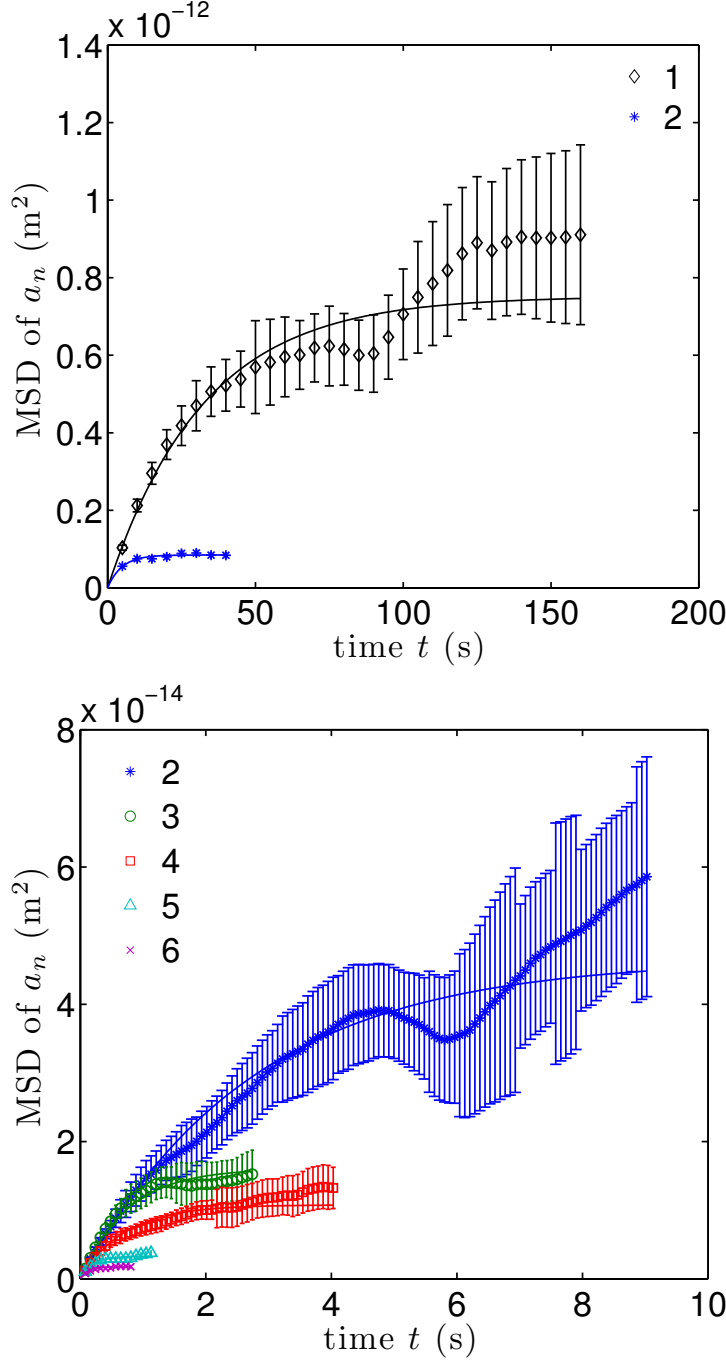


Figure 3.9: MSDs of mode amplitudes obtained from two movies of the same microtubule as in Fig. 3.6. The slower movie (top, frame rate $f = 0.2$ Hz, exposure time $W = 44$ ms) resolves the dynamics of the first two modes, but fails to capture any mode faster than the second mode. The faster movie (bottom, $f = 12.41$ Hz, $W = 24$ ms) resolves the MSD of higher modes, but fails to sample sufficiently long to capture meaningful data for the first mode. The error bars account for errors due to correlation and sampling, and nicely illustrate how correlations produce deceptively smooth curves though being subject to large errors (see Section 3.1.2). The fits (shown as lines) account for both position error and low-pass filtering. The two fits of mode 2, which is resolved in both movies, yield a relaxation time τ_2 of 4.8 ± 0.8 s and 2.7 ± 0.2 s, respectively.

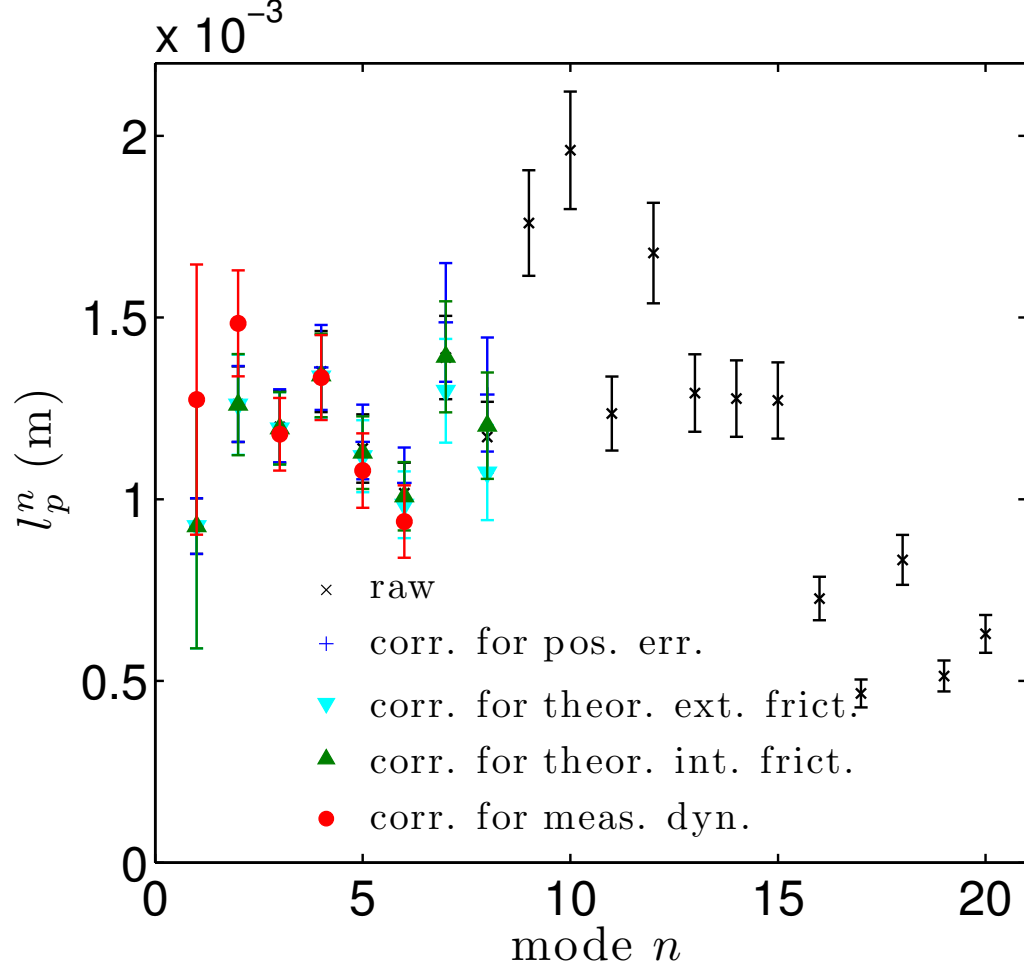


Figure 3.10: Example for persistence length estimates and corrections for the slower movie of the microtubule shown in Fig. 3.6. See text for a detailed description of the difference between different estimates. Raw estimates (black \times) peak around mode 10 due to low-pass filtering. Beyond that regime, the numbers drop because position noise is becoming a major contributor to the amplitude variance. Variability in the estimates obtained from higher modes can also be caused by different sensitivity of the modes to the presence of small rotations. The data presented in Section 4.2.2 exclusively corresponds to stiffness estimates obtained under consideration of dynamics, shown in red here.

where only a different movie yielded an MSD, values are based on the position error-corrected variance, but low-pass filtering is corrected for using the relaxation times obtained from MSDs of the faster movie and Eq. 3.8.

Typical features of these plots are relatively consistent l_p estimates for the lowest modes, then a regime where the l_p estimates increase due to low-pass filtering decreasing the measured mode amplitude variance, before a position noise comes to dominate the mode amplitude variance and l_p estimates decrease to zero.

Chapter 4

Results and Discussion

4.1 Grafted microtubules

4.1.1 Taxol microtubules

Stiffness is not a material constant

The Wormlike Chain Model assumes the bending stiffness κ , and hence the persistence length l_p , to be a material parameter, and as such it cannot depend on extrinsic parameters. Amid the dozens of studies on the bending stiffness of microtubules, however, evidence has surfaced repeatedly that the measured stiffness does in fact depend on the length of the microtubule under consideration.

In 1995, Kurachi et al. [69] bent microtubules with optical tweezers and found power law dependencies on filament length, with exponents between 1 and 2. Using a similar technique, Takasone et al. [63] show an approximately quadratic dependence on length. Kis et al. [70] deformed microtubules using atomic force microscopy, observed a similar length dependence and suggested that the apparent bending stiffness scales with L^2 due to shear contributions arising from slippage between protofilaments. More recently, Pampaloni et al. [59] used the same method as in the present study and concluded that the measured persistence length scales with L^2 up to $L \approx 20 \mu\text{m}$ from where on it approaches a plateau. Many other studies, however, find no evidence of a length-dependent scaling [10, 65], or attribute the scaling they find to bias arising from limitations in their measurement strategy [90].

Fig. 4.1 shows stiffness measurements obtained for taxol microtubules in the present study. The first obvious feature is that, similar to several previous experimental studies [59, 90], the scatter is larger than the error bars. This scatter is due to true heterogeneity in the microtubule population and not due to measurement errors. Repeat measurements on the same microtubule generally reproduce the measured result within error, ruling out sampling errors as the source. In addition, Sections 4.1.2 & 4.1.5 will present further evidence validating the experimental approach and pointing towards true mechanical diversity.

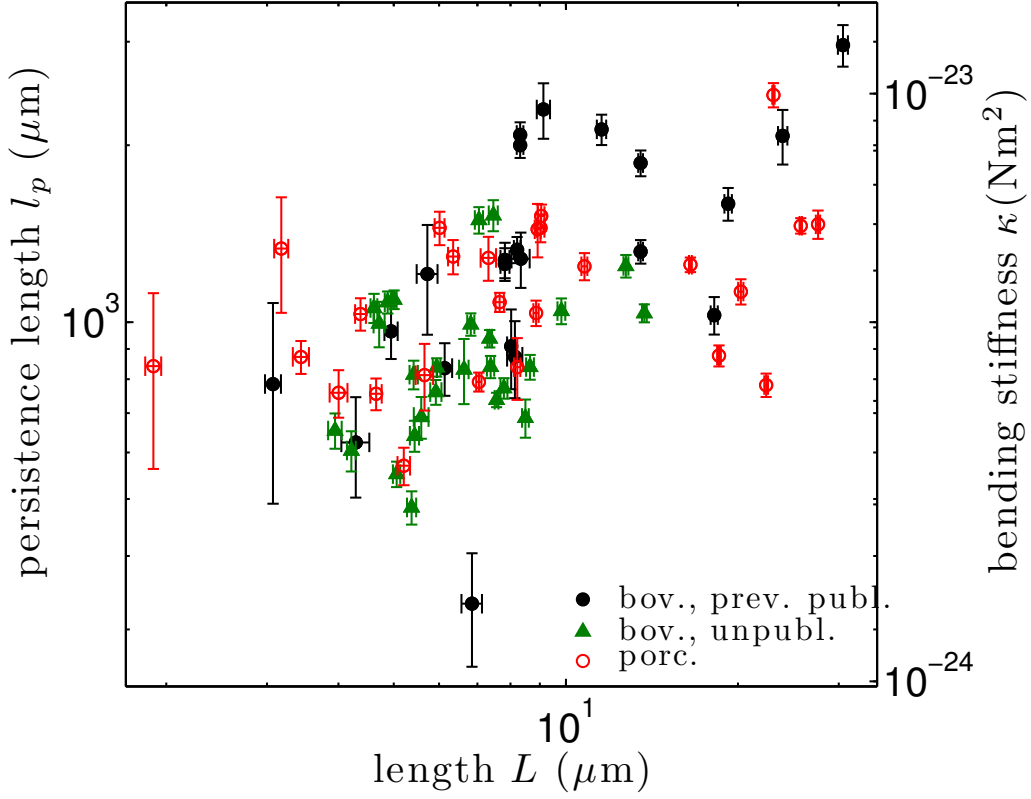


Figure 4.1: Stiffness of taxol microtubules plotted against filament length. Persistence length l_p and bending stiffness $\kappa = l_p k_B T$ are shown on opposite axes. A subset of the data (filled circles) have been published previously in modified form [71, 83]. While the present data were computed from the saturation level of the MSD as described in Section 3.2.2, the previous analysis [71, 83] used the full position variance which is less accurate. One measurement included in the previous study had to be omitted here because the dynamics were insufficiently resolved to perform the three parameter fit employed here. Data from porcine microtubules (open symbols) follow a similar trend as those for bovine microtubules (filled symbols). The stiffness values show a trend to increase with increasing length (correlation coefficient 0.55).

Beyond the experimental scatter, the data show a clear trend to increase with increasing length. The correlation coefficient for the data shown is 0.55. Because the present study used the same assay as Pampaloni et al. [59], and, like those authors, finds a dependence of bending stiffness on length, the present data are compared to those obtained in their study.

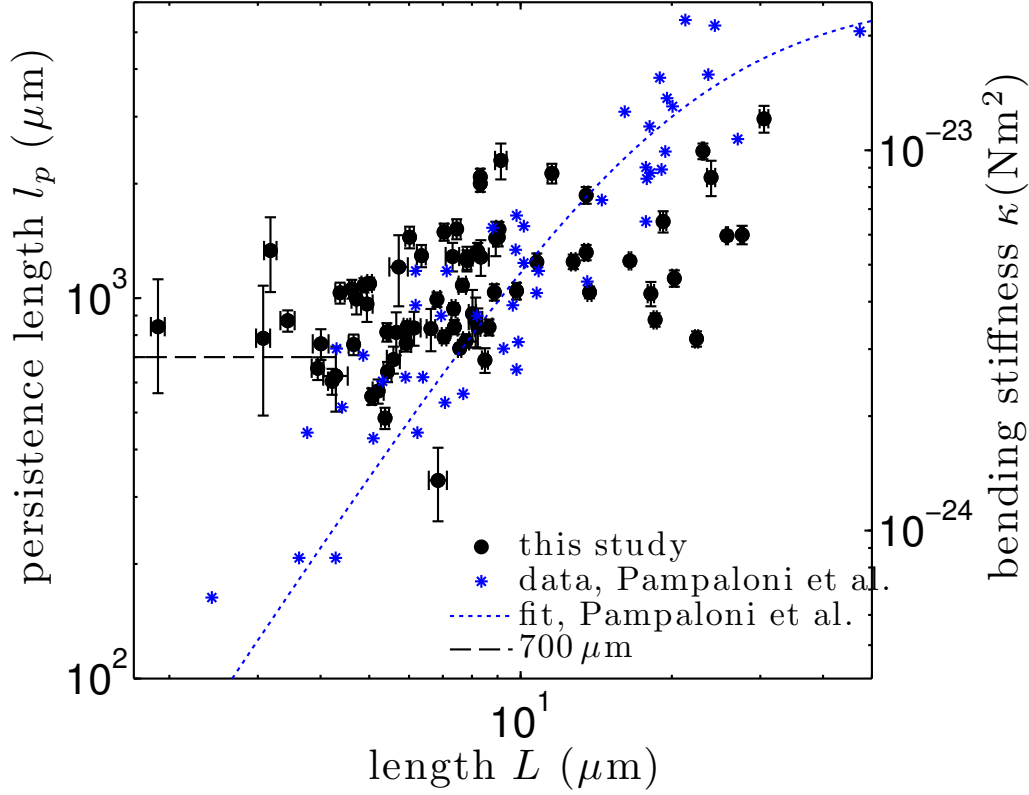


Figure 4.2: Stiffness of taxol microtubules plotted against filament length. The black symbols show the same data as in Fig. 4.1. The blue stars and line represent the experimental data and fit obtained by Pampaloni et al. [59]. The experimental data from the present study fall roughly into the same range as theirs, but markedly diverge from it in the short length regime, where the values seem to level into a plateau. The weighted average of the 8 values for length $L < 4.3 \mu\text{m}$ is $704 \pm 25 \mu\text{m}$. For long microtubules, the data of Pampaloni et al. show a continuation of the length dependence while the present study finds lower values and more scatter.

Comparison with the data of Pampaloni et al. [59]

Fig. 4.2 shows an overlay of the results obtained by this study and by Pampaloni et al. [59]. Markedly, the data found by those authors show a more pronounced dependence on length (correlation coefficient 0.87). While both data sets show a similar tend to increase with increasing length in the range from $\sim 4 - 10 \mu\text{m}$, the results deviate on both ends of this interval.

In the long length regime, Pampaloni et al. report larger stiffness values than the present study. It is however questionable whether the authors correctly took into account sampling errors. For their longest microtubule with $L = 47.5 \mu\text{m}$, they report $l_p = 5035 \mu\text{m}$. A microtubule with these properties

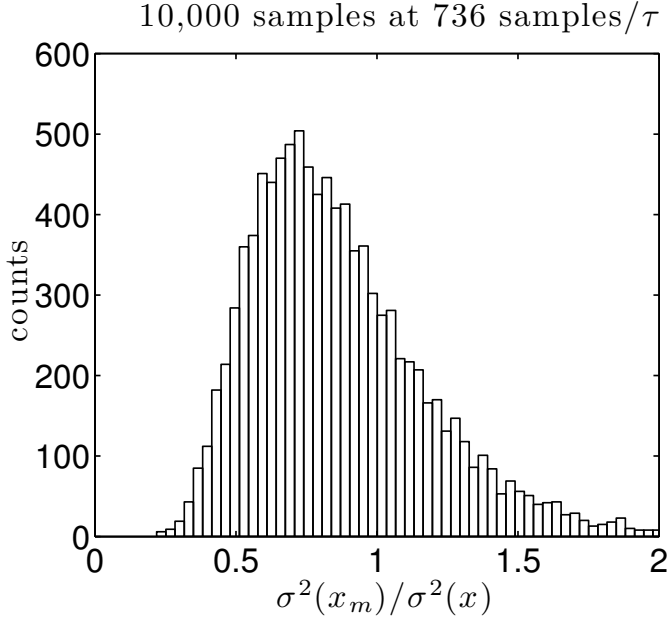


Figure 4.3: Monte Carlo simulations of a random walk in a harmonic potential with sampling parameters comparable to those used for the longest microtubule in Ref. [59]. A histogram of the ratio of sample variance and true variance shows that not only is the measurement likely to underestimate the variance, it is also subject to random error with a standard deviation of $\sim 30\%$.

is expected to have a relaxation time of $\tau_1 = \frac{L^4 \zeta}{q_1^4 l_p k_B T} \approx 46$ s, assuming a drag coefficient of $\zeta = 2.3 \times 10^{-3} \text{ Nsm}^{-2}$ (see Fig. 4.9). If 10,000 frames were collected at 16 Hz as stated in the study’s Materials and Methods section, the total sampling time would equate to less than 14 first mode relaxation times. A set of simple Monte Carlo simulations reveals that if a random walk in a harmonic potential is sampled for such a short duration, the expected sample variance will be $\sim 13\%$ smaller than the true value. In addition, the expected error on the sample variance will be $> 30\%$, which contrasts markedly with the small error bars in Fig. 3 in Ref. [59], suggesting less than 10 % error. Fig. 4.3 shows a histogram of the sample variances obtained in 10,000 Monte Carlo runs of this scenario. Even if 5 times as many frames as reported had been obtained, the resulting error would still be at least twice as large as indicated. It is therefore quite likely that the values Pampaloni et al. [59] report for long microtubules are not only overestimating the persistence length, but are also subject to much larger errors than reported.

The deviations between the two studies in the short length regime, however, cannot easily be explained by measurement errors. While the values found here seem to level into a plateau of around $700 \mu\text{m}$, Pampaloni et al. find a continuation of the decrease. For their shortest microtubule, Pampaloni et al. report a length of $2.6 \mu\text{m}$ and a persistence length of $l_p = 110 \mu\text{m}$. Given that they used Eq. 1.33, this implies that the standard deviation of the transverse position fluctuations was $0.23 \mu\text{m}$. Assuming typical values for the magnification, this value corresponds to ~ 2 pixels on the detector, a

value large enough so that it should be easily resolved and not be increased significantly by measurement error.

Low-pass filtering effects in the Pampaloni study can be excluded as the source of the discrepancy, too, because they would bias the measured stiffness towards appearing larger rather than smaller compared to the true value.

It would appear, then, that the differences in measurement results for short microtubules are not due to sampling or measurement error. Apart from biochemical differences in the sample preparation procedures, it is conceivable that there is human bias in the selection of microtubules for measurements. In both studies, microtubule lengths were measured from the edge of the substrate under the assumption that any part of the microtubule covalently grafted to the substrate is unlikely to contribute to the mechanical response. This idealized picture may not be true, and it is conceivable that differences in the attachment conditions lead to a different mechanical response. In the present study, the microtubules chosen for measurement generally were grafted on the substrate along a substantial fraction of their total length such as to avoid confusion with pinned microtubules that would appear artificially soft.

The Timoshenko model

Following a similar argument as laid out by Kis et al. [70], Pampaloni et al. [59] fit an equation of the type

$$l_p = \frac{l_p^\infty}{\left(1 + \left(\frac{\lambda}{L}\right)\right)}. \quad (4.1)$$

and find $l_p^\infty = 6.3 \pm 0.8 \text{ mm}$ and $\lambda \approx 21 \text{ } \mu\text{m}$. Both bending and shear contributions are taken into account in the derivation of this equation, and the parameter λ reflects the relative contributions of the two, by being proportional to the ratio of the Young's modulus E and the shear modulus G :

$$\lambda = \frac{3EI}{GkA}, \quad (4.2)$$

where k is a geometrical factor, A is the cross section area of the microtubule, and I is the second area moment of the cross section as before (see Section 1.3.2). The parameter l_p^∞ is the asymptotic limit for $L \rightarrow \infty$ where the microtubule acts as a fully coupled beam and shear contributions become irrelevant:

$$l_p^\infty = \frac{EI}{k_B T} \quad (4.3)$$

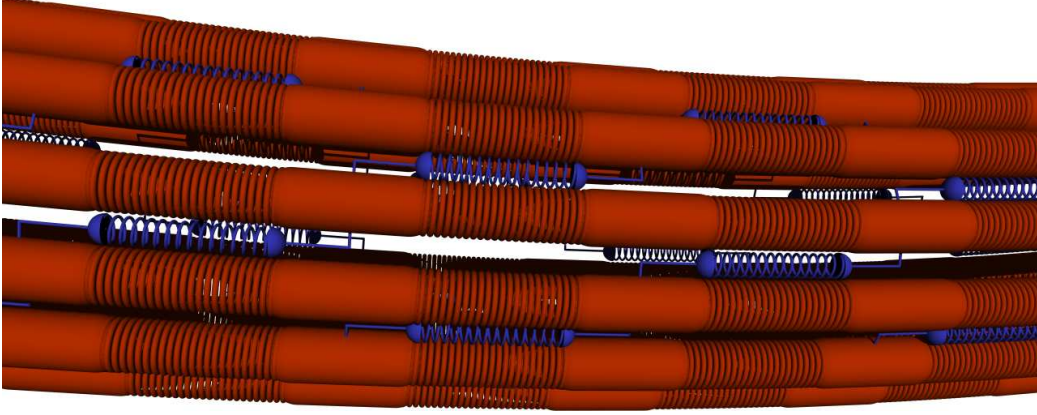


Figure 4.4: Schematic of the Wormlike Bundle Model. Constituent fibres (red) are linked into a bundle by shear springs between each other (blue). The individual fibres have both a bending stiffness and are extensible.

The rationale is that because shear and bending deformations scale differently with length, shorter microtubules are increasingly subject to shear between protofilaments weakening their mechanical response. The frame work is equivalent to the concept of so-called Timoshenko beams known in the engineering literature [92].

Upon closer inspection, however, it becomes apparent that the short length limit of this model is not physical. Intriguingly, this regime is where the data in the present study deviate most significantly from the model proposed by Pampaloni et al. With $L \rightarrow 0$, the model predicts l_p to vanish. Intuitively, by contrast, one would expect a finite lower limit of the stiffness set by the stiffness of the individual protofilaments. The model presented by Pampaloni et al., however, is based in continuum elasticity theory and must break down at this length scale.

The Wormlike Bundle Model

Heussinger et al. [5, 6] have presented an extension of the Wormlike Chain Model (WLC) which they call the Wormlike Bundle Model (WLB). The model follows a similar rationale of considering both bending and shear contributions, but is built from a microscopic rather than a continuum mechanics perspective.

It envisions the mechanics of a bundle of fibres coupled by shear springs, and describes each individual constitutive fibre as an extensible Wormlike Chain. Fig. 4.4 shows a schematic. The necessity of extensibility arises because, in analogy to continuum mechanics, in a bent bundle, the innermost

fibres would be expected to be compressed while the outer ones would be stretched. So the extensibility of the individual fibres mirrors the use of the Young's modulus in Eq. 4.3. In addition to fibre extensibility and shear between fibres, the fibres are also endowed with an intrinsic bending stiffness κ_f . If the fibres truly were made of a homogeneous isotropic material as envisioned in the Wormlike Chain Model, both their bending stiffness and their extensibility would be governed by their Young's modulus. The same does not necessarily need to be true for filaments on a molecular scale where assumptions of heterogeneity and isotropy fail.

These considerations lead to three types of energy terms being relevant to the mechanical description of the assembly, accounting for stretching, bending and shear. Heussinger et al. show that these terms lead to an effective bending stiffness κ for the bundle that is a function of length. In case of the tubular geometry relevant for microtubules, they find [6]

$$\kappa = N\kappa_f \left(1 + \frac{1}{\frac{\kappa_f}{b^2} \left(\frac{8 \sin^2(\pi/N)}{k_s \delta} + \frac{q_n^2 \delta}{L^2 k_x} \right)} \right). \quad (4.4)$$

Here k_s and k_x are the microscopic force constants of the stretching and shear springs, δ is their spacing along the fibres, b is the lateral distance between the fibres, and N is the number of fibres, or, in the case of microtubules, protofilaments.

Fig. 4.5 shows a plot of the length-dependent bending stiffness predicted by this model. The graph shows three distinct scaling regimes. Analogously to the Timoshenko model, a plateau value is predicted for very long microtubules that is dependent on stretching elasticity, while an L^2 scaling in an intermediate regime is governed by shear contributions. The two regimes are separated by the critical length scale L_x :

$$L_x^2 = \frac{k_s}{k_x} \frac{\delta^2}{8 \sin^2(\pi/N)}, \quad (4.5)$$

which is conceptually equivalent to the length scale λ/q_n in the Timoshenko model. In contrast to the Timoshenko model, however, the Wormlike Bundle model predicts a lower limit for the effective bending stiffness equal to the sum of the bending stiffnesses of the constituent protofilaments. This effect is dominant for lengths shorter than

$$L_b^2 = \frac{\kappa_f}{k_x} \frac{\delta}{b^2}. \quad (4.6)$$

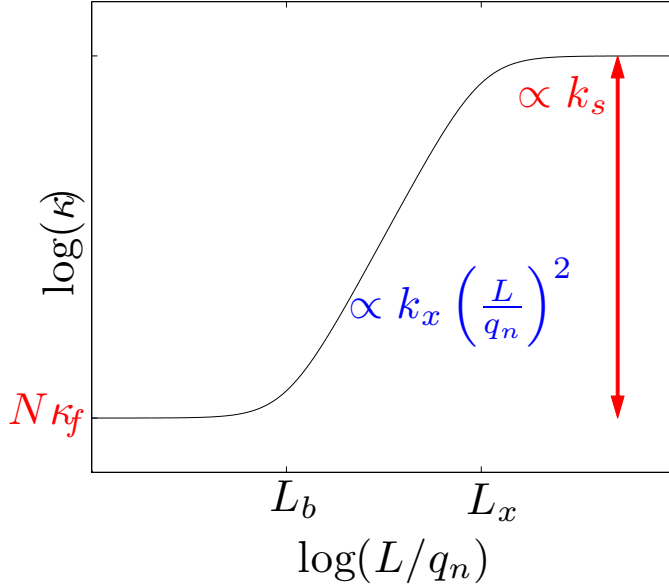


Figure 4.5: Effective bending stiffness κ in the Wormlike Bundle Model [5, 6]. The stiffness is a function of length with three distinct regimes, each dependent on only one aspect of the underlying structure. Two plateau values at either end of the range depend only on properties of the constituent fibres, while the intermediate L^2 regime is dominated by contributions from shear between them.

Eq. 4.4 can then be rewritten as

$$\kappa = N\kappa_f \left(1 + \frac{1}{\frac{L_b^2}{L_x^2} + \frac{q_n^2 L_b^2}{L^2}} \right). \quad (4.7)$$

An interesting feature of Eq. 4.4 is that the expression does not only depend on length L , it more specifically depends on L/q_n . Because the q_n are set by the boundary conditions, this implies that the measured stiffness for a microtubule of a given length can depend on how the measurement was performed. In addition, it implies that different modes should have different stiffnesses within the L^2 scaling regime. As a result, the tangent-tangent correlation function likely would not show a well-defined exponential decay anymore as in Eq. 1.6, making the definition of the persistence length less obvious. The term persistence length should therefore be understood in the following not as the characteristic tangent autocorrelation length scale, but as derived from the effective bending stiffness via Eq. 1.7.

A lower limit for the persistence length of short microtubules

Given that the Timoshenko model is unphysical for short lengths, it is plausible that the stiffness plateau found in the length regime $< 4 \mu\text{m}$ represents the lower limit predicted by the WLB model, referred to as l_p^0 from hereon. The weighted average of the data points for the shortest 8 filaments measured (up to a length of $4.3 \mu\text{m}$) is $704 \pm 25 \mu\text{m}$. Assuming that a microtubule

has 13 protofilaments, this would lead to a value of $\sim 55 \mu\text{m}$ for the persistence length of an individual protofilament. If protofilaments were made of a homogeneous material, it would be possible to compute a Young's modulus $E = \kappa/I$ from this value. Assuming a radius of $r = 2 \text{ nm}$ and $I = \pi r^4/4$, one obtains $\sim 18 \text{ GPa}$. This value contrasts with that of $\sim 1.5 \text{ GPa}$ obtained by Pampaloni et al. [59] from their value of $l_p^\infty = 6300 \pm 800 \mu\text{m}$ for the stretch dominated stiffness of long microtubules. It should be noted, however, that not only do these estimates depend on the 4th power of geometrical parameters that are not exactly determined, but they also correspond to different deformation modes of the tubulin protein. It is not clear that a protofilament's resistance to bending and to stretch are related to each other as would be the case for a homogeneous material. Both numbers seem reasonable though given that α -helices were found to have a Young's modulus of $\sim 1.2 \text{ GPa}$ [93], while for silk fibres, which also consist of proteins, a modulus of over 30 GPa was reported for the linear regime [94].

Interestingly, two recent studies also find evidence that very short microtubules have a small, but non-vanishing persistence length: van den Heuvel et al. [95, 96] use gliding assays to probe the persistence length of only the very tips of microtubules and find values of only 240 ± 30 and $80 \pm 20 \mu\text{m}$. These values are somewhat smaller than the value of $700 \mu\text{m}$ indicated by the present data, but as already the difference by a factor of 3 between the two values suggests, the technique used by these authors is very challenging to calibrate. In addition, the data from the present study is subject to large errors in this length regime mainly because the use of fluorescence microscopy limits the temporal resolution, and low-pass filtering effects become larger and increasingly difficult to correct for. If, however, these short microtubules really had a persistence length as low as the values found by van den Heuvel et al., their fluctuations would be slower and the present assay would not have difficulties resolving them.

Parameters dependence of the WLB stiffness

One of the most appealing features of the WLB model is that the three distinct scaling regimes predicted for the effective bending stiffness each depend almost exclusively on only one of the three energy contributions considered in the model. This separation can be exploited in order to link changes in the mechanical properties to changes in the molecular contacts at specific sites in the microtubule lattice.

Fig. 4.6 shows schematically how the WLB stiffness response changes when specific input parameters change. A stiffening of the shear coupling between protofilaments k_x should only result in a shift of the L^2 scaling

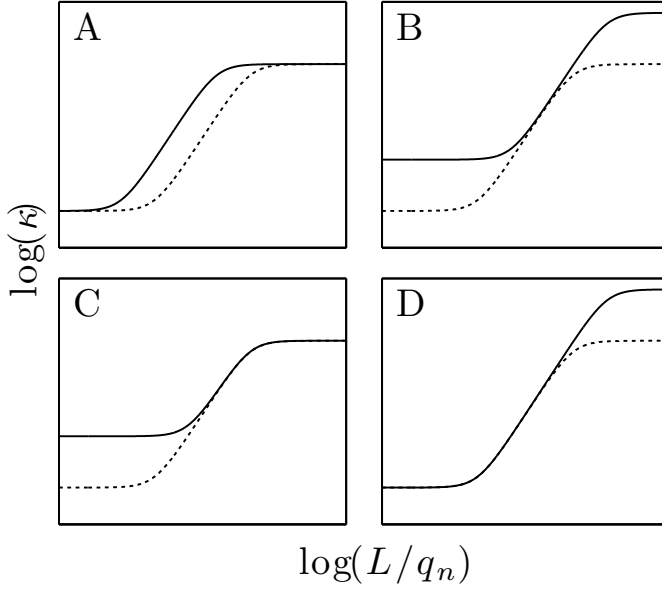


Figure 4.6: WLB stiffness dependence on input parameters. The solid line represents the following changes relative to the dotted line: A) a decrease in the shear coupling k_x ; B) an increase in both the bending stiffness κ_f and the stretching stiffness k_s of the constituent fibres; C) an increase only in κ_f ; D) an increase only in k_s . The physically most plausible scenarios are A and B.

regime to the left (see Fig. 4.6 A), extending the high stiffness plateau to shorter filament lengths. A change in the longitudinal contacts within fibres, however, would only affect their bending stiffness κ_f (Fig. 4.6 C) or their extensibility k_s (Fig. 4.6 D) or both (Fig. 4.6 B), leaving the intermediate shear-dominated regime unaffected.

If the fibres could be modeled as homogeneous elastic beams, then both k_s and κ_f would be determined by their Young Modulus E . While this strict coupling need not be applicable for molecular scale fibres such as protofilaments, one would still expect that to first order, changes in protofilament properties that lead to a change in k_s would also similarly affect κ_f . The ratio of these two parameters also determines the ratio l_p^∞/l_p^0 :

$$\frac{l_p^\infty}{l_p^0} = 1 + \frac{\delta b^2}{8 \sin^2(\pi/N)} \frac{k_s}{\kappa_f}. \quad (4.8)$$

As the expression does not depend on k_x either, it seems that it would be difficult to devise a mechanism that would alter l_p^∞/l_p^0 . The physically most likely scenarios in Fig. 4.6 would then be depicted in A and B. In Section 4.1.4, we will apply this logic to the comparison of mechanical properties for microtubules polymerized with different nucleotides.

Dynamics deviate from the Wormlike Chain model

Given that the bending stiffness of microtubules does not turn out to be the material constant envisioned by the Wormlike Chain Model, it stands to

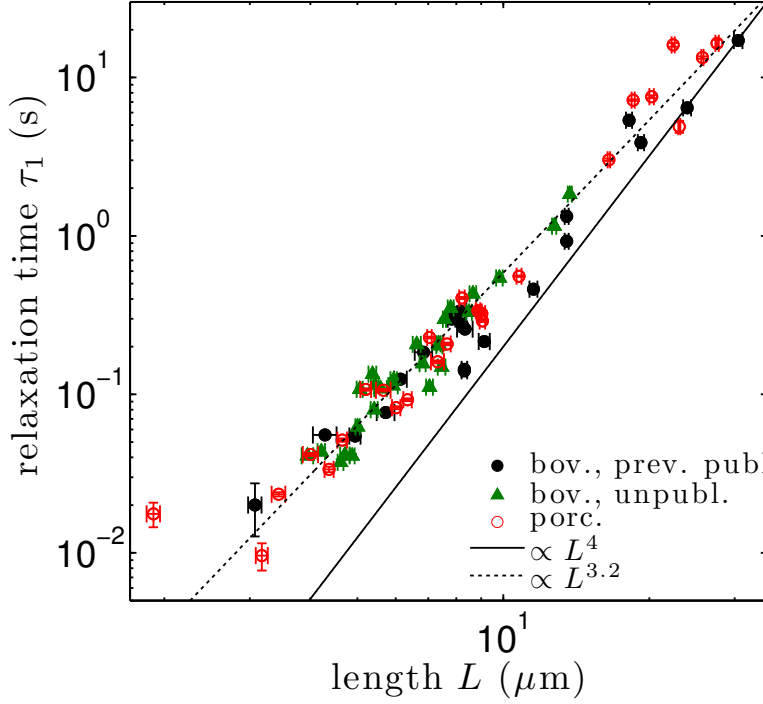


Figure 4.7: Relaxation dynamics for taxol microtubules deviate from the L^4 scaling predicted by the Wormlike Chain Model. The best power law fit yields an exponent of ~ 3 . A subset of the data (filled circles) was previously published in Refs. [71, 83].

reason that the relaxation times should also deviate from the predicted L^4 scaling of Eq. 1.29.

As was previously reported in Refs. [71, 83], that is exactly what the data reveal (Fig. 4.7). While the data for microtubule lengths $L > 10 \mu\text{m}$ do not seem to significantly stray from the L^4 behaviour expected from the Wormlike Chain Model, the data for shorter microtubules deviate markedly. The best power law fit for the entire data set yields an exponent of ~ 3 . If, however, these two regimes are fit separately as shown in Fig. 4.8, one finds that the scaling across the range is not uniform. The length dependence for the shorter microtubules seems shallower, while that for longer microtubules approaches the L^4 scaling of the Wormlike Chain Model.

If Eq. 1.29 still holds, then a shallower length dependence is exactly what is expected from a stiffness that decreases with decreasing length. In the regime of very short lengths, however, where Fig. 4.1 shows a levelling of the length dependence, one would expect the dynamics to return to the L^4 scaling expected for a constant stiffness. That this is not the case implies that the drag coefficients are exhibiting anomalous behaviour as well.

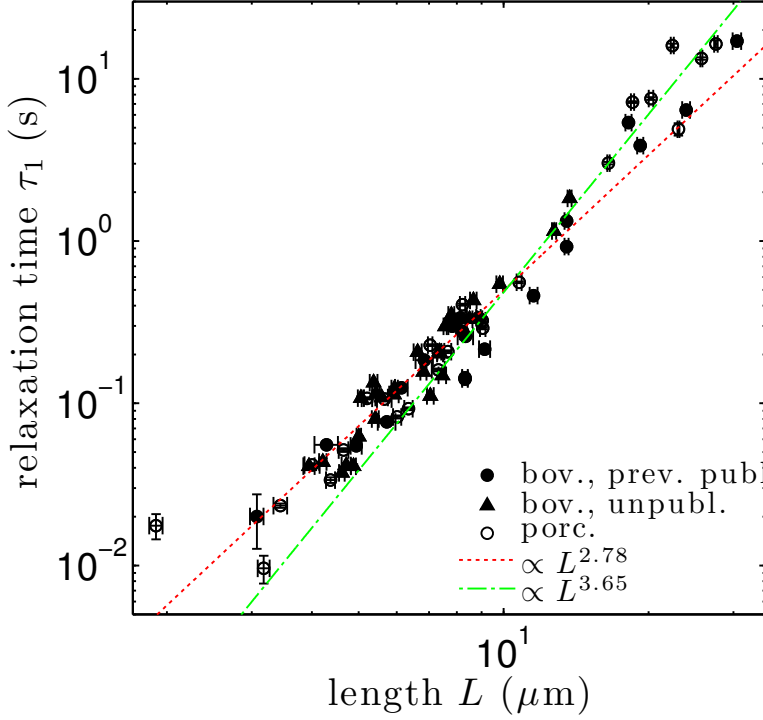


Figure 4.8: When the regimes above and below $10 \mu\text{m}$ are fit separately, it becomes apparent that the long length regime is closer to the L^4 scaling while the shorter length regime follows a shallower scaling.

Internal friction dominates drag for short microtubules

A reasonable estimate of the drag per unit length experienced by a microtubule fluctuating in solution is that of a slender cylinder held in a steady flow at low Reynolds number [97]:

$$\zeta_{\text{th}} = \frac{4\pi\eta}{\ln(L/d) + 2\ln(2) - 0.5}, \quad (4.9)$$

where η is the viscosity of the medium and d is the diameter of the cylinder. Since this function only depends on the logarithm of the length, it is not expected to significantly alter the functional dependence for the relaxation times τ .

Having measured both τ and l_p , it is possible to compute the drag per unit length ζ from Eq. 1.29. Fig. 4.9 shows the result. Several features of this graph are notable. First, it is remarkable how smooth the data are in comparison to the stiffness data in Fig. 4.1. While persistence length estimates for microtubules with a length of $10 \mu\text{m}$ can differ by a factor of three, and a similar scatter is present in the relaxation time data in Fig. 4.7, drag coefficients cluster around a relatively well-defined line and show little scatter. This consistency underscores that the scatter obtained for the stiffness is real and not due to measurement error or flaws in the rationale of the analysis.

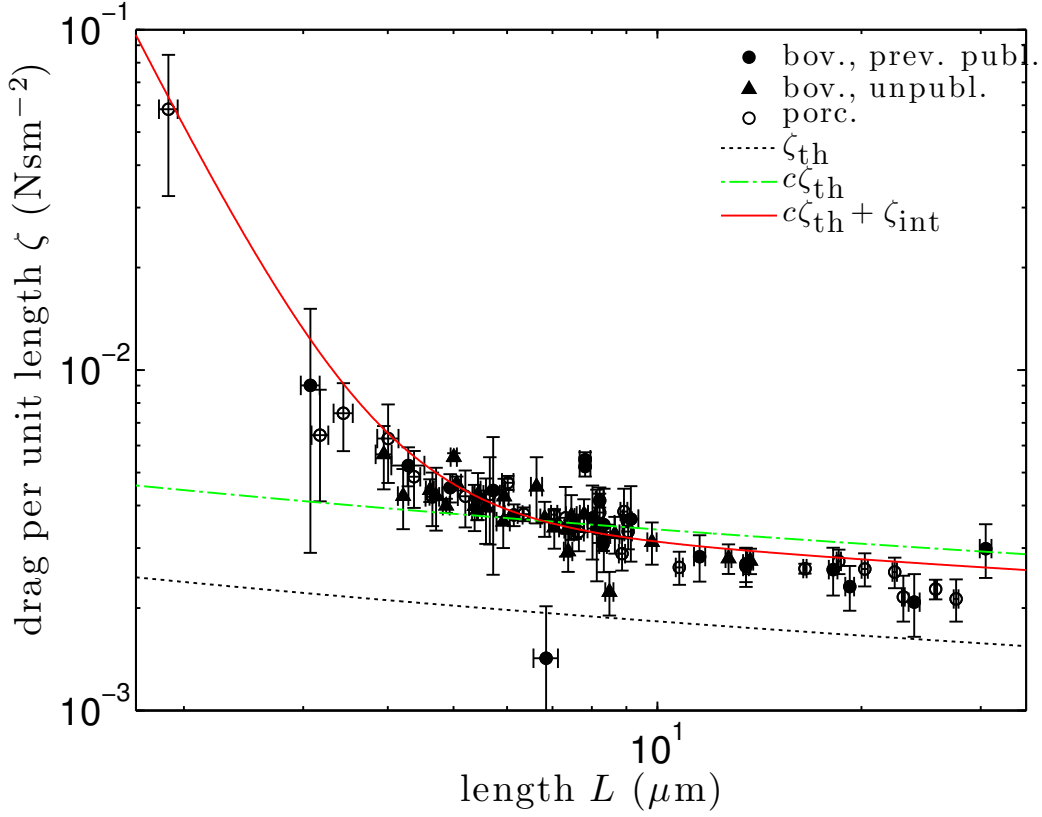


Figure 4.9: Friction contributions for taxol microtubules. The data are well explained by hydrodynamic friction (Eq. 4.9) for microtubules longer than $\sim 5 \mu\text{m}$, but deviate sharply from this model for shorter lengths. The steep rise in this regime can be explained by the presence of internal friction (Eq. 4.10). A subset of the data (filled circles) was previously published in Ref. [83].

Secondly, for long microtubules, the data are, apart from a multiplicative factor, in fair agreement with the rough estimate of Eq. 4.9. For shorter microtubules, however, a sharp increase away from the hydrodynamic estimate is evident. The increase is well fit if, in addition to Eq. 4.9, a term accounting for internal friction is taken into account. Poirier & Marko [98] showed that additional dissipation inside a bent filament, be it due to conformational changes or due to fluid molecules being squeezed through pores in the filament, would result in an effective friction term proportional to $(q_n/L)^4$. This scaling results from the assumption that internal dissipation is proportional to the rate of the bending deformations. A fit of the equation

$$\zeta = c\zeta_{\text{th}} + \zeta_{\text{int}} = c \frac{4\pi\eta}{\ln(L/d) + 2\ln(2) - 0.5} + \epsilon \left(\frac{q_1}{L} \right)^4 \quad (4.10)$$

with $q_1 = 1.875$ yields $c = 1.67 \pm 0.02$ and $\epsilon = (6.2 \pm 0.4) \times 10^{-26} \text{ Nsm}^2$.

Internal friction contributions in the fluctuation dynamics of microtubules have also been detected in shape analysis studies by Janson & Dogterom [54] as well as Brangwynne et al. [90] who find values of $\epsilon = 6.9 \times 10^{-25} \text{ Nsm}^2$ and $1.6 \times 10^{-24} \text{ Nsm}^2$, respectively. These two values, while being reasonably close to each other, are more than an order of magnitude larger than the value observed here.

This discrepancy is puzzling because the two studies differ from each other in their approaches but each share features with the present assay. Janson & Dogterom study unlabelled, dynamic microtubules with grafted boundary conditions, while Brangwynne et al. observe fluorescently labelled, taxol-stabilized microtubules with free ends. There are only two obvious common features of the two studies that are not shared by the present one. Firstly, both other studies analyze higher modes in long microtubules, while the present study observed first mode fluctuations in shorter microtubules. It is however not clear why the physical mechanisms generating internal friction should be different in the two cases. Secondly, both other studies observe microtubules in close proximity to coverslips where hydrodynamic coupling already causes the drag to be increased by almost an order of magnitude compared to the microtubules in this study that were more than $10 \mu\text{m}$ away from the coverslip. An external hydrodynamic cause of the excess friction does however seem unlikely because of the characteristic L^{-4} scaling.

A curious feature is that the rise in drag per unit length is seen at around the same lengths as the plateau in stiffness estimates. Given that other, biochemically modified microtubules seem to share a similar friction behaviour without associated stiffness effects as will be shown in Section 4.1.2, this coincidence is probably not due to a systematic effect. Interestingly, if the regime of length-dependent stiffnesses did extend into the regime dominated by internal friction, one would expect relaxation times to start to increase with increasing mode number! It is at present unclear whether such a scenario would be physical.

4.1.2 GMPCPP microtubules

GMPCPP microtubules are much stiffer than taxol microtubules and do not show length-dependence

Fig. 4.10 shows stiffness estimates for GMPCPP microtubules from several different lots compared to the previously shown taxol data. Because bovine and porcine taxol microtubules showed similar values, those data were combined.

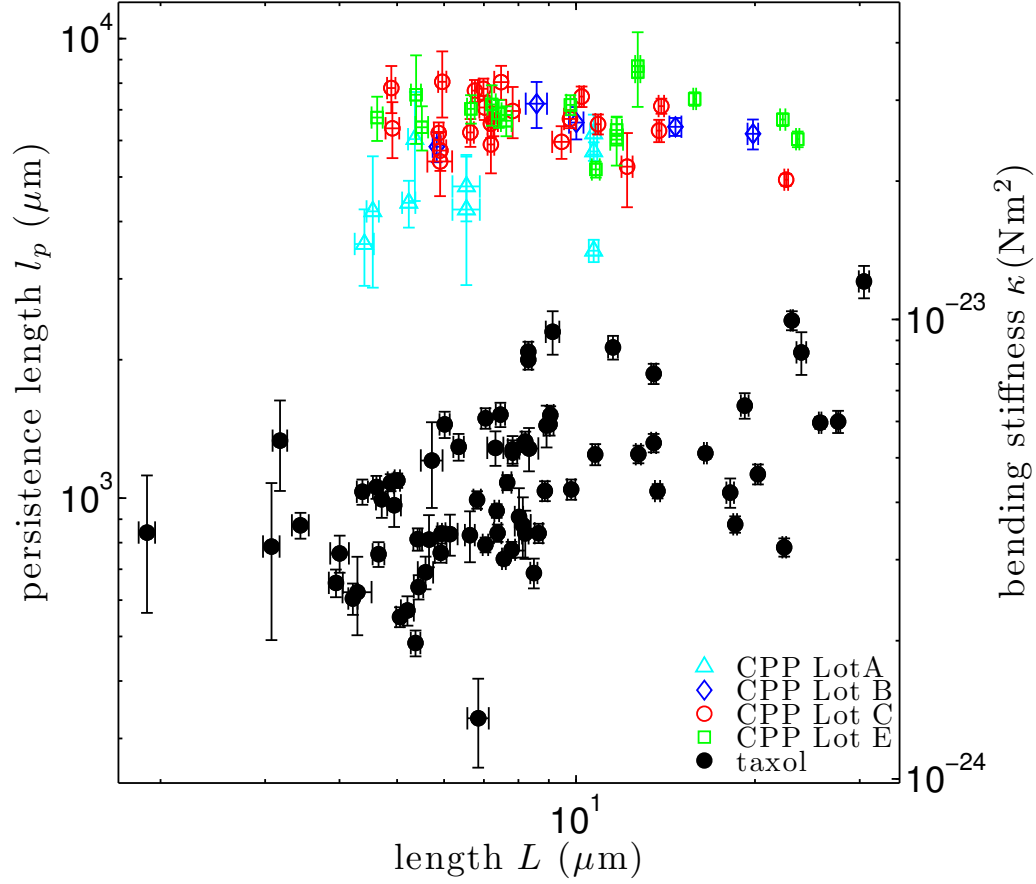


Figure 4.10: Stiffness of GMPCPP microtubules compared to taxol microtubules. Data from bovine and porcine taxol microtubules from Fig. 4.1 were combined as there were no evident differences between the two species.

Clearly, the GMPCPP microtubules are much stiffer. Their persistence lengths lie in a range about 6 times larger than those obtained for taxol microtubules, making measurements for short microtubules much more challenging. The rapidly decreasing relaxation times (see Fig. 4.12) prevent fluctuations of GMPCPP microtubules shorter than $\sim 4.5 \mu\text{m}$ from being resolved, therefore data for this length regime is not available.

In addition to the increased stiffness, the GMPCPP data, with the exception of Lot A, do not seem to show length-dependence. This first lot may be subject to systematic differences though because the chemical protocol for producing tubulin with a high GMPCPP content was still in the development phase. In particular, the preparation for this first lot differed from later ones in that it included only a cold and not a calcium-induced

depolymerization step (see Section 2.1.2). It is likely that this resulted in a higher fraction of GDP tubulin among the GMPCPP tubulin. Because the three later lots produced quite consistent results (see Table 4.1), subsequent analyses merging the results from different GMPCPP lots will discard the results from Lot A.

Lot	$\mu(l_p)$ (μm)	$\sigma_{\text{SE}}(l_p)$ (μm)	$\sigma(l_p)$ (μm)
A	4350	140	1030
B	6330	190	510
C	6200	80	900
E	6650	90	880

Table 4.1: Average persistence lengths and errors for the different GMPCPP lots. μ refers to the weighted mean, and σ_{SE} is the associated standard error of the mean, while σ is the standard deviation.

Comparison to literature values

Only few previous studies have attempted quantitative measurements on the stiffness of GMPCPP microtubules. Mickey et al. [66] report a stiffness of $6.2 \pm 0.9 \times 10^{-23} \text{ Nm}^2$ which is about twice as large as the values found here. Interestingly, the values they report for taxol microtubules are also several times larger than the values found here, pointing to systematic differences between their study and the present one. Kawaguchi et al. [99] in turn report GMPCPP microtubules of lengths 5-20 μm to show a slightly length-dependent stiffness of $0.8 - 1.5 \times 10^{-23} \text{ Nm}^2$, values about half as large as presented here. Neither study makes a statement with respect to the expected purity in nucleotide content for their GMPCPP microtubules, so it is difficult to judge whether the different results may be due to composition. Hyman et al. [78] report variable GMPCPP incorporation ratios up to 0.85, with the remainder presumably being GDP. Müller-Reichert et al. [25] report GMPCPP incorporation ratios up to 0.9.

While Mickey et al. [66] follow the procedures of Gittes et al. [10] who are admirably thorough in their analysis, Kawaguchi et al. [99] employ a measurement strategy that is more error-prone. From only 60 frames recorded at a fixed frame rate, they trace the free end of a grafted microtubule undergoing thermal fluctuations. On the lower end of the length regime they study, their results imply a standard deviation of 150 nm for the free tip, that is likely too small to be accurately resolved by tracing the tip manually, making underestimates of the stiffness due to measurement error likely. On the longer end of the length regime, their stiffness results for 20 μm long microtubules imply a first mode relaxation time of 1.7 s which is only minimally shorter than the total observation time of 4 s, likely giving rise to an overestimate of the

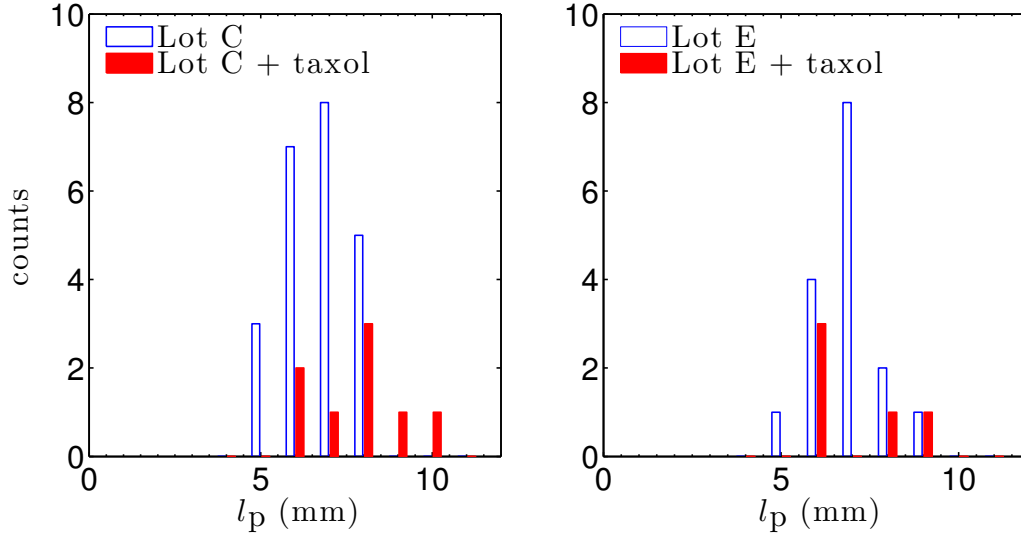


Figure 4.11: Stiffness of GMPCPP microtubules with added taxol for Lots C and E. The difference in mean is smaller than one standard deviation (see Table 4.2).

stiffness due to undersampling. Their observed weak length-dependence may hence be the result of measurement errors. Mickey et al. [66] only measured six GMPCPP microtubules, and presumably obtained a lot of scatter given that their standard error of the mean already corresponds to $\sim 15\%$ of the mean.

Taxol has little effect on GMPCPP microtubules

The taxol/GDP microtubules and the GMPCPP microtubules differ not only in their nucleotide content, but also in the presence and absence of taxol. As some studies have reported evidence that taxol makes microtubules more flexible [67, 68], it is unclear whether it is taxol or the nucleotide that is responsible for the observed difference in stiffness behaviour.

As a first step towards resolving this question, some measurements were performed on GMPCPP microtubules from Lots C and E with added taxol. The resulting data show no significant length dependence and give results very similar to those for GMPCPP microtubules without taxol (see Figs. 4.11 & 4.15).

Table 4.2 shows that the mean values for microtubules of the two conditions are quite similar for the two lots. Curiously, the values for microtubules with taxol are slightly larger. While the effect is statistically significant ($p \approx 0.01$), the difference in means between the two conditions is still smaller than one standard deviation. It is therefore unlikely that the presence or

l_p (μm)	Lot C	Lot E
+taxol	$7030 \pm 140(1490)$	$7350 \pm 170(1550)$
-taxol	$6200 \pm 80(900)$	$6650 \pm 90(880)$

Table 4.2: Average persistence lengths and standard errors for GMPCPP microtubules with and without taxol. The values are given as $\mu \pm \sigma_{\text{SE}}(\sigma)$.

absence of taxol causes the large difference in stiffnesses between GDP/taxol and GMPCPP microtubules seen in Fig. 4.10.

It is however not obvious that the effect of taxol on GMPCPP microtubules is comparable to the effect on GDP microtubules. The ultimate test would be a measurement on GDP microtubules without taxol, but since those microtubules are not stable this measurement is not possible with the current assay. If, however, the nucleotide is the main cause of the observed effect, then intermediates between the pure GDP and pure GMPCPP lattice should yield an intermediate in stiffness. This avenue of inquiry will be pursued in Section 4.1.3.

GMPCPP microtubules show WLC dynamics

If, as Fig. 4.10 suggests, the stiffness of GMPCPP microtubules can be considered constant, then the relaxation times should follow the L^4 scaling expected from the WLC model. Fig. 4.12 shows a plot of the first mode relaxation times obtained for GMPCPP microtubules with and without taxol as well as the data for taxol microtubules previously shown in Fig. 4.7. The observed scaling with length is close to the L^4 expected for a constant stiffness. Deviations are most obvious for short microtubules where for taxol microtubules increased drag was observed and attributed to internal friction.

GMPCPP microtubules show stronger internal friction than taxol microtubules

Fig. 4.13 shows that GMPCPP microtubules show similar drag coefficients to taxol microtubules. As before, the long range regime is captured fairly well by the hydrodynamic description, but for short lengths a rapid increase away from that line can be seen. A fit of Eq. 4.10 yields $\epsilon = 11.2 \pm 1.4 \times 10^{-26} \text{ Nsm}^2$ and $c = 1.65 \pm 0.03$. While the parameter c is unchanged compared to that found for taxol microtubules, the parameter ϵ is about twice as large, so the GMPCPP microtubules are subject to at least as much internal friction as taxol microtubules. A factor of two however is not a huge deviation in the fit of a power law. With $2^{1/4} \approx 1.18$, it corresponds to a less than 20% change in the critical length where the contributions from hydrodynamic and internal

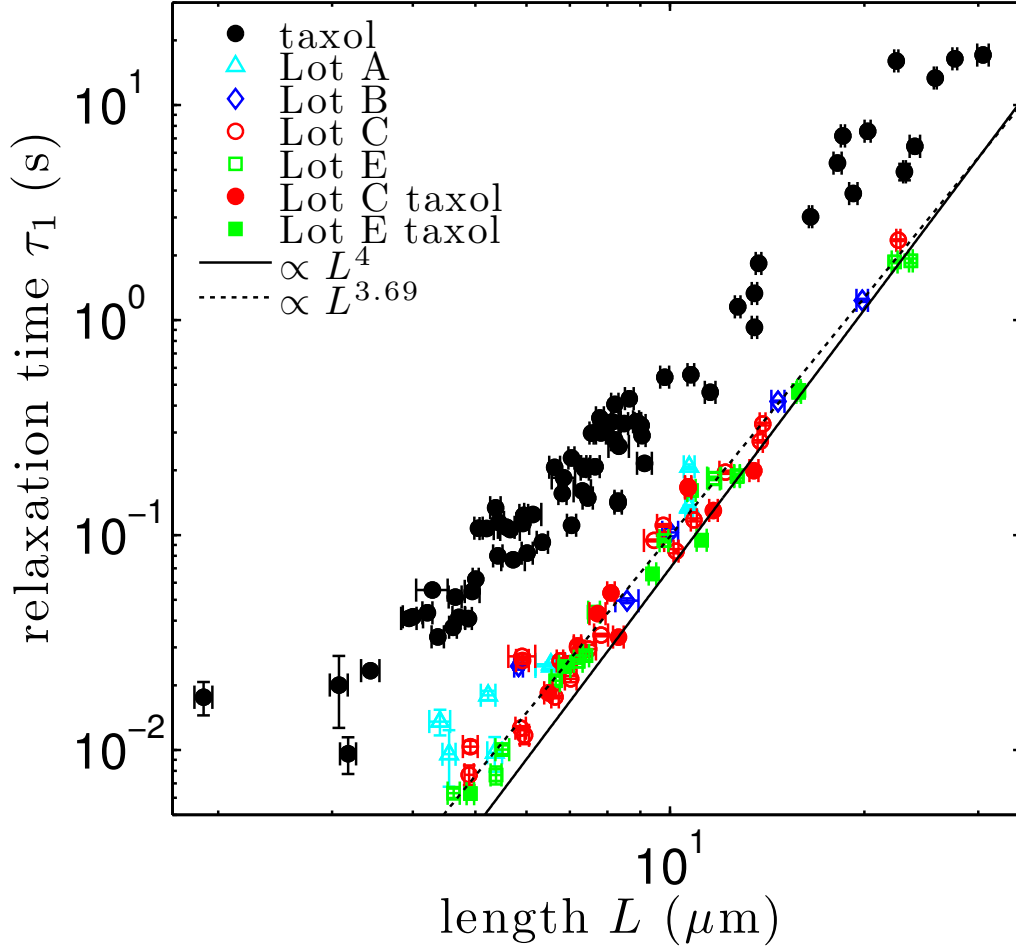


Figure 4.12: First mode relaxation times for GMPCPP microtubules. The taxol data previously shown in Fig. 4.7 and a slope of 4, expected from the WLC model, are shown for comparison. The best power law fit to the data from Lots B, C and E is slightly shallower (dotted line), probably due to effects caused by the drag coefficient.

friction become equal, from $3.8 \mu\text{m}$ in the taxol to $4.5 \mu\text{m}$ in the GMPCPP case.

It is unclear whether the presence of taxol makes a difference in the friction behaviour. Fig. 4.14 presents the data obtained for GMPCPP microtubules with and without taxol. The taxol data seem to show a larger scatter, but do not reach to lengths sufficiently short to unambiguously tell whether they follow the same steep rise there.

Both the L^{-4} scaling of the internal friction contributions as well as their weak dependence on biochemical modifications may yield clues with respect to their sources. Because a small change was observed as a consequence

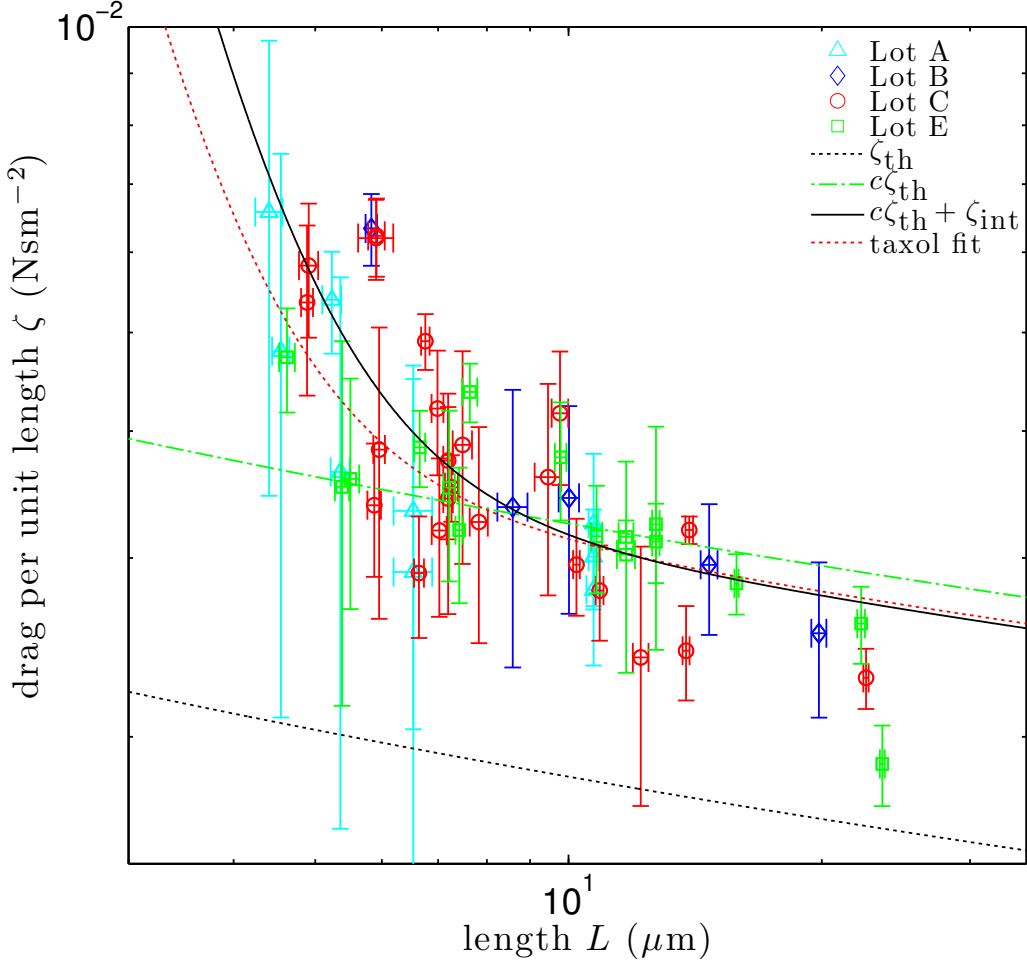


Figure 4.13: Drag coefficients for GMPCPP microtubules. The black line is a fit of Eq. 4.10 to the data from Lots B, C and E. The red dotted line shows the best fit for internal friction in taxol microtubules as shown in Fig. 4.9. The present fit yields an internal friction parameter about twice as large as the one obtained for taxol microtubules.

of nucleotide state, one might expect that the interprotofilament bonds are governed

4.1.3 Mixed nucleotide microtubules

Great care was taken to ensure a very high GMPCPP content for the microtubules discussed in Section 4.1.2. It is however easily possible to polymerize microtubules from a mixture of GTP and GMPCPP, thereby creating a mixed lattice of GDP and GMPCPP. If the nucleotide is responsible for the differences observed between GMPCPP and taxol/GDP microtubules, then such

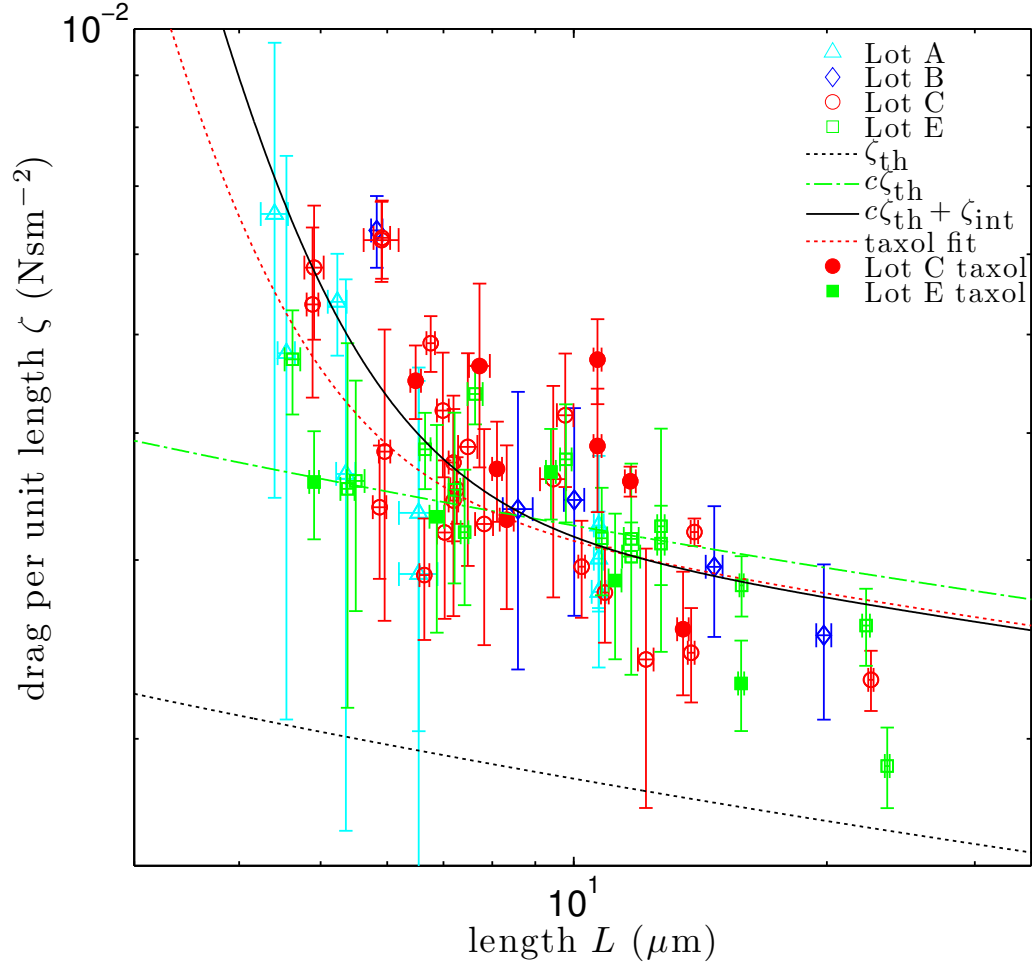


Figure 4.14: Drag coefficients for GMPCPP microtubules with and without taxol. The plot is identical to the one in Fig. 4.13 except for the addition of data points for GMPCPP microtubules with taxol. These data points show a little more scatter, and it is not clear whether they are also subject to internal friction.

an intermediate state would be expected to show an intermediate response in stiffness.

The mixed nucleotide microtubules created here had a sufficiently high GMPCPP content for the microtubules to remain stable for several hours. It is not easy however to estimate the GMPCPP/GDP ratio in the lattice. Two main avenues of reasoning could be applied: 1) If both the nucleotide concentrations at polymerization and the binding affinities for incorporation of nucleotides into tubulin dimers as well as those for incorporation of nucleotide-bound tubulin into microtubules were known exactly, an estimate could be attempted. Not only would this estimate disregard the fact that

some turnover of microtubules is likely to occur over time, turning some of the GTP into GDP, but it already fails because the numbers are not known to the required precision. 2) Alternatively, if it were known how many GMPCPP:tubulin dimers are required at the tip of a microtubule to prevent it from undergoing catastrophe, a probabilistic estimate could be attempted based on catastrophe rates and the known hydrolyzation rate of GMPCPP in the microtubule lattice. Unfortunately, the chemical requirements for a stabilizing cap are still under debate [31]. A quantitative estimate is hence not feasible a priori. It does however seem quite likely that the nucleotide content is significantly different to that of the microtubules polymerized almost purely with GMPCPP because of the observed large differences in stability. The nucleotide content is therefore likely dominated by GDP.

Because of the fragility of the microtubules polymerized with only a small amount of GMPCPP, experiments were more challenging and it was not possible to obtain measurements for the entire length range covered for taxol and GMPCPP microtubules. The results for the accessible length range however are all the more surprising. As shown in Fig. 4.15, the low GMPCPP condition restored the behaviour seen for taxol microtubules. Not only do the values fall into the same range as seen for taxol microtubules, they also show a similar trend to increase with increasing length.

Taxol microtubules are equivalent to GDP microtubules

Given that microtubules with a mixed nucleotide content, that is, with GDP as the dominant nucleotide, display the same stiffness behaviour as taxol/GDP microtubules, it seems that what governs the mechanics of both of these is the GDP rather than the addition of taxol or GMPCPP. Otherwise one would have to assume that, coincidentally, the amount of GMPCPP that the microtubules of the low GMPCPP condition incorporated happened to be exactly the amount that would mimic the effects of taxol.

Nucleotide content affects internal friction

GDP microtubules stabilized with a low amount of GMPCPP not only show similar stiffness values as taxol microtubules, they also exhibit the same friction behaviour. As shown in Fig. 4.16, the drag coefficients for this condition show the same rise at short lengths, and a fit of Eq. 4.10 yields $\epsilon = 5.5 \pm 0.7 \times 10^{-26} \text{ Nsm}^2$ and $c = 1.80 \pm 0.04$, very similar to taxol microtubules. This implies that the bound nucleotide is a regulator of internal friction.

This connection may not seem surprising given that nucleotide hydrolysis

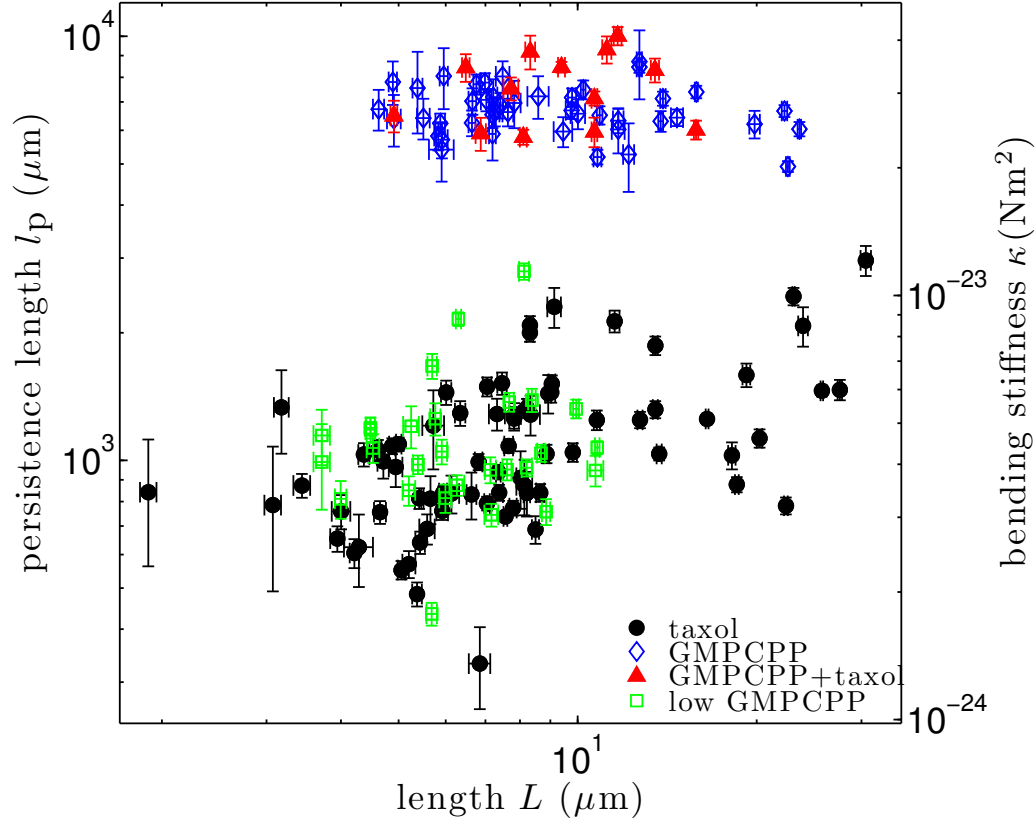


Figure 4.15: Persistence length estimates for microtubules of 4 different chemical conditions: black circles: taxol GDP microtubules, polymerized with GTP and then stabilized with taxol; blue diamonds: polymerized with a high GMPCPP content (includes Lots B, C, and E); red triangles: the same with added taxol; green squares: microtubules polymerized with a mixture of GTP and GMPCPP, presumably containing mostly GDP.

is thought to be coupled to the induction of mechanical strain in the microtubule lattice [100]. Taxol however is thought to stabilize microtubules by relieving internal strain by either straightening dimers [101] or decreasing the stiffness of individual protofilaments [102]. The taxol/GDP microtubules and the low GMPCPP/high GDP microtubules are hence expected to differ in their internal mechanical tension, but they show the same friction response. The mechanism by which GMPCPP increases internal friction would then have to be distinct from that which causes the induction of strain during nucleotide hydrolysis.

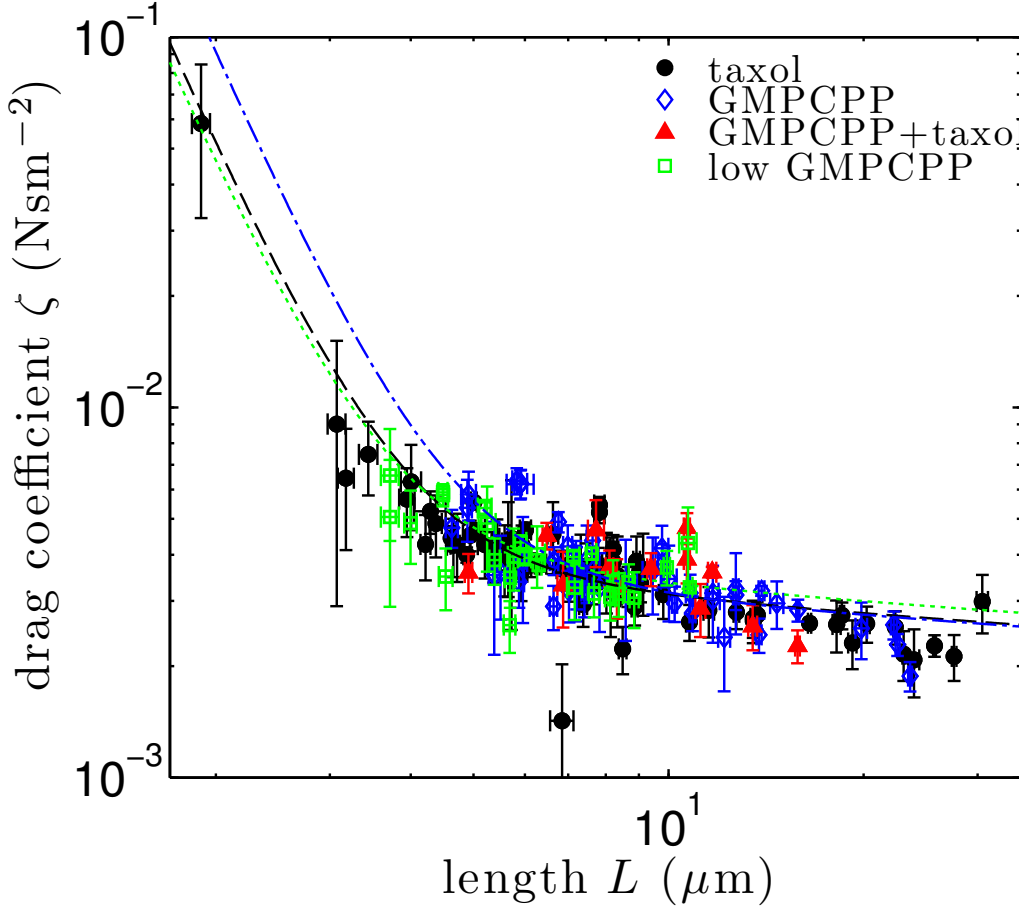


Figure 4.16: Drag estimates for microtubules of 4 different chemical conditions as in Fig. 4.15. The lines show fits according to Eq. 4.10. Microtubules with a low GMPCPP content show the same friction behaviour as taxol microtubules, while microtubules with a high content of GMPCPP show increased friction for shorter microtubules, attributed to an increase in internal friction.

4.1.4 An interpretation based on the Wormlike Bundle Model

Assuming that the Wormlike Bundle Model correctly describes microtubule mechanics, it would seem that the stiffness values observed for taxol microtubules correspond to the regime of l_p^0 and the intermediate shear-dominated $\propto L^2$ scaling regime.

Because the plateau l_p^∞ for long microtubules is not resolved (see Section 4.1.5 for a discussion), it does not make sense to fit the entire expression Eq. 4.7 to the data. If instead one neglects the plateau l_p^∞ and fits an ex-

pression of the type

$$l_p = l_p^0 \left(1 + \left(\frac{L}{q_n L_b} \right)^2 \right), \quad (4.11)$$

$l_p^0 = 670 \pm 20 \mu\text{m}$ and $q_n L_b = 10.3 \pm 0.3 \mu\text{m}$ are obtained. The fit, shown in Fig. 4.17, only includes data points up to a microtubule length of $10 \mu\text{m}$. If one assumes a subunit and interprotofilament spacing $\delta \approx b \approx 4 \text{ nm}$ as well as $N = 13$ and $q_n = 1.875$, then Eq. 4.6 implies a shear coupling force constant of $k_x \approx 2 \times 10^{-6} \text{ N/m}$. This value is extraordinarily small. If k_x were the force constant of a single harmonic oscillator, its thermal position fluctuations would have a standard deviation of

$$\sqrt{\frac{k_B T}{k_x}} \approx 45 \text{ nm}. \quad (4.12)$$

This number corresponds to the length of more than 5 dimers, suggesting that single dimers can be shifted almost arbitrarily longitudinally to each other solely by thermal forces. It should be noted though that protofilaments would feel the restoring forces acting on all dimers along their length on both sides, making thermally induced displacements much smaller. In addition, such a harmonic model would only be applicable for displacements significantly smaller than the dimer length as the energy landscape for protofilaments would have to be periodic.

This high degree of flexibility in the lateral interactions may explain why protofilaments can arrange into a vast array of different structures such as zinc-induced sheets [37], ribbons, and tubes [103], and why microtubules can be found in so many different conformations with respect to protofilament numbers, helix starts, and lattice defects [104].

The nucleotide strongly affects lateral interactions between protofilaments

How would the microtubule lattice have to change in order to yield the high, constant stiffness observed for GMPCPP microtubules? As Fig. 4.6 shows, there are only limited physically plausible scenarios.

The fact that monomers in GMPCPP microtubules have been observed to be $\sim 4\%$ longer suggests that the protofilaments' stiffness might be altered. If k_s and κ_f were equally affected, Eq. 4.8 shows that l_p^∞/l_p^0 would be unchanged, apart from a linear dependence on the subunit spacing δ which would not cause a large effect. The length-dependent regime should then still be visible, unless the coupling k_x between protofilaments was affected, resulting in a shift of the length-dependent regime to shorter microtubule

lengths as in Fig. 4.6 A. If so, the data obtained for GMPCPP microtubules would correspond to the plateau value l_p^∞ .

Intriguingly, the mean stiffness of $6400 \pm 60 \mu\text{m}$ found for GMPCPP microtubules in the present study agrees well with the value $l_p^\infty = 6300 \pm 800 \mu\text{m}$ found for taxol microtubules by Pampaloni et al. [59]. While it may be that the latter value hinges on the potentially error-fraught data point for the longest microtubule, it seems likely that corrected data would yield an estimate that is not too dissimilar in magnitude. The data from the present study are not helpful in resolving this matter because they do not include the l_p^∞ regime. This is likely due to a combination of lack of data for very long microtubules as well as variations in microtubule architecture increasingly disrupting the idealized WLB scaling (see Section 4.1.5).

Regardless of whether or not taxol microtubules and GMPCPP microtubules converge to the same value of l_p^∞ , it is possible to estimate the minimum change in lateral shear coupling k_x that would be necessary to shift the length-dependent regime to microtubule lengths even shorter than the range accessible in the present measurements. The shortest GMPCPP microtubule measured among lots C-E had a length of approximately $4.6 \mu\text{m}$, and its stiffness of $6730 \pm 740 \mu\text{m}$ is no smaller than the values found for longer microtubules. The length scale L_x must then be much smaller than $4.6 \mu\text{m}/q_1$. If we set the condition that at $4.6 \mu\text{m}$ any shear-induced decrease may not be more than 10 % of l_p^∞ , then L_x can be at most $0.78 \mu\text{m}$. Fig. 4.17 shows a visualization of this scenario.

Shear coupling between protofilaments is two orders of magnitude stronger in GMPCPP microtubules

We can then estimate the shear coupling k_x for GMPCPP microtubules using

$$k_x = \frac{l_p^\infty k_B T \delta}{L_x^2 N b^2}. \quad (4.13)$$

With $l_p^\infty = 6400 \mu\text{m}$ and $b \approx \delta \approx 4 \text{ nm}$ as before, we then conclude that for GMPCPP microtubules, $k_x \geq 8 \times 10^{-4} \text{ N/m}$. This value is more than two orders of magnitude larger than the value found for taxol microtubules. Such an extreme change may seem odd at first glance, but is less surprising if put into context.

Taxol microtubules seem mechanically equivalent to GDP microtubules as has been argued in Section 4.1.3. This may not be true across the entire length regime - the short length plateau l_p^0 is not covered in the present experiments - but seems to hold true in the shear-dominated, length-dependent regime. GDP microtubules are not stable and will undergo catastrophe,

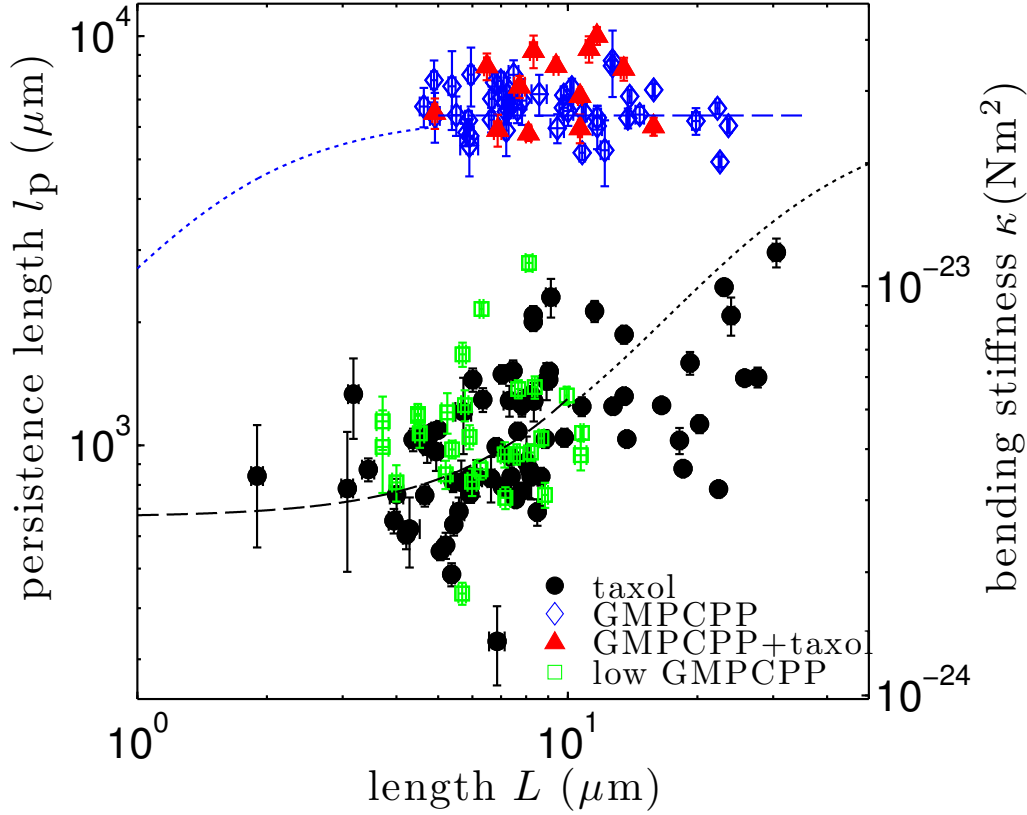


Figure 4.17: The effects of the nucleotide on microtubule stiffness. A fit of Eq. 4.11 (black dashed line) yields a stiffness plateau of $l_p^0 = 670 \pm 30 \mu\text{m}$ for short microtubules and $q_n L_b = 10.3 \pm 0.3 \mu\text{m}$. The saturation predicted for long microtubules is indicated as a black dotted line at l_p^∞ . The blue dash-dotted line indicates the average value of $6400 \mu\text{m}$ found for GMPCPP microtubules. The dotted continuation represents the curve for taxol microtubules shifted to the left, corresponding to an increase in shear coupling.

during which the protofilaments are known to peel away from each other as shown in Fig. 4.18. Clearly then, the attraction between protofilaments cannot be very strong. In contrast, GMPCPP microtubules not only assemble readily like GTP microtubules, they also do not depolymerize. Given this stark difference in polymerization behaviour between the two nucleotide states, it does not seem surprising that there would be a large difference in mechanical properties underlying it.

Implications for dynamic instability

Given that GMPCPP is considered an analogue of GTP, the interactions in the GMPCPP lattice likely mimic the interactions between GTP:tubulin

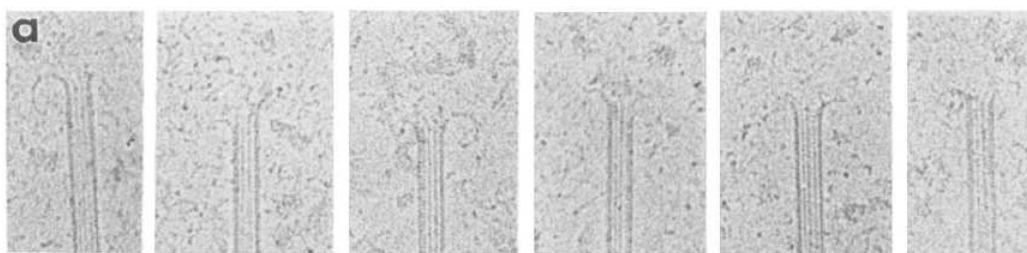


Figure 4.18: EM images of microtubules undergoing catastrophe upon dilution (Fig. 2a from Ref. [105]). The protofilaments can be seen to peel away from each other.

dimers in growing microtubules. With the taxol microtubules putatively providing a mimic of the GDP lattice, the results found here may shed light on the forces underlying microtubule assembly and disassembly.

Recent interpretations concerning the relevance of the nucleotide for the microtubule assembly process have focussed on the curvature of the tubulin dimer. In microtubules undergoing catastrophe, the GDP:tubulin protofilaments curve outwards [105]. Depolymerization products include tight curls and rings [25]. Similarly, GDP:tubulin dimers bound to depolymerizing agents in solution have been shown to have a kinked conformation [106].

Dimers inside microtubules, however, are straight [36], and GMPCPP dimers in ribbon polymers show only a small curvature [103]. In addition, sheet structures observed at fast growing microtubule ends show only gentle curvature [107], and GMPCPP microtubules forced into depolymerization by cold temperatures or Ca^{2+} yield large spirals of protofilaments [25].

It appears, therefore, that the straighter conformation is related to a preference for microtubule assembly, while the curved conformation induces depolymerization. Some uncertainty remains on whether the straightening of the dimer is mainly driven by the binding of GTP [108] or by the lateral contacts made by the GTP:tubulin dimer in the microtubule lattice [109, 110]. It is however generally accepted that the energy released in GTP hydrolysis is stored as mechanical strain in the microtubule lattice to be freed during depolymerization [100].

Early studies suspected the nucleotide to affect the lateral interactions between protofilaments [111, 112]. This hypothesis has been difficult to test based on structural data because the structures for which crystallography studies were possible, such as zinc-induced sheets [37], have different lateral contacts than microtubules [36]. In addition, the domains now thought to be the key players in the lateral interactions are flexible loops which tend to be difficult to resolve in crystallography studies. After various iterations based on docking the x-ray crystallography data obtained from zinc-induced

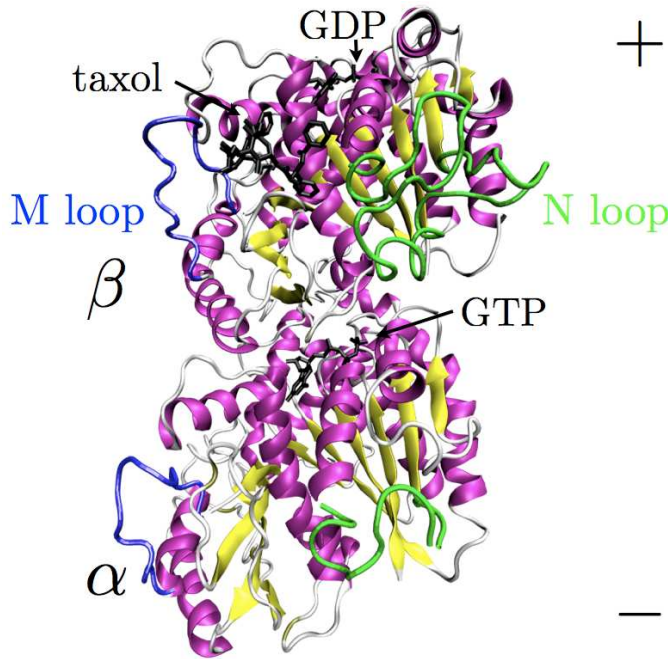


Figure 4.19: Molecular representation of the tubulin dimer, viewed from the inside of the microtubule with protofilaments aligned vertically. The regions thought to be involved in lateral interactions between protofilaments are highlighted: the M loop (H1-S2, residues 24-64) and N loop (S7-H9, residues 274-287) [113]. Both regions are flexible and relatively unstructured. This figure is based on PDB ID 1jff [114] and was partially created using VMD [2].

sheets [37] into density maps obtained from electron microscopy, the current understanding is that the lateral interactions between protofilaments are dominated by the so-called M loop and N loop [113]. Fig. 4.19 shows a schematic of the tubulin dimer that highlights these loops.

Some information has come from a recent AFM study comparing the indentation of taxol microtubules and GMPCPP microtubules [115]. The authors find a two-fold increase in the effective force constant in GMPCPP microtubules compared to taxol microtubules, a much smaller effect than in the present study. It is however not easily possible to deduce from this effective force constant the underlying effects on the microtubule lattice. The AFM tip used in the study had a nominal tip radius of 10 nm, very much comparable in size to the microtubule itself. The resulting indentation is therefore likely a result of the combined effects of protofilament number, local protofilaments bending and some displacement between neighbouring protofilaments in the radial direction. As, like in previous AFM experiments [116], the microtubule is supported by a substrate along the entire length, shear between neighbouring protofilaments is not expected. The mode of deformation found to be most affected by nucleotide state in the present study was hence not probed by their assay.

The present study therefore for the first time presents evidence of severe differences in the lateral interactions between protofilaments in the two different nucleotide states. While it is important to point out that the strength

of shear coupling does not directly translate into the lateral attraction between neighbouring dimers, it seems unlikely that a conformational change that so severely affects one, does not affect the other.

What consequences would an increased shear coupling between GTP protofilaments have for microtubule assembly? Such a tight coupling might lock dimers into a specific geometry at the growing end of a microtubule. The fact that GMPCPP microtubules almost exclusively contain exactly 14 protofilaments suggests that tighter coupling does indeed lead to better control of microtubule architecture. While GMPCPP:tubulin is generally fully accepted as a GTP:tubulin analogue, there are some differences in polymerization behaviour. The fact that GMPCPP:tubulin not only leads to a more restricted protofilament architecture but is also much more prone to nucleating new microtubules than GTP:tubulin must then be a result of the hydrolysis of GTP and may allow for conclusions with respect to its timing. It may be that a cap of GTP units at the growing microtubule end is not sufficient to restrict the relative positioning of protofilaments, or that GTP hydrolysis actually happens earlier in microtubule assembly than expected. An intermediate state such as the hypothesized GDP-Pi state [31] may then be factor governing the arrangement of protofilaments.

Taxol does not affect lateral interactions between protofilaments

Given that at least within the shear-dominated, length-dependent stiffness regime, taxol/GDP microtubules behave like taxol-free microtubules that have predominantly GDP bound, it follows that the shear interactions between neighbouring protofilaments are unaffected by taxol. This result conflicts with the notion that the M loop, thought to be a major factor in the lateral interactions between dimers, is stabilized by taxol [113], but is in agreement with several findings from a range of sources.

An X-ray diffraction study of osmotically buckled microtubules [117] showed that the critical pressure for buckling was independent of taxol concentration and concluded that taxol does not affect the lateral contacts between protofilaments probed in this study. Mitra & Sept [118] performed computational studies on arrays of tubulin dimers with and without bound taxol and concluded that taxol mainly affects the rigidity of contacts within protofilaments. This finding is backed up by a recent AFM study showing that straight protofilaments are formed in the presence of taxol, while GDP protofilaments form rings [101].

The present data do not contradict the notion that taxol has an effect on the longitudinal contacts within protofilaments. For microtubules with a mixed nucleotide content, the plateaus for l_p^0 and l_p^∞ are not covered in the

present study, and any change in κ_f would only lead to a linear offset in the length-dependent regime. A small offset is unlikely to be noticeable. For the GMPCPP microtubules with added taxol, however, a small increase in l_p^∞ was observed, suggested that taxol might stiffen protofilaments slightly. But it is unclear whether taxol would have similar effects on a GMPCPP lattice as on a GDP lattice.

4.1.5 Mechanical and architectural heterogeneity

Mechanical heterogeneity in the microtubule population

The measurements on taxol microtubules as well as those with a low GMPCPP content display a large scatter. Measurement error or flaws in the analysis can be ruled out as the cause because of two observations. Firstly, the drag coefficients computed from the stiffnesses do not retain this scatter but are smooth. Secondly, the stiffness estimates for GMPCPP microtubules, which are considerably higher and therefore present more of a challenge for measurements, do not display this much scatter. It may be argued that on a linear scale the scatter is similar, but because parameters enter the equations for stiffness estimates multiplicatively, it makes more sense to look at the scatter relative to the absolute value. Relative errors of a given magnitude appear constant throughout the range of a logarithmic plot. The data therefore show clear evidence that there is true heterogeneity in mechanical properties of these microtubule populations.

Known heterogeneities in microtubule architecture *in vitro*

It is tempting to link this heterogeneity to the variations in microtubule architecture observed in EM and x-ray diffraction studies of microtubules polymerized *in vitro* [43, 119, 44, 46, 120]. Unfortunately, there is considerable disagreement in the literature over the distribution of protofilament numbers for taxol microtubules. While some studies claim that the addition of taxol quickly induces even preassembled microtubules to reduce their protofilament number to 12 [119, 120], others find that the addition of taxol largely preserves the protofilament number assumed during taxol-free assembly [46]. Arnal et al. [46] find a largely even mix of 13, 14 and 15 protofilaments under typical assembly conditions, while others [43, 121, 10] find a distribution that is strongly peaked at 14 protofilaments and has only smaller percentages with 13, 15, and 16 protofilaments. Chrétien et al. [44] showed that the magnesium concentration present at polymerization can have an effect on the relative frequencies.

By contrast, in the case of GMPCPP, Hyman et al. [47] found that $\sim 95\%$ of the microtubules have 14 protofilaments. The greater architectural heterogeneity found for taxol microtubules may be the reason for the large scatter in persistence lengths obtained specifically for this condition.

Relation of structural and mechanical variations

As has been argued before [10], if microtubules are modeled as homogeneous elastic tubes as in Eq. 1.4, the resulting difference in stiffness between a 13 and a 14 protofilament microtubule should only be on the order of $\sim 20\%$. The observed scatter however is much larger, emphasizing again that this simple mechanical model is insufficient.

In the Wormlike Bundle Model [5, 6], however, not just the number of protofilaments, but also the presence of supertwist will have an effect on the resulting stiffness. While the scaling with protofilament number is almost linear, Heussinger et al. [6] predict that the presence of supertwist should make the filament softer, but to a degree that is strongly dependent on the other parameters such as the length of the filament and the strength of the lateral coupling. The underlying reasoning is that the rotation of each protofilament from one side of the filament to the other allows the protofilaments to more evenly accommodate the shear displacements between each other. Only microtubules with no supertwist are expected to purely follow the WLB effective bending stiffness given in Eq. 4.4 and Fig. 4.5.

How can this prediction of the effects of pretwist be reconciled with the likely distribution of protofilament architectures for these measurements?

For a 14 protofilament architecture, as found in GMPCPP microtubules, the lattice rotation model [43] predicts a supertwist pitch of $5.6\ \mu\text{m}$ [45]. If the subunit spacing along protofilaments is somewhat increased [47], this pitch is probably a little larger. It stands to reason that this supertwist should only have a softening effect on the microtubule, if the length scale of the pitch is at least as short as the length scale where, if the microtubule did not have supertwist, shear effects would begin to be relevant, that is the length scale L_x in Eq. 4.5. If, however, L_x is very short, for instance because of a very strong lateral coupling between protofilaments, then the supertwist of GMPCPP microtubules will not be relevant for their mechanical properties. The implication would be that the measured stiffness values already correspond to the long length stiffness plateau, and no length dependence should be apparent in the data. This scenario is consistent with the results presented here.

For taxol microtubules, the situation is more complicated. Because of the discrepancy in literature reports concerning the likely protofilament number

distribution, different scenarios will be considered individually.

Suppose all microtubules had 12 protofilaments as in the studies by Andreu et al. [119]. The expected supertwist pitch should be roughly $4\text{ }\mu\text{m}$ (compare Table 1.1). Given that taxol microtubules with a length of $4\text{ }\mu\text{m}$ and shorter seem to have reached the putative short-length stiffness plateau of $l_p^0 \sim 700\text{ }\mu\text{m}$, the supertwist should cause the longer microtubules to have a similarly low stiffness. That this is however not the case. In addition, if all microtubules had the same number of protofilaments, the source of the scatter would be mysterious.

Suppose then that the taxol microtubule protofilament distribution is similar to those found by Chretien et al. [43], or Arnal et al. [46]. Any 13-protofilament microtubules should have straight protofilaments and therefore display a bending stiffness that scales with length according to Eq. 4.4 and Fig. 4.5. Because for any other similar number of protofilaments, the expected supertwist (Table 1.1) is on the order of a few μm , that is shorter than the putative L_b , the same argument as for 12 protofilament microtubules apply, and these microtubules should display a low and only weakly length-dependent stiffness. The one taxol microtubule in Fig. 4.23 with a low first mode stiffness estimate and a slightly higher second mode stiffness estimate might then be one of this class. While these kinds of microtubules would probably create a noisy plateau of relatively low stiffness, those with 13 protofilaments should follow the length dependence of Eq. 4.4 without much scatter. This appears to not be the case: The region with the clearest length dependence in the middle of Fig. 4.1 still exhibits a lot of scatter.

The reason for this discrepancy likely lies in lattice defects. Chrétien et al. [44] have shown that transitions in the number of protofilaments can occur even along a single microtubule, and that such transitions constitute the norm rather than an exception for microtubules formed *in vitro*. The transitions frequencies between different architectures are surprisingly high and range from hundreds of nanometers to tens of microns. Given that such transitions would likely disrupt the smooth shear between protofilaments, one would expect lattice defects to have a stiffening effect on microtubules within the length-dependent regime. On the other hand, it may be argued that defects produce a weak spot in the lattice that might bend more easily. While the question cannot be answered on the basis of current models, it might be possible to probe it experimentally by manipulating the frequency of defects and testing the resulting change in the mechanics.

4.1.6 Consistency checks

The biharmonic modes are the correct eigenmodes

In Section 1.3.2 it was mentioned that there may be reason to suspect that the biharmonic modes are not the true eigenmodes, and that pure harmonic modes would be a more appropriate set of basis functions. The present data allow to test this claim using measurements of microtubules with two beads attached at different points along the contour.

While both models lead to the same expression

$$\sigma^2(y(s)) = \frac{s^3}{3l_p} \quad (4.14)$$

for the total transverse position variance at any point s , the relative contributions of the different modes vary between the two models. Because the present measurements single out contributions from the first mode only, the resulting stiffness estimate depends on the set of basis functions chosen.

If two beads are attached at different positions s along one microtubule as in Fig. 4.20, the correct model should give consistent estimates for measurements from the two beads. Fig. 4.21 shows that while estimates from the harmonic modes are biased towards underestimating the stiffness from the measurement of the bead attached closer to the grafted end, the biharmonic modes yield consistent estimates.

Results for higher modes

Eq. 4.4 predicts that the stiffness is a function not just of length, but also of mode number because the expression scales with L/q_n . Higher modes are therefore expected to display a lower stiffness, analogous to short microtubules. While in most cases, this assay only resolves contributions from the first mode, in rare cases contributions from the second mode can be resolved, allowing for the theory's prediction to be tested.

This situation arises when long microtubules are measured that have a bead attached not too close to the free end. While the first mode dominates the mode amplitudes at the free end, contributions from higher modes increase towards the grafted end. Although only data from a single point along the microtubule contour are gathered, a statistical separation of mode contributions is possible on the basis of the dynamics. This approach relies on a combination of a high frame rate and large amounts of data to be able to capture and adequately sample dynamics on the vastly different time scales of the first and second mode. Fig. 4.22 shows an example.

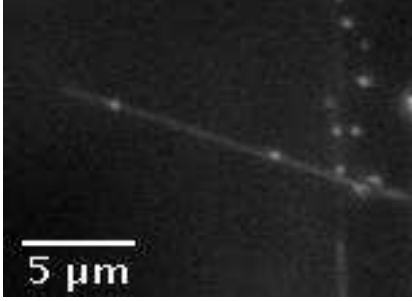


Figure 4.20: Example microtubule with two beads attached at different positions along its contour.

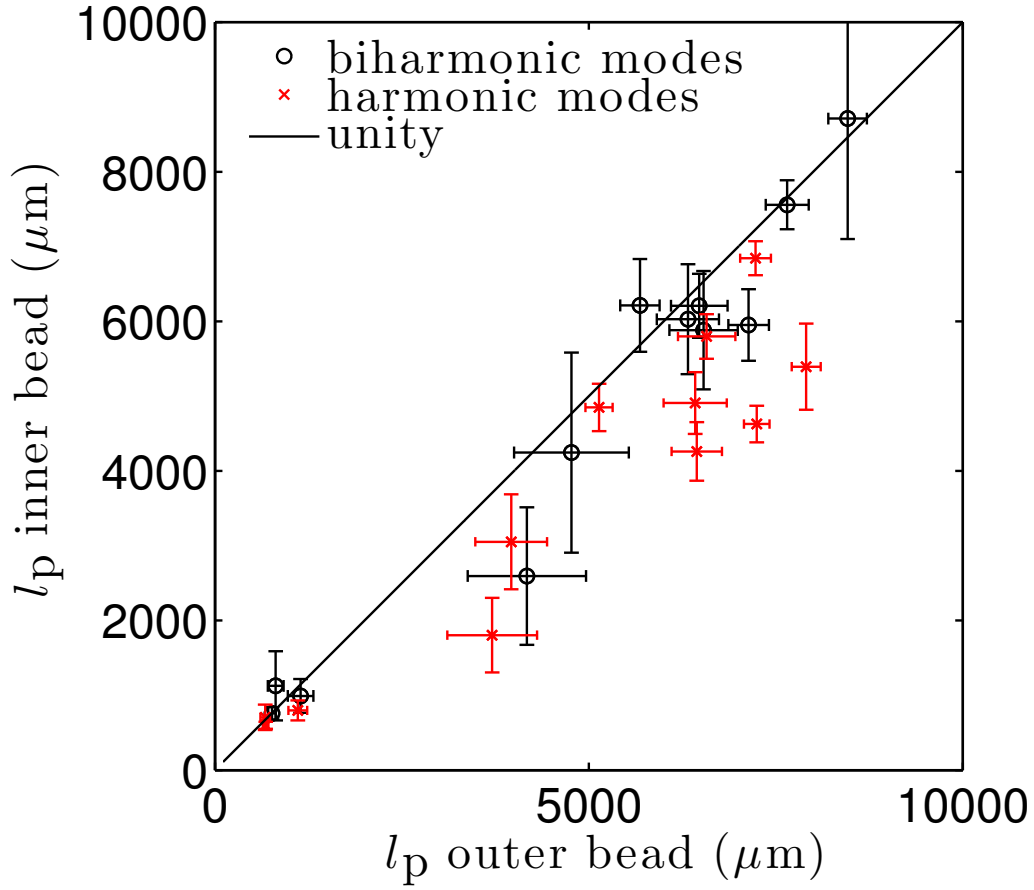


Figure 4.21: Persistence length estimates from different eigenmode models. Microtubules of a variety of chemical conditions with two beads attached at different positions along their contour are shown. For both models, the estimates from measurements of the bead closer to the grafted end are plotted against those for the bead closer to the free end. Consistency demands that the data follow unity.

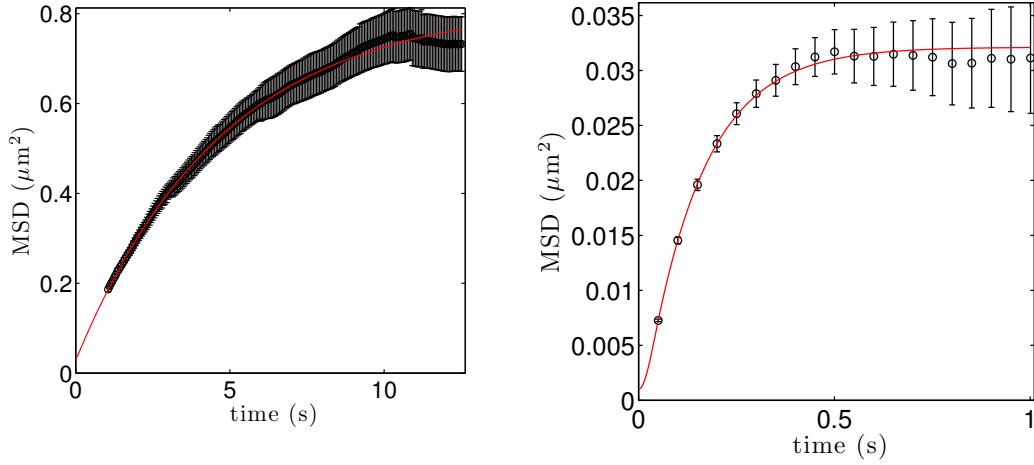


Figure 4.22: First (left) and 2nd (right) mode MSD fits for a taxol microtubule with a length of $23.1 \pm 0.1 \mu\text{m}$. 30,000 frames were recorded at a rate of 19.98 Hz with an exposure time of 50 ms. The first mode fit neglects the first 30 data points of the full MSD because these are affected by the dynamics of the second mode, and yields $\tau_1 = 4.7 \pm 0.3 \text{ s}$ and $l_p = 2450 \pm 75 \mu\text{m}$. The data for the second mode MSD are computed by subtracting the result of the first mode fit from the full MSD. The dynamics of the second mode are remarkably well retrieved. The fit yields $\tau_2 = 144 \pm 9 \text{ ms}$ and $l_p = 1530 \pm 150 \mu\text{m}$.

For 6 microtubules of different chemical conditions it was possible to extract the MSD of the second mode. Fig. 4.23 shows the stiffness data from Fig. 4.15 overlaid with the results for these microtubules. The x-axis has been scaled in terms of L/q_n so that results from different modes can be combined. The first two mode numbers are $q_1 = 1.875$ and $q_2 = 4.694$.

It can be seen that the second mode generally follows the trends observed for first mode stiffnesses of shorter microtubules. For taxol microtubules as well as microtubules with only a low content of GMPCPP, the second mode generally appears to be softer than the first, matching the prediction of the Wormlike Bundle Model. In contrast, microtubules with a high content of GMPCPP show no such decrease. The apparent slight increase for the second mode compared to the first for these two data points may not be real - measurements in this regime are challenging because of the time and length scales involved. In addition, the error bars represent only one standard deviation and hence only a confidence of 68%.

The data also confirm the existence of inhomogeneities within the population of taxol microtubules. Of the three taxol microtubules measured in this way, two show a sharp drop in mode stiffness from the first to the second mode, while the other one has a slightly lower estimate for the first than for the second mode. Interestingly, while the second mode data point for this

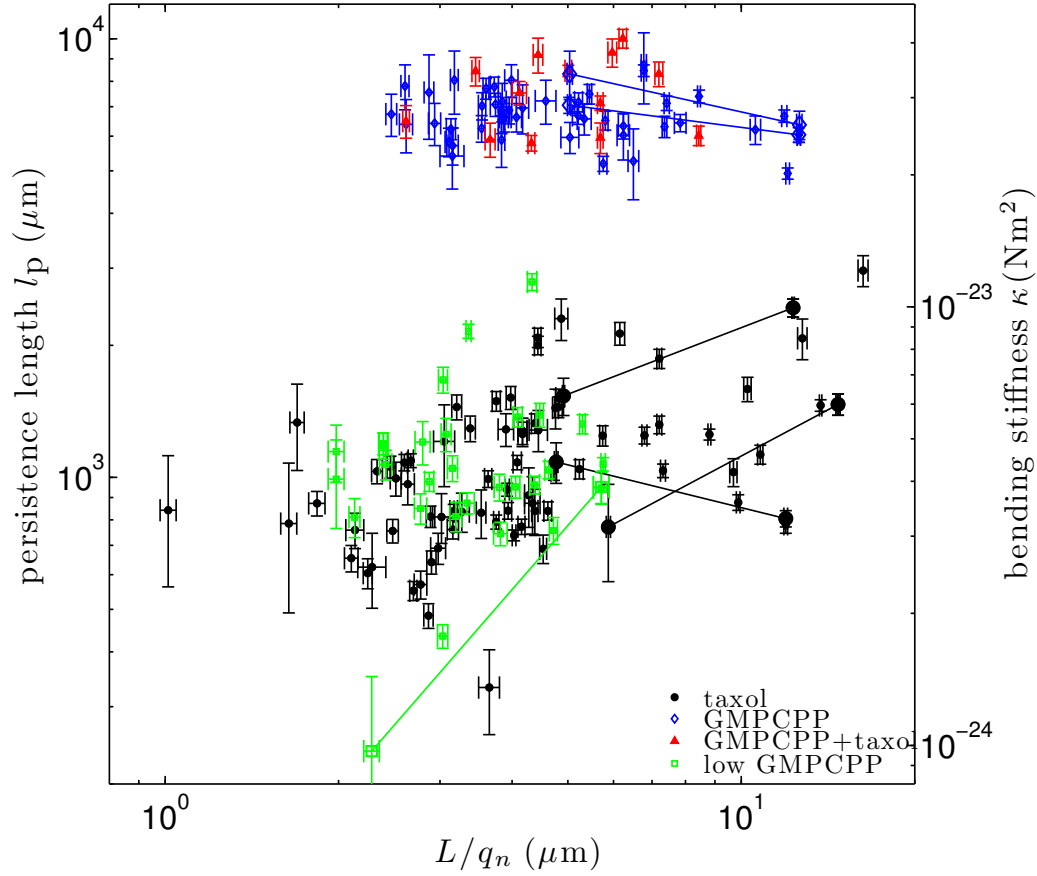


Figure 4.23: Stiffness as a function of wavelength. The small symbols represent the same stiffness data as in Fig. 4.15, while the overlaid large symbols are data from microtubules where both the first and the second mode contribution could be resolved. The second mode stiffness is always the left one in any one pair of large symbols connected by a line.

microtubule lies in the typical range for first mode estimates of shorter microtubules, the estimate for the first mode is uncharacteristically low for its length. At a length of $22.4 \pm 0.2 \mu\text{m}$, this microtubule has the lowest first mode stiffness measured among those longer than $10 \mu\text{m}$. It stands to reason, then, that it is the first mode, and not the second mode stiffness estimate that constitutes an outlier.

As Fig. 4.16 showed that all types of microtubules are affected by internal friction scaling with $(q_n/L)^4$, one might expect that second mode contributions show a similar rise. It is not very revealing to plot drag estimates from the first and second mode on the same scale because hydrodynamic friction scales with only L and internal friction is expected to scale with q_n/L . Fig. 4.24 hence shows results from the two modes side-by-side. While for

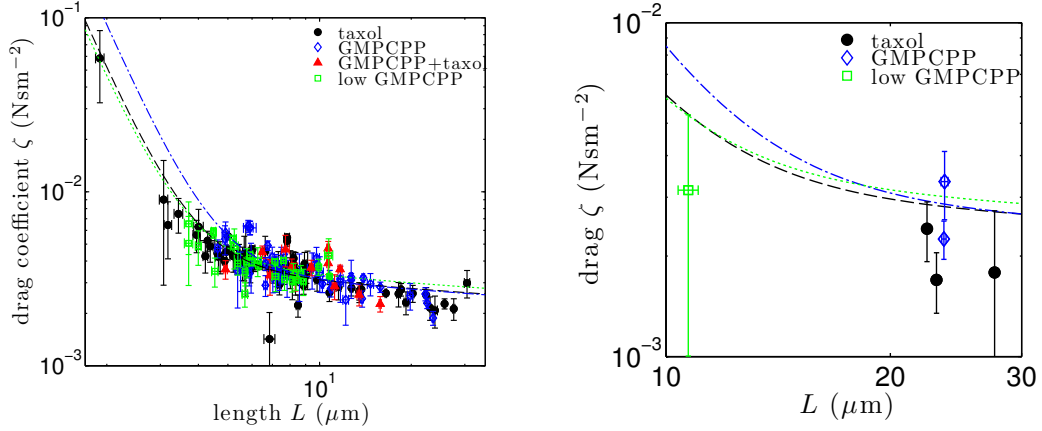


Figure 4.24: First (left) and second (right) mode drag coefficients. The left figure is a replica of Fig. 4.16 and is shown for reference. The lines are fits to Eq. 4.10. In the right figure, the second mode relaxation times are shown the first mode fit results, with the internal friction component of the fit rescaled by $(q_2/q_1)^4 \approx 39$.

the first mode, the contributions from internal friction become larger than those from hydrodynamic friction at $3.8 \mu\text{m}$, this length regime is expected to be shifted by a factor of q_2/q_1 to $\sim 10 \mu\text{m}$ for the second mode. The data for second mode contributions however were obtained only for microtubules longer than $10 \mu\text{m}$. They therefore do not provide any additional evidence on the existence of internal friction, although they are consistent with the fit obtained for first mode drag coefficients.

Interestingly, the second mode data do not scatter around the line predicted from the first mode data, but are mostly smaller, though within error. This systematic pattern raises the possibility that the procedure used here to separate first and second mode contributions introduces a bias.

4.2 Free microtubules

4.2.1 Intrinsic shapes

It has frequently been noted that microtubules formed in vitro often are not straight, but show pronounced intrinsic curvature [10]. Strangely, no thorough investigation seems to have addressed the cause of this observation or its connection to the underlying microtubule structure.

This intrinsic curvature can be described in terms of the mean mode amplitudes $\langle a_n \rangle$. Fig. 4.25 shows a schematic of such a parametrization of the intrinsic shape in 2D. Bending fluctuations occur in both transverse directions about the mean of the mode amplitudes. Only the horizontal component of the amplitudes is observed in this assay, but rotations can still be distinguished from bending fluctuations on the basis of correlations between the amplitudes of different modes, as shown in Fig. 4.26.

Rotating filaments are discarded, and only filaments whose mode amplitudes show no evidence of rotation are retained. It is important to note though that even in cases where rotations are small and insignificant for low modes, they may yet affect higher modes more strongly. In particular, if a

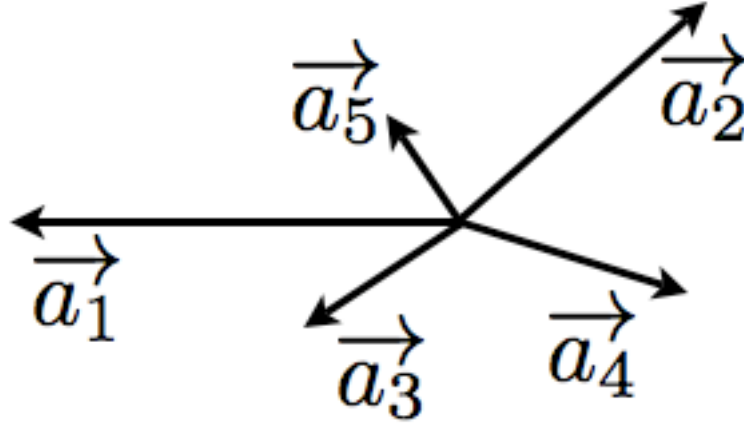


Figure 4.25: Schematic of mean mode amplitudes in 2D. The main axis of the filament is perpendicular to the plane, and the mean shape is described in terms of the mode amplitudes $\langle \vec{a}_n \rangle$. Because there are two transverse directions, the \vec{a}_n are vectors with two components. In the present assay, only the horizontal component is observed. It is expected that microtubules with a large enough intrinsic curvature to prevent them from rotating will orient such that the largest mean mode amplitude is aligned roughly horizontally in the thin sample chamber.

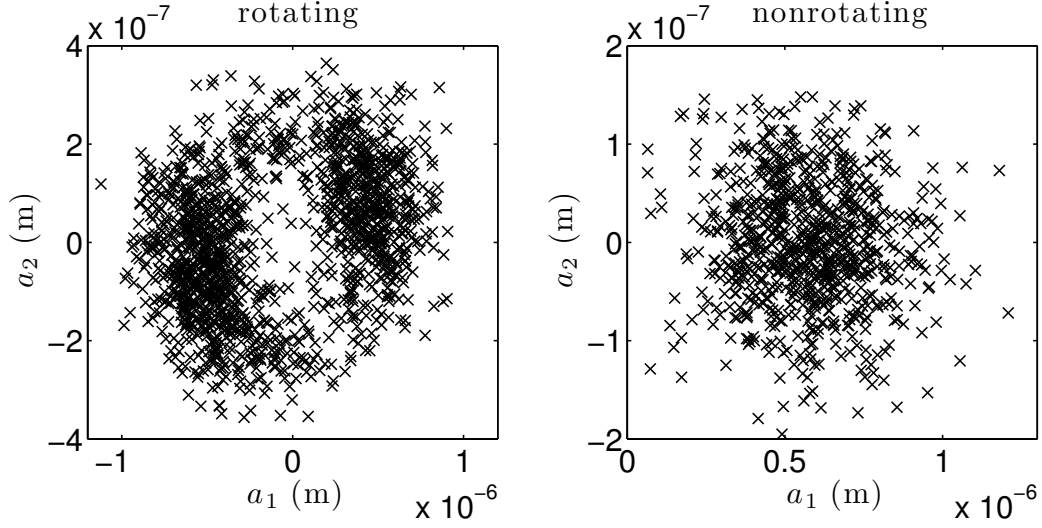


Figure 4.26: Correlations between the observed horizontal amplitudes of different modes reveal rotations of the filament. When rotations dominate the mode amplitudes, they follow an elliptical pattern around the origin (left). In the case shown here, the angle between the intrinsic mode amplitudes \vec{a}_1 and \vec{a}_2 must be close to $\pi/2$ as one appears maximal when the other is close to zero. Scatter around the pattern is due to bending fluctuations. Only when the filament is not rotating, or when the rotational contributions to the observed fluctuations are small for the mode in question, do the amplitudes of different modes fluctuate independently (right) around a mean given by their intrinsic curvature.

mode has a high intrinsic curvature in the direction along the optical axis, a small rotation can significantly increase its observed amplitude fluctuations.

As the source of intrinsic curvature is unknown, it is not a priori clear what patterns its amplitudes should follow. Fig. 4.27 shows that the spectrum of these intrinsic shapes is surprisingly similar to those expected from thermal bending fluctuations. For thermal fluctuations,

$$\sigma^2(a_n) = \langle a_n^2 \rangle - \langle a_n \rangle^2 = \frac{L^3}{q^4 l_p}, \quad (4.15)$$

hence

$$\sigma^2(a_n)L = \left(\frac{L}{q}\right)^4 l_p^{-1} \quad (4.16)$$

It is important to note, however, that the data presented here are not representative of the microtubule population as a whole. In order to avoid ambiguity in the attribution of mode amplitudes to filament orientation or bending, only microtubules were chosen for analysis that had an intrinsic curvature large enough to prevent them from rotating in the sample chamber

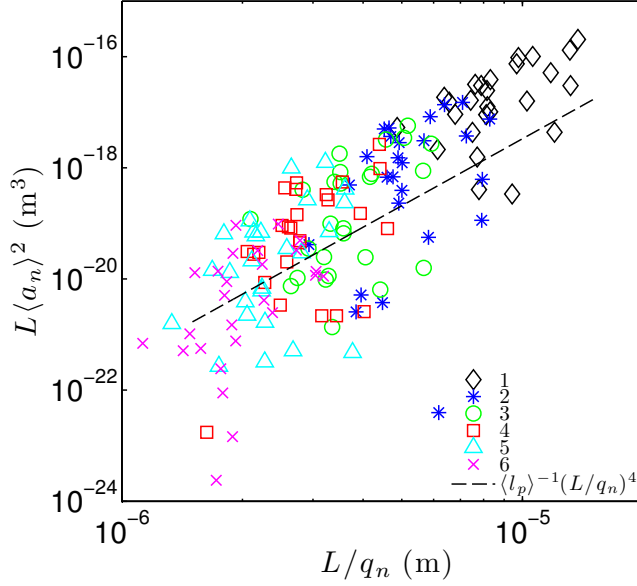


Figure 4.27: Intrinsic microtubule shape spectrum. Intrinsic shape amplitude data for modes 1-6 is shown plotted against wavelength. The dashed line shows the spectrum that would be expected from thermal bending fluctuations for a persistence length $l_p = 3$ mm which is about the average of the measured microtubules. Intrinsic shapes show a mode spectrum with a similar power law dependence.

of thickness $\sim 1 - 2 \mu\text{m}$. Each sample only contained few such microtubules since the majority of filaments were close to straight. Curiously, previous studies using similarly thin sample chambers do not report the need for this selection [10, 66, 90].

In order for the filament to not be able to rotate, at least one mode needs to have a mean amplitude larger than $\sim 1 \mu\text{m}$. In addition, however, the filament also needs to be stiff enough such that the thermal fluctuations are small compared to this value so as to prevent the filament from flipping during instances where its shape becomes close to straight. It is therefore expected for many of the mean amplitude values in Fig. 4.27 to lie above the line representing the expectation for thermal fluctuations. The same will not be true for the whole population. It is reasonable to expect that the equivalent plot for the whole microtubule population would fill in more data points below the thermal spectrum, but it seems unlikely that the pronounced power law dependence on wavelength would disappear.

Dye et al. [67] as well as Venier et al. [68] describe taxol microtubules as having a “wavy” shape. Venier et al. show evidence of a characteristic wavelength of $\sim 7 \mu\text{m}$ and suggest helicity as a cause. Such a characteristic pitch should produce a peak roughly in the middle of the range of the plot in Fig. 4.27, but the data show no evidence of it. In addition, the amplitudes of more than $0.5 \mu\text{m}$ indicated by Venier et al. are large enough that a 3D helical shape would become visually apparent due to periodic defocus along the microtubule contour. In this study, such an effect was never observed.

The close-to-thermal spectrum of the intrinsic shapes may yield a hint

towards the mechanism underlying their formation. It suggests that bending energy is a limiting factor in the formation of these shapes, but does not clarify whether the bends are formed during the polymerization process, or later, for instance by freezing of thermal undulations by some unknown mechanism of structural plasticity. Either pathway seems plausible since taxol microtubules have been reported to have very dynamic structures. Diaz et al. [120] present evidence that the addition of taxoids can change the number of protofilaments on a subminute timescale, that is too fast for depolymerization/polymerization cycles. Shida et al. [122] show that the tubulin acetyltransferase α TAT1 with a molecular weight of over 30 kDa unrestrictedly binds to a site inside the microtubule lumen, suggesting that the microtubule lattice is somewhat malleable and may be able to open transiently.

4.2.2 Stiffness estimates

Stiffness estimates were obtained from freely fluctuating microtubules with an intrinsic curvature large enough to prevent them from rotating in the sample chamber.

Stiffness estimates show extreme scatter

Because stiffness scales with the wave length in the Wormlike Bundle Model, one would expect results obtained from different modes or boundary conditions to coincide if plotted against L/q_n . Doing so would then present an elegant way of combining the data gained from the grafted and free microtubule experiments.

Instead, Fig. 4.28 shows that the results obtained for free microtubules do not collapse onto the data obtained for grafted microtubules. Different modes of the same microtubule yield reasonably close results, validating the data analysis procedures. Between different microtubules, however, there is a vast scatter. Only a small part of the data overlaps well with the results from grafted microtubules, most scatter over a vast range. While many microtubules display a trend of higher modes having lower stiffness values, there is no clear overall pattern showing wavelength dependence in the data.

Stiffness estimates correlate with sample, but not batch

A reasonable expectation would be that the spread in results is correlated with polymerization conditions. Microtubules that were part of the same polymerization batch should then show similar mechanical behaviour. Yet Fig. 4.29 A demonstrates that this is not the case. Panel B of the same

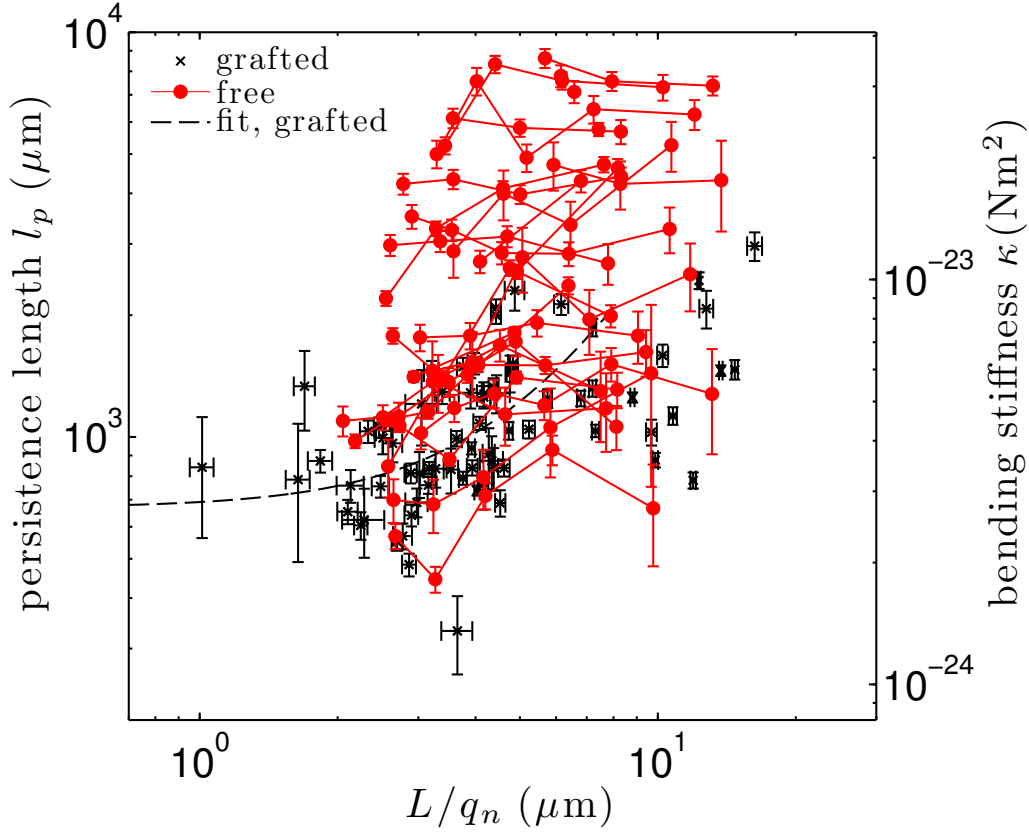


Figure 4.28: Stiffness estimates from free and grafted taxol microtubules. Data for grafted taxol microtubules are as in Fig. 4.1, but the x-axis has been rescaled by mode number so that results obtained for different modes and boundary conditions can be combined. For free microtubules, data points from different modes of the same microtubule are linked by lines.

figure however shows that results for microtubules within the same sample show similar stiffnesses.

The fact that stiffness estimates show a large scatter, but correlate reasonably well within each sample allows one to narrow down the potential sources of scatter. The microtubule preparation and buffer used for these experiments was identical to that used in the experiments on grafted microtubules. While those experiments showed some scatter in stiffness estimates, the drag coefficients were smooth, and no correlation was observed between results for microtubules in the same sample.

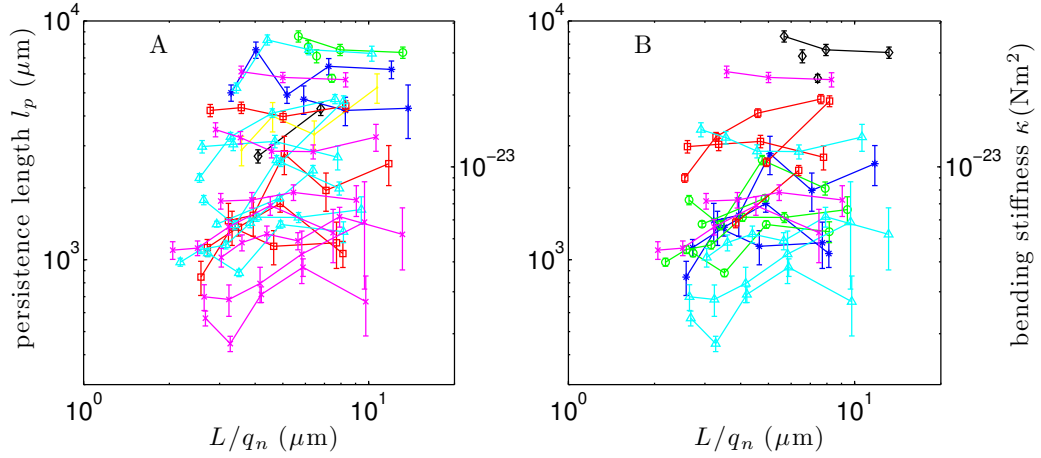


Figure 4.29: Stiffness estimate obtained from free taxol microtubules, grouped by polymerization batch (A) and by sample (B). In Panel A, the batches coloured dark blue and yellow made use of casein as a shielding agent, all other data used PEG. Panel B includes only data from samples with at least three microtubule measurements. These include only data obtained with PEG as the shielding agent.

Blocking agents may be buckling microtubules

One difference between the two assays is the use of the blocking agents PEG and casein to shield glass surfaces. It is possible that due to incomplete rinsing of coverslips, some unbound PEG remained on the coverslips and entered the microtubule solution. An indicator that this may have been the case is the fact that microtubules were observed to bundle upon touching, pointing towards the presence of depletion forces which can be caused by large macromolecules or colloids in solution [117].

Intriguingly, similar behaviour was also observed in the presence of beta casein. This may be because beta casein can form micelles with a size of ~ 8 nm [123] which could potentially act in a similar manner as PEG.

While PEG was specifically chosen because of its inertness in relation to biological molecules, it has been shown that high molecular weight PEG in solution can exert osmotic pressure on microtubules. Needleman et al. [117] used PEG with a molecular weight of 20,000 Da to assemble microtubules in arrays using depletion forces, and to buckle them into a elliptical cross sections. Using x-ray diffraction, they showed that while concentrations around 1 % buckled microtubules osmotically, at concentrations higher than ~ 7.5 % the cross section was restored to circular, indicating that the PEG molecules were forced into the microtubule lumen. The authors established a critical pressure of 600 Pa for the buckling of microtubules.

The PEG molecules used in the present study had a lower molecular

weight of 5,000 Da. For PEG-20,000 the radius of gyration was estimated by Needleman et al. to be around 7 nm which is similar to the inner radius of the microtubule of ~ 8 nm. PEG-5000 can be estimated to have a radius of gyration around 3 nm [124]. While this value is roughly a factor of 2 smaller than the radius of the microtubule lumen, at least at low concentrations one would expect that entropic effects decrease the concentration inside the lumen compared to the outside. Given that 5 % PEG-4000 has been reported to already create an osmotic pressure of 10^5 Pa [125], it is plausible that a small amount of PEG-5000 in solution might create an osmotic pressure larger than the critical value of 600 Pa established by Needleman et al. [117].

The rinsing of the coverslips after incubation with PEG might leave variable amounts of free PEG behind, and the volume of the microtubule solution is not precisely controlled either because for sub- μ l volumes pipetted with cut pipet tips, a large fraction of the solution remains in the pipet tip. Different samples may hence contain different concentrations of PEG and thereby subject the contained microtubules to different amounts of osmotic deformation. It is reasonable to expect a drastic change in mechanical properties if the structure is put under massive stress.

Because only three microtubules were measured in the presence of casein rather than PEG as a shielding agent, it is difficult to say whether casein may have similar effects. Given that the size of casein micelles is similar to the inner diameter of microtubules and that beta casein micelles have been reported to exert depletion forces previously [126], it seems reasonable to expect that they would be capable of exerting osmotic pressure on microtubules, too.

It is curious that the few data points obtained for this condition are all quite high compared to the values obtained for grafted boundary conditions. Casein in solution was also used as a shielding agent in the studies by Gittes et al. [10] and Mickey et al. [66], and these two studies also obtained similarly high values for the stiffness of taxol microtubules. It is hence plausible that both PEG and casein might affect the mechanics of microtubules by exerting osmotic pressure.

Buckling response confirms relevance of interprotofilament bonds

It seems reasonable to assume that the contacts between protofilaments will be most affected by osmotic buckling of the microtubule cross section, as argued by Needleman et al. [117]. The fact that such a strong mechanical response to buckling is seen then confirms that interprotofilament contacts are the key mechanical elements regulating the stiffness response for microtubules in this wavelength regime.

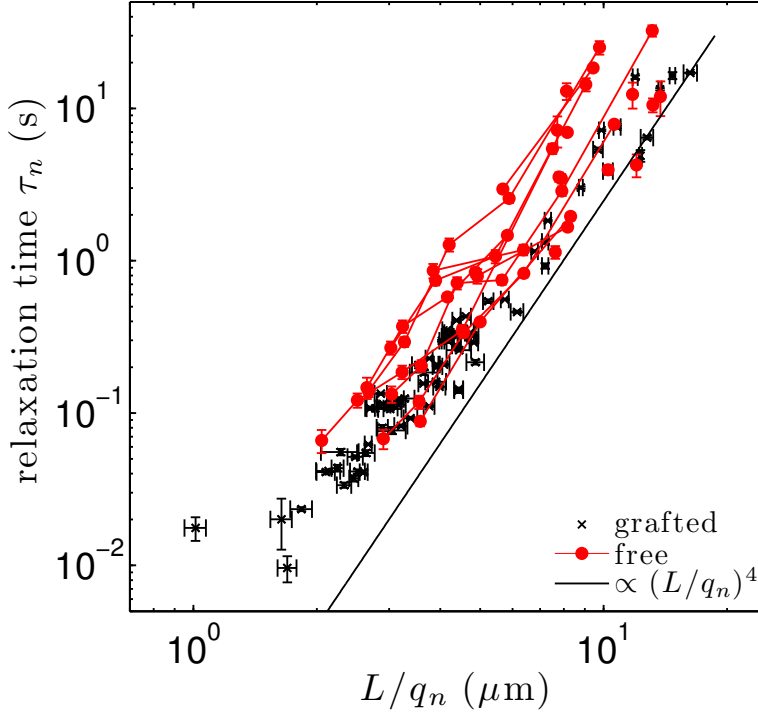


Figure 4.30: Relaxation times for free microtubules in comparison to those for grafted microtubules. The data for grafted taxol microtubules are as in Fig. 4.7. Data from different modes of the same microtubule are connected by lines.

4.2.3 Relaxation times

Since many of the stiffness values obtained for free microtubules are larger than the values found for grafted microtubules, one might expect shorter relaxation times as well. Fig. 4.30 shows that this is not the case. Relaxation times for free microtubules are similar to or larger than the values obtained for grafted microtubules, pointing at the presence of stronger drag forces. Similar to grafted microtubules, the values for free microtubules show a steeper scaling for long length scales and shallower slopes for shorter length scales. The scatter is however much larger.

Fig. 4.31 shows the same data coloured by sample as in Fig. 4.29 B. Again, data from the same sample behave similarly, though the correlation is not as clear as for the stiffness values in Fig. 4.29 B.

4.2.4 Drag coefficients

The hydrodynamic drag for the microtubules in these experiments is expected to be higher than for the previously discussed grafted ones because of the vicinity of the coverslips leading to hydrodynamic coupling. The hydrodynamic drag per unit length acting on a long filament moving between

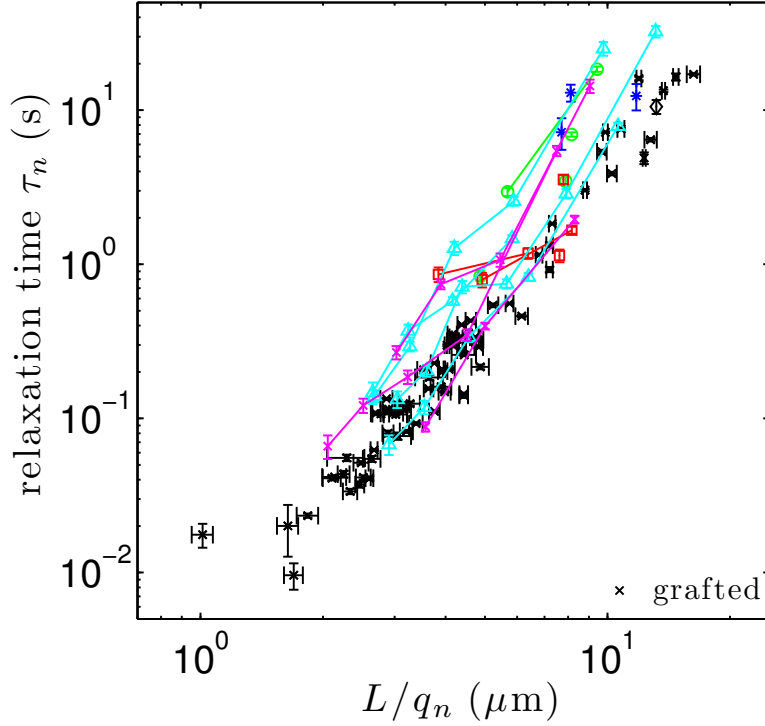


Figure 4.31: Relaxation times for free microtubules in comparison to those for grafted microtubules. The data are as in Fig. 4.30, but the values for free microtubules are coloured by sample. Only samples with three or more measured microtubules are included.

and parallel to two surfaces can be estimated as [127, 91, 54]

$$\zeta_{\text{hydro}} = \frac{8\pi\eta}{\cosh^{-1}(2h/d)}, \quad (4.17)$$

where h is the distance between the cylinder and the surfaces and d is the cylinder's diameter.

Fig. 4.32 shows that the drag coefficients obtained here are indeed larger than the values found for grafted microtubules in Section 4.1.1. The values are not too dissimilar from the hydrodynamic estimate of Eq. 4.17, assuming $h = 0.5 \mu\text{m}$, and fall into a similar range as the fits found by Janson et al. [54] and Brangwynne et al. [90]. As predicted by Eq. 4.10, shorter wavelengths show a trend towards increased friction, confirming the presence of internal friction.

In contrast to the data obtained for grafted microtubules, however, the drag coefficients for free microtubules contain a lot of scatter. Some of this scatter is expected because the Eq. 4.17 depends on the thickness of the sample chamber. This value is not tightly controlled and may even vary between different positions within one sample. In addition, the distance a microtubule keeps from the coverslips may vary along its length because of intrinsic curvature, giving rise to more scatter.

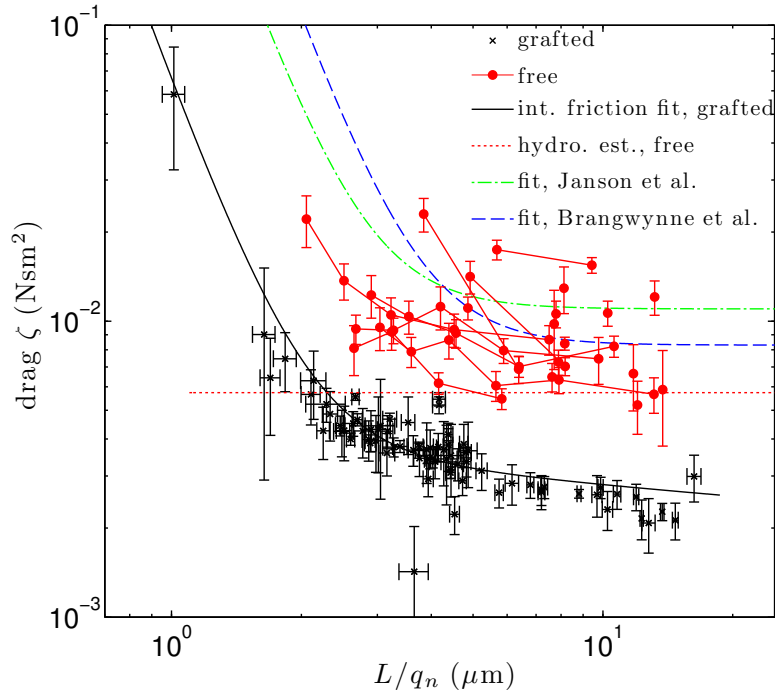


Figure 4.32: Drag coefficients for free microtubules in comparison to the data previously obtained for grafted microtubules. Data connected by lines correspond to different modes of the same microtubule. The red dotted line shows a hydrodynamic estimate according to Eq. 4.17 with $h = 0.5 \mu\text{m}$.

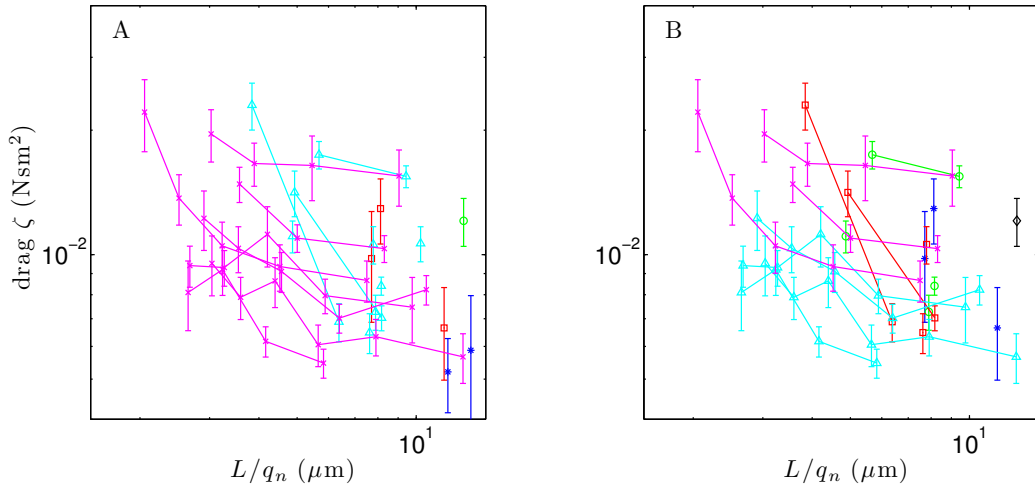


Figure 4.33: Drag estimates obtained from free taxol microtubules, grouped by polymerization batch (A) and by sample (B).

Fig. 4.33 shows that similar to stiffness estimates, drag coefficients also show some correlation with sample, but not with polymerization batch.

4.3 Comparison of the two approaches

Historically, the approach of measuring shape fluctuations of free microtubules has been the more prevalent and well executed one. Gittes et al. [10] presented a very thorough analysis that carefully considered most error sources, and later studies [66, 90] were modeled after it.

By comparison, most studies measuring microtubule stiffness from fluctuations of grafted microtubules used much less sophisticated methods and reasoning. Mickey et al. [66] rightfully list various oversights in other studies attempting to extract stiffness estimates from thermal fluctuations. Typical problems range from mathematical errors [68] over disregard of intrinsic shape [67] and improper hydrodynamic treatments [68] to position errors [67].

Early studies generally also suffered from a lack of sampling because in the absence of automated tracking, only a few dozen frames were analyzed per microtubule [10, 68, 128]. Strangely, many later studies stuck with this small number of samples [57, 129, 99] despite technical advances making automation more feasible. Janson et al. [54] were the first to automate shape tracking of microtubules, and Pampaloni et al. [59] were the first to harness single particle tracking techniques using attached fluorescent beads to extract thermal fluctuation-based stiffness estimates.

The present study is unique in that it allows a comparison of both techniques under high sampling. The method based on tracking fluorescent beads attached to grafted microtubules is validated by several observations: 1) Two beads attached at different positions on one microtubule yield the same result. 2) Repeat measurements yield the same result within error. 3) Remaining scatter can clearly be attributed to true mechanical heterogeneity because of the almost constant results obtained for GMPCPP microtubules as well as the consistent values always obtained for drag coefficients.

Using those measurements as a baseline, the measurements on free microtubules can be evaluated. In comparison, it becomes clear that the data obtained here for free microtubules may be an artefact of sample preparation. Brangwynne et al. [90] used an almost identical preparation to the present experiments using PEG shielding, and show results that scatter across the entire range that is not excluded by noise limitations. Gittes et al. [10] and Mickey et al. [66] used conditions very similar to those used for the present experiments employing casein shielding, and obtain similarly large values and large scatter as found here. It therefore seems plausible that the measurements obtained in those studies were suffering from similar artefacts.

The scatter remaining within one sample in the present study is comparable or slightly larger than observed for grafted microtubules where the mechanical heterogeneity was attributed to variations in microtubules ar-

chitecture. Because the measurements on free microtubules were selectively performed on microtubules with a large intrinsic curvature, one would expect them to show at least as much scatter as those obtained for grafted microtubules.

Table 4.3 compares the main features of each approach. As evidenced by the results of the present study, the approach based on measurements of grafted microtubules seems superior.

Table 4.3: Comparison of the advantages and disadvantages of the two techniques used in the present study.

shape tracking free MT	grafted MT with bead
+ easy sample preparation	– involved sample preparation
– possible artefacts from surface shielding	+ no shielding required
– limited to high intrinsic curvature microtubules	– limited by stochastic bead attachment
– variable hydrodynamic conditions	+ no hydrodynamic coupling
– $10^2 - 10^3$ frames feasible	+ 10^4 frames easily possible
– precision limited to tens of nm	+ precision of a few nm
+ higher modes easily accessible	– large difference in time scales between first and higher modes

Chapter 5

Conclusions and outlook

5.1 Summary

The present study used two types of thermal fluctuation measurements to extract mechanical parameters of microtubules. For grafted microtubules, high precision position information was extracted for one point along the contour by use of an attached fluorescent bead. For free microtubules, shape fluctuations were measured directly from fluorescence images of the microtubules themselves.

Intrinsic microtubule shapes measured by the latter method show a spectrum with a power law dependence reminiscent of thermal bending fluctuations, suggesting that bending energy is a limiting factor in the formation of intrinsic curvature. Mechanics measurements extracted from these data were however shown to suffer from systematic problems that were linked to the sample preparation. As these types of sample preparations have also been used by other authors [90, 10, 66], their results are called into question as well.

By contrast, all consistency checks for the first method presented evidence that it produces reliable results. Dynamics were considered carefully, and the effects of low-pass filtering, correlations, sampling, and measurement errors were taken into account. The author is not aware of any other study having reached this level of confirmation. This high precision assay was then used to study the effect of the bound nucleotide on the mechanical properties of microtubules.

The resulting data show that microtubules stabilized with the chemotherapy drug taxol have a stiffness or persistence length l_p that is a function of length, but is also subject to a lot of scatter, while microtubules polymerized with the GTP-analogue GMPCPP show a constant, but higher stiffness and very little scatter. The addition of taxol to GMPCPP microtubules produced only a small increase in stiffness. A lowering of the GMPCPP content, however, to a level just sufficient to avoid depolymerization during the measurements reproduced the behaviour seen for taxol microtubules. The difference observed between microtubules of the GMPCPP and the taxol/GDP

state must hence be a result of the nucleotide content, not the presence of taxol. Furthermore, at least in the length-regime of $\sim 4 - 11 \mu\text{m}$ probed for both conditions in the present study, taxol/GDP microtubules and GDP microtubules without taxol seem mechanically equivalent. Because GMPCPP microtubules are in turn thought to mimic the GTP state of tubulin, conclusions can be drawn from this data concerning the role of the nucleotide in microtubule assembly where the conversion of GTP to GDP in the microtubule lattice drives dynamic instability.

The stiffness measurements were confirmed by measurements of microtubule relaxation times, where deviations from the standard L^4 scaling predicted by the Wormlike Chain Model were obtained for conditions that showed a length-dependent stiffness. In addition, the relaxation times allowed for the extraction of the friction coefficients governing microtubule thermal fluctuations. All conditions showed friction contributions significantly higher than expected from hydrodynamic drag for microtubules shorter than $\sim 4 \mu\text{m}$. The increase can be explained by the additional presence of internal friction caused by dissipation inside the bending microtubule. Microtubules with a high GMPCPP content showed slightly higher internal friction than the other conditions.

A new polymer model, the Wormlike Bundle Model developed by Heussinger et al. [5, 6], was used to interpret the stiffness data. The model is based around the realization that microtubules are highly anisotropic structures, with very strong bonds longitudinally connecting dimers in one protofilament, but only loose lateral contacts between neighbouring protofilaments. It predicts a length-dependent stiffness with three different scaling regimes each dependent mainly on one type of contact within the microtubule lattice. A regime dominated by interprotofilament shear and exhibiting an L^2 scaling is predicted between the plateau l_p^0 for short microtubules, set by the sum of the persistence lengths of the constituent protofilaments, and the limit l_p^∞ for very long microtubules, set by protofilament extensibility.

In the case of taxol microtubules, it was argued that the data represent the regimes l_p^0 for microtubules shorter than $\sim 4 \mu\text{m}$ and the length-dependent regime dominated by interprotofilament shear for longer microtubules. The plateau $l_p^0 \approx 700 \mu\text{m}$ implies a protofilament persistence length of $l_p^{\text{PF}} \approx 55 \mu\text{m}$. For GMPCPP microtubules, the data most likely represent the plateau $l_p^\infty \approx 6400 \mu\text{m}$. The length-dependent regime for the stiffness of GMPCPP microtubules would then have to be shifted to lengths shorter than those covered in the present study, i.e., significantly shorter than $4.6 \mu\text{m}$. This constraint allows for an estimate of the minimum increase in interprotofilament shear coupling between taxol and GMPCPP microtubules, and by implication between the GDP and the GTP state. In the GTP state, the

lateral coupling between protofilaments must then be at least two orders of magnitude larger than in the GDP state.

In addition, the Wormlike Bundle Model predicts a strong dependence of the stiffness on variations in protofilament architecture because the latter can cause a supertwist of the microtubule lattice. Because microtubules polymerized with GTP are known to show more heterogeneity in architecture than GMPCPP microtubules, the model explains why more scatter in experimental results is found for the former.

5.2 Conclusions

To the knowledge of the author, the present study is unique in the range of potential error sources considered, the consistency tests undertaken, the precision achieved, and in being able to unambiguously show scatter to be the result of microtubule heterogeneity rather than measurement error.

While several previous studies have probed the effects of nucleotide content on microtubule mechanics and found an increased stiffness for GMPCPP microtubules, none of these were able to pinpoint the source of the observed differences. The current study presents the first evidence that the bound nucleotide has a drastic effect on interprotofilament bonds. This large effect is likely to be an important, but so far overlooked regulator in the still poorly understood polymerization dynamics of microtubules. Complementing studies that have analyzed the effect of the nucleotide on protofilament bending, this study fills an important gap towards a unified understanding of how microtubule assembly is controlled by nucleotide hydrolysis.

Using similar reasoning, it is shown that taxol does not affect interprotofilament bonds. Although taxol is one of the most commonly used chemotherapy drugs because of its stabilizing effect on microtubules in the mitotic spindle, the underlying mechanism of action is still debated. The result obtained here contributes to an understanding of taxol's functionality and may aid in the future development of optimized chemotherapy drugs.

The methodology introduced in this study is not only applicable to the problems considered here, but has the capability of addressing a broad range of analogous questions as will be discussed in Section 5.3.

Furthermore, this study for the first time analyzes the intrinsic curvatures of microtubules formed *in vitro* and finds that their spectrum mimics that of thermal bending fluctuations. The result has implications for the formation mechanism of intrinsic bends in microtubules which so far have received very little attention although they may yield relevant information on the polymerization kinetics of microtubules.

In addition, the present study is the first to show evidence of internal friction in microtubules that are unlikely to be affected by hydrodynamic coupling to surfaces, thereby firmly establishing the existence of internal dissipation in the thermal fluctuation dynamics of microtubules.

5.3 Outlook

Much of the interpretation presented here might be unambiguously confirmed if measurements could be performed on microtubules with a controlled architecture. While the use of biological templates such as axonemes is likely to favour 13-protofilament microtubules, the prevalence of lattice defect in non-nucleated microtubules suggests that transitions to different architectures can be expected along those microtubules, too. Inside cells, microtubules are generally limited to only the 13-protofilament architecture, so one might imagine performing measurements on microtubules directly extracted from cells. It is not obvious, however, how one could strip them of all associated proteins and at the same time prevent their depolymerization.

A challenging, but possibly rewarding strategy might be to directly measure the stiffness of microtubules inside cells. Because the action of molecular motors outweighs thermal fluctuations by two orders of magnitude for intracellular microtubules [130, 131], one would have to deplete ATP to disable the motors in order to perform the measurement.

A curious feature is the prediction of a possible length-dependent regime for the stiffness of GMPCPP microtubules at very short lengths. This regime is not accessible with the methods presented here because the time and spatial scales are too small. One promising technique capable of measurements on these scales would be light scattering-based position detection. If scattering signals turn out to be too challenging to obtain directly from microtubules, the scattering cross section could be increased by the attachment of small gold particles.

Finally, the methodology presented here could be adapted to address other research questions such as the effects of microtubule-associated proteins (MAPs). For instance, the binding mode of the Alzheimer-relevant τ protein to microtubules is still hotly debated [132], but the present technique might be able to resolve the question by pinpointing the mechanical effects of τ on the microtubule lattice.

References

- [1] W.J. Rasband. ImageJ. <http://imagej.nih.gov/ij/>, 1997-2011.
- [2] W Humphrey, A Dalke, and K Schulten. VMD: visual molecular dynamics. *J Mol Graph*, 14(1):33–38, 1996.
- [3] Rongxin Huang, Isaac Chavez, Katja M Taute, Branimir Lukić, Sylvia Jeney, Mark G Raizen, and Ernst-Ludwig Florin. Direct observation of the full transition from ballistic to diffusive brownian motion in a liquid. *Nat Phys*, 7(3):1–5, Mar 2011.
- [4] E Frey and K Kroy. Brownian motion: a paradigm of soft matter and biological physics. *Ann Phys*, 14:20, Feb 2005.
- [5] Claus Heussinger, Mark Bathe, and Erwin Frey. Statistical mechanics of semiflexible bundles of wormlike polymer chains. *Phys Rev Lett*, 99(4):048101, Jul 2007.
- [6] Claus Heussinger, Felix Schüller, and Erwin Frey. Statics and dynamics of the wormlike bundle model. *Phys Rev E*, 81(2):021904, Feb 2010.
- [7] Torsten Wittmann at Scripps Research Institute. <http://www.microscopyu.com/smallworld/gallery/contests/2003/index.html>, 2011.
- [8] N Mücke, L Kreplak, R Kirmse, T Wedig, H Herrmann, U Aepli, and J Langowski. Assessing the flexibility of intermediate filaments by atomic force microscopy. *J Mol Biol*, 335(5):1241–1250, 2004.
- [9] B.A. Alberts, A.B. Johnson, J. Lewis, M. Raff, K. Roberts, and P. Walter. *Molecular biology of the cell*. Garland, 4th edition, 2002.
- [10] F Gittes, B Mickey, J Nettleton, and J Howard. Flexural rigidity of microtubules and actin filaments measured from thermal fluctuations in shape. *J Cell Biol*, 120(4):923–934, 1993.
- [11] A Ott, M Magnasco, A Simon, and A Libchaber. Measurement of the persistence length of polymerized actin using fluorescence microscopy. *Phys Rev E*, 48(3), 1993.
- [12] S Goodin. Epothilones: Mechanism of action and biologic activity. *J Clin Oncol*, 22(10):2015–2025, Apr 2004.
- [13] A Desai. Kinetochore. *Curr Biol*, 10(14):R508, 2000.
- [14] XVIVO/Harvard College. The inner life of the cell. <http://www.xvivo.net/the-inner-life-of-the-cell/>, 2011.

- [15] P GaddumRosse, RJ Blandau, and JB Thiersch. Ciliary activity in the human and macaca nemestrina oviduct. *Am J Anat*, 138(2):269–275, 1973.
- [16] The Imaging Technology Group at University of Illinois at Urbana-Champaign. http://www.itg.uiuc.edu/technology/atlas/structures/nucleus/images/microtubules_03.tif, 2011.
- [17] Shaw Lab. <http://sites.bio.indiana.edu/~shawlab/>, 2011.
- [18] F Chang and S.G Martin. Shaping fission yeast with microtubules. *Cold Spring Harb Perspect Biol*, 1(1):a001347, 2009.
- [19] X Ma, D.W Ehrhardt, and W Margolin. Colocalization of cell division proteins FtsZ and FtsA to cytoskeletal structures in living Escherichia coli cells by using green fluorescent protein. *Proc Natl Acad Sci USA*, 93(23):12998, 1996.
- [20] H.P Erickson. Ftsz, a tubulin homologue in prokaryote cell division. *Trends Cells Biol*, 7(9):362–367, 1997.
- [21] IR Gibbons. Cilia and flagella of eukaryotes. *J Cell Biol*, 91(3):107s, 1981.
- [22] J McGrath and M Brueckner. Cilia are at the heart of vertebrate left-right asymmetry. *Curr Opin Genet Dev*, 13(4):385–392, 2003.
- [23] S. E Siegrist and C. Q Doe. Microtubule-induced cortical cell polarity. *Genes Dev*, 21(5):483–496, Mar 2007.
- [24] E M Mandelkow and E Mandelkow. Unstained microtubules studied by cryo-electron microscopy. substructure, supertwist and disassembly. *J Mol Biol*, 181(1):123–35, Jan 1985.
- [25] T Müller-Reichert, D Chrétien, F Severin, and A.A Hyman. Structural changes at microtubule ends accompanying GTP hydrolysis: Information from a slowly hydrolyzable analogue of GTP, guanylyl (α , β)methylenediphosphonate. *Proc Natl Acad Sci USA*, 95(7):3661, 1998.
- [26] J Richard Mcintosh, Ekaterina L Grishchuk, Mary K Morphew, Artem K Efremov, Kirill Zhudnikov, Vladimir A Volkov, Iain M Cheeseman, Arshad Desai, David N Mastronarde, and Fazly I Ataullakhanov. Fibrils connect microtubule tips with kinetochores: A mechanism to couple tubulin dynamics to chromosome motion. *Cell*, 135(2):322–333, Oct 2008.
- [27] M.K Gardner, A.J Hunt, H.V Goodson, and D.J Odde. Microtubule assembly dynamics: new insights at the nanoscale. *Curr Opin Cell Biol*, 20(1):64–70, 2008.
- [28] A Dimitrov, M Quesnoit, S Moutel, I Cantaloube, C Pous, and F Perez. Detection of GTP-tubulin conformation in vivo reveals a role for GTP remnants in microtubule rescues. *Science*, 322(5906):1353–1356, Nov 2008.
- [29] T Mitchison and M Kirschner. Dynamic instability of microtubule growth. *Nature*, 312(5991):237–42, Dec 1984.

- [30] A Desai and T.J Mitchison. Microtubule polymerization dynamics. *Annu Rev Cell Dev Biol*, 13(1):83–117, 1997.
- [31] D Panda, HP Miller, and L Wilson. Determination of the size and chemical nature of the stabilizing "cap" at microtubule ends using modulators of polymerization dynamics. *Biochemistry*, 41(5):1609–1617, Jan 2002.
- [32] M.F Carlier and D Pantaloni. Kinetic analysis of cooperativity in tubulin polymerization in the presence of guanosine di-or triphosphate nucleotides. *Biochemistry*, 17(10):1908–1915, 1978.
- [33] Michael Caplow and Lanette Fee. Concerning the chemical nature of tubulin subunits that cap and stabilize microtubules. *Biochemistry*, 42(7):2122–6, Feb 2003.
- [34] Jacob W. J Kerssemakers, E Laura Munteanu, Liedewij Laan, Tim L Noetzel, Marcel E Janson, and Marileen Dogterom. Assembly dynamics of microtubules at molecular resolution. *Nature*, 442(7103):709–712, Aug 2006.
- [35] Henry T Schek, Melissa K Gardner, Jun Cheng, David J Odde, and Alan J Hunt. Microtubule assembly dynamics at the nanoscale. *Curr Biol*, 17(17):1445–55, Sep 2007.
- [36] E Nogales, M Whittaker, R A Milligan, and K H Downing. High-resolution model of the microtubule. *Cell*, 96(1):79–88, Jan 1999.
- [37] E Nogales, S G Wolf, and K H Downing. Structure of the alpha beta tubulin dimer by electron crystallography. *Nature*, 391(6663):199–203, Jan 1998.
- [38] L.G Tilney, J Bryan, D.J Bush, K Fujiwara, M.S Mooseker, D.B Murphy, and D.H Snyder. Microtubules: evidence for 13 protofilaments. *J Cell Biol*, 59(2):267, 1973.
- [39] M Chalfie and J N Thomson. Structural and functional diversity in the neuronal microtubules of *Caenorhabditis elegans*. *J Cell Biol*, 93(1):15–23, Apr 1982.
- [40] M M Mogensen and J B Tucker. Taxol influences control of protofilament number at microtubule-nucleating sites in *Drosophila*. *J Cell Sci*, 97 (Pt 1):101–7, Sep 1990.
- [41] IR Gibbons and AV Grimstone. On flagellar structure in certain flagellates. *J Biophy Biochem Cytol*, 7(4):697, 1960.
- [42] K Hu, D. S Roos, and J. M Murray. A novel polymer of tubulin forms the conoid of *Toxoplasma gondii*. *J Cell Biol*, 156(6):1039–1050, Mar 2002.
- [43] D Chrétien and R.H Wade. New data on the microtubule surface lattice. *Biol Cell*, 71(1-2):161–174, 1991.
- [44] D Chrétien, F Metoz, F Verde, E Karsenti, and R H Wade. Lattice defects in microtubules: protofilament numbers vary within individual microtubules. *J Cell Biol*, 117(5):1031–40, Jun 1992.

- [45] RH Wade and D Chrétien. Cryoelectron microscopy of microtubules. *J Struct Biol*, 110(1):1, 1993.
- [46] I Arnal and R.H Wade. How does taxol stabilize microtubules? *Curr Biol*, 5(8):900–908, 1995.
- [47] A A Hyman, D Chrétien, I Arnal, and R H Wade. Structural changes accompanying GTP hydrolysis in microtubules: information from a slowly hydrolyzable analogue guanylyl-(α,β)-methylene-diphosphonate. *J Cell Biol*, 128(1-2):117–25, Jan 1995.
- [48] Iva M Tolić-Nørrelykke. Push-me-pull-you: how microtubules organize the cell interior. *Eur Biophys J*, 37(7):1271–1278, Sep 2008.
- [49] O Kratky and G Porod. Röntgenuntersuchung gelöster fadenmoleküle. *Recueil des Travaux Chimiques des Pays-Bas*, 68:1106–1122, Mar 1949.
- [50] N Saitô, K Takahashi, and Y Yunoki. The statistical mechanical theory of stiff chains. *J Phys Soc Jpn*, 22(1):219–226, 1967.
- [51] K Soda. Dynamics of stiff chains. i. equation of motion. *J Phys Soc Jpn*, 35(3):866–870, 1973.
- [52] SR Aragon and R Pecora. Dynamics of wormlike chains. *Macromolecules*, 18(10):1868–1875, 1985.
- [53] CH Wiggins, D Riveline, A Ott, and RE Goldstein. Trapping and wiggling: Elasto-hydrodynamics of driven microfilaments. *Biophys J*, 74(2):1043–1060, 1998.
- [54] M Janson and M Dogterom. A bending mode analysis for growing microtubules: Evidence for a velocity-dependent rigidity. *Biophys J*, 87(4):2723–2736, Oct 2004.
- [55] K Kroy and E Frey. Dynamic scattering from solutions of semiflexible polymers. *Phys Rev E*, 55(3):3092–3101, Jan 1997.
- [56] Erwin Frey. personal communication, 2007.
- [57] L Cassimeris, D Gard, PT Tran, and H.P Erickson. Xmap215 is a long thin molecule that does not increase microtubule stiffness. *J Cell Sci*, 114(16):3025–3034, 2001.
- [58] Azam Gholami, Jan Wilhelm, and Erwin Frey. Entropic forces generated by grafted semiflexible polymers. *Phys Rev E*, 74(4):1–21, Oct 2006.
- [59] Francesco Pampaloni, Gianluca Lattanzi, Alexandr Jonás, Thomas Surrey, Erwin Frey, and Ernst-Ludwig Florin. Thermal fluctuations of grafted microtubules provide evidence of a length-dependent persistence length. *Proc Natl Acad Sci USA*, 103(27):10248–53, Jul 2006.
- [60] Katja M Taute, Francesco Pampaloni, and Ernst-Ludwig Florin. Extracting the mechanical properties of microtubules from thermal fluctuation measurements on an attached tracer particle. *Methods Cell Biol*, 95:601–615, Jan 2010.

- [61] Shoko Yamazaki, Tadakazu Maeda, and Taiko Miki-Noumura. Flexural rigidity of singlet microtubules estimated from statistical analysis of fluctuating images. *Biological Functions of Microtubules and Related Structures*, Chapter 5:41–48, Apr 1982.
- [62] J Mizushima-Sugano, T Maeda, and T Miki-Noumura. Flexural rigidity of singlet microtubules estimated from statistical analysis of their contour lengths and end-to-end distances. *Biochim Biophys Acta*, 755:257–262, Jan 1983.
- [63] Toru Takasone, Saulius Juodkazis, Yuji Kawagishi, Akira Yamaguchi, Shigeki Matsuo, Hitoshi Sakakibara, Haruto Nakayama, and Hiroaki Misawa. Flexural rigidity of a single microtubule. *Jpn J Appl Phys*, 41:3015–3019, May 2002.
- [64] H Felgner, R Frank, and M Schliwa. Flexural rigidity of microtubules measured with the use of optical tweezers. *J Cell Sci*, 109:509–516, Jan 1996.
- [65] M Kikumoto, M Kurachi, V Tosa, and H Tashiro. Flexural rigidity of individual microtubules measured by a buckling force with optical traps. *Biophys J*, 90(5):1687–1696, Mar 2006.
- [66] B Mickey and J Howard. Rigidity of microtubules is increased by stabilizing agents. *J Cell Biol*, 130(4):909–917, 1995.
- [67] R B Dye, S P Fink, and R C Williams. Taxol-induced flexibility of microtubules and its reversal by MAP-2 and Tau. *J Biol Chem*, 268(10):6847–50, Apr 1993.
- [68] P Venier, A C Maggs, M F Carlier, and D Pantaloni. Analysis of microtubule rigidity using hydrodynamic flow and thermal fluctuations. *J Biol Chem*, 269(18):13353–60, May 1994.
- [69] M Kurachi, M HOSHI, and H Tashiro. Buckling of a single microtubule by optical trapping forces: direct measurement of microtubule rigidity. *Cell Motil Cytoskel*, 30(3):221–8, Jan 1995.
- [70] A Kis, S Kasas, B Babic, AJ Kulik, W Benoit, GAD Briggs, C Schonenberger, S Catsicas, and L Forro. Nanomechanics of microtubules. *Phys Rev Lett*, 89(24):248101, Jan 2002.
- [71] Katja Taute. Mechanics of individual biofilaments. Master’s Thesis, Universität Leipzig, 2006.
- [72] BL Frey and RM Corn. Covalent attachment and derivatization of poly(L-lysine) monolayers on gold surfaces as characterized by polarization-modulation FT-IR spectroscopy. *Anal Chem*, 68:3187–3193, 1996.
- [73] N Patel, MC Davies, M Hartshorne, RJ Heaton, CJ Roberts, SJB Tendler, and PM Williams. Immobilization of protein molecules onto homogeneous and mixed carboxylate-terminated self-assembled monolayers. *Langmuir*, 13(24):6485–6490, 1997.

- [74] Jerker Widengren, Andriy Chmyrov, Christian Eggeling, Per-Ake Löfdahl, and Claus A M Seidel. Strategies to improve photostabilities in ultrasensitive fluorescence spectroscopy. *J Phys Chem A*, 111(3):429–40, Jan 2007.
- [75] GP Vigers, M Coue, and JR McIntosh. Fluorescent microtubules break up under illumination. *J Cell Biol*, 107(3):1011–1024, 1988.
- [76] H Guo, C Xu, C Liu, E Qu, M Yuan, Z Li, B Cheng, and D Zhang. Mechanism and dynamics of breakage of fluorescent microtubules. *Biophys J*, 90(6):2093–2098, Mar 2006.
- [77] Margit Foss, Buck W. L Wilcox, G. Bradley Alsop, and Dahong Zhang. Taxol crystals can masquerade as stabilized microtubules. *PLoS ONE*, 3(1):e1476, Jan 2008.
- [78] A A Hyman, S Salser, D N Drechsel, N Unwin, and T J Mitchison. Role of GTP hydrolysis in microtubule dynamics: information from a slowly hydrolyzable analogue, GMPCPP. *Mol Biol Cell*, 3(10):1155–67, Oct 1992.
- [79] T.J. Mitchison. <http://mitchison.med.harvard.edu/protocols/poly.html#V.%20%20GMPCPP%20Polymerization>, 2011.
- [80] M.R Mejillano and R.H Himes. Binding of guanine nucleotides and Mg^{2+} to tubulin with a nucleotide-depleted exchangeable site. *Arch Biochem Biophys*, 291(2):356–362, 1991.
- [81] Vincent Associates. www.uniblitz.com, 2011.
- [82] WP Wong and K Halvorsen. The effect of integration time on fluctuation measurements: calibrating an optical trap in the presence of motion blur. *Optics Express*, 14(25):12517–12531, 2006.
- [83] Katja M Taute, Francesco Pampaloni, Erwin Frey, and Ernst-Ludwig Florin. Microtubule dynamics depart from the wormlike chain model. *Phys Rev Lett*, 100(2):028102, Jan 2008.
- [84] R Yasuda, H Miyata, and K Kinosita. Direct measurement of the torsional rigidity of single actin filaments. *J Mol Biol*, 263(2):227–36, Oct 1996.
- [85] Thierry Savin and Patrick S Doyle. Role of a finite exposure time on measuring an elastic modulus using microrheology. *Phys Rev E*, 71(4):1–6, Apr 2005.
- [86] Thierry Savin and Patrick S Doyle. Static and dynamic errors in particle tracking microrheology. *Biophys J*, 88(1):623–638, Dec 2008.
- [87] Ilya N. Bronstein, Konstantin A. Semandj Jew, Gerhard Musiol, and Heiner Mühlig. *Taschenbuch der Mathematik*. Verlag Harri Deutsch, 5th edition, 2000.
- [88] H Flyvbjerg and HG Petersen. Error estimates on averages of correlated data. *J Chem Phys*, 91(1):461, 1989.

- [89] M.J Saxton and K Jacobson. Single-particle tracking: applications to membrane dynamics. *Annu Rev Biophys Biomol Struct*, 26(1):373–399, 1997.
- [90] C Brangwynne, G Koenderink, E Barry, Z Dogic, F Mackintosh, and D Weitz. Bending dynamics of fluctuating biopolymers probed by automated high-resolution filament tracking. *Biophys J*, 93(1):346–359, Jul 2007.
- [91] A Hunt, F Gittes, and J Howard. The force exerted by a single kinesin molecule against a viscous load. *Biophys J*, 67:766–781, Jan 1994.
- [92] Stephen P. Timoshenko. On the correction factor for shear of the differential equation for transverse vibrations of bars of uniform cross-section. *Philosophical Magazine*, XLI:744–746, 1921.
- [93] A Ptak, S Takeda, C Nakamura, J Miyake, M Kageshima, S.P Jarvis, and H Tokumoto. Modified atomic force microscope applied to the measurement of elastic modulus for a single peptide molecule. *J Appl Phys*, 90:3095, 2001.
- [94] F.K Ko, S Kawabata, M Inoue, M Niwa, S Fossey, and J.W Song. Engineering properties of spider silk. *Mater Res Soc Symp Proc*, 702:U1.4.1, 2001.
- [95] M. G. L Van Den Heuvel, S Bolhuis, and C Dekker. Persistence length measurements from stochastic single-microtubule trajectories. *Nano Lett*, 7(10):3138–3144, Oct 2007.
- [96] M G L Van den Heuvel, M P de Graaff, and C Dekker. Microtubule curvatures under perpendicular electric forces reveal a low persistence length. *Proc Natl Acad Sci USA*, 105(23):7941–6, Jun 2008.
- [97] RG Cox. The motion of long slender bodies in a viscous fluid part 1. general theory. *J Fluid Mech*, 44(04):791–810, 1970.
- [98] MG Poirier and JF Marko. Effect of internal friction on biofilament dynamics. *Phys Rev Lett*, 88(22):228103, 2002.
- [99] Kenji Kawaguchi and Atsushi Yamaguchi. Temperature dependence rigidity of non-taxol stabilized single microtubules. *Biochem Biophys Res Commun*, 402(1):66–69, Nov 2010.
- [100] M Caplow, RL Ruhlen, and J Shanks. The free energy for hydrolysis of a microtubule-bound nucleotide triphosphate is near zero: all of the free energy for hydrolysis is stored in the microtubule lattice. *J Cell Biol*, pages 779–788, 1994.
- [101] C Elie-Caille, F Severin, J Helenius, J Howard, D.J Muller, and A.A Hyman. Straight GDP-tubulin protofilaments form in the presence of taxol. *Curr Biol*, 17(20):1765–1770, 2007.
- [102] Vincent VanBuren, Lynne Cassimeris, and David J Odde. Mechanochemical model of microtubule structure and self-assembly kinetics. *Biophys J*, 89(5):2911–26, Nov 2005.

- [103] Hong-Wei Wang and Eva Nogales. Nucleotide-dependent bending flexibility of tubulin regulates microtubule assembly. *Nature*, 435(7044):911–915, Jun 2005.
- [104] D Chrétien and S D Fuller. Microtubules switch occasionally into unfavorable configurations during elongation. *J Mol Biol*, 298(4):663–76, May 2000.
- [105] E M Mandelkow, E Mandelkow, and R A Milligan. Microtubule dynamics and microtubule caps: a time-resolved cryo-electron microscopy study. *J Cell Biol*, 114(5):977–91, Aug 1991.
- [106] Raimond B G Ravelli, Benoît Gigant, Patrick A Curmi, Isabelle Jourdain, Sylvie Lachkar, André Sobel, and Marcel Knossow. Insight into tubulin regulation from a complex with colchicine and a stathmin-like domain. *Nature*, 428(6979):198–202, Mar 2004.
- [107] D Chrétien, S D Fuller, and E Karsenti. Structure of growing microtubule ends: two-dimensional sheets close into tubes at variable rates. *J Cell Biol*, 129(5):1311–28, Jun 1995.
- [108] Eva Nogales and Hong-Wei Wang. Structural mechanisms underlying nucleotide-dependent self-assembly of tubulin and its relatives. *Curr Opin Struct Biol*, 16(2):221–9, Mar 2006.
- [109] RM Buey, JF Diaz, and JM Andreu. The nucleotide switch of tubulin and microtubule assembly: A polymerization-driven structural change. *Biochemistry*, 45(19):5933–5938, Jan 2006.
- [110] Luke M Rice, Elizabeth A Montabana, and David A Agard. The lattice as allosteric effector: structural studies of $\alpha\beta$ - and γ -tubulin clarify the role of GTP in microtubule assembly. *Proc Natl Acad Sci USA*, 105(14):5378–83, Apr 2008.
- [111] R Melki and M F Carlier. Thermodynamics of tubulin polymerization into zinc sheets: assembly is not regulated by GTP hydrolysis. *Biochemistry*, 32(13):3405–13, Apr 1993.
- [112] R D Vale, C M Coppin, F Malik, F J Kull, and R A Milligan. Tubulin GTP hydrolysis influences the structure, mechanical properties, and kinesin-driven transport of microtubules. *J Biol Chem*, 269(38):23769–75, Sep 1994.
- [113] Huilin Li, David J DeRosier, William V Nicholson, Eva Nogales, and Kenneth H Downing. Microtubule structure at 8Å resolution. *Structure*, 10(10):1317–28, Sep 2002.
- [114] J Löwe, H Li, K H Downing, and E Nogales. Refined structure of $\alpha\beta$ -tubulin at 3.5Å resolution. *J Mol Biol*, 313(5):1045–57, Nov 2001.
- [115] Kathleen M Munson, Philipose G Mulugeta, and Zachary J Donhauser. Enhanced mechanical stability of microtubules polymerized with a slowly hydrolyzable nucleotide analogue. *J Phys Chem B*, 111(19):5053–5057, May 2007.

- [116] PJ de Pablo, IAT Schaap, FC MacKintosh, and CF Schmidt. Deformation and collapse of microtubules on the nanometer scale. *Phys Rev Lett*, 91(9):98101–98101, 2003.
- [117] Daniel J Needleman, Miguel A Ojeda-Lopez, Uri Raviv, Kai Ewert, Jayna B Jones, Herbert P Miller, Leslie Wilson, and Cyrus R Safinya. Synchrotron x-ray diffraction study of microtubules buckling and bundling under osmotic stress: a probe of interprotofilament interactions. *Phys Rev Lett*, 93(19):198104, Nov 2004.
- [118] Arpita Mitra and David Sept. Taxol allosterically alters the dynamics of the tubulin dimer and increases the flexibility of microtubules. *Biophys J*, 95(7):3252–3258, Jan 2008.
- [119] JM Andreu, J Garcia de Ancos, F.J Medrano, R Gil, J.F Diaz, E Nogales, E Towns-Andrews, E Pantos, and J Bordas. Twelve protofilament taxol-induced microtubules assembled from purified tubulin. A synchrotron x-ray scattering study in comparison with glycerol- and MAP-induced microtubules. *The living cell in four dimensions. AIP conference proceedings.*, 226:160–169, Oct 1991.
- [120] JF Diaz, JM Valpuesta, P Chacon, G Diakun, and JM Andreu. Changes in microtubule protofilament number induced by taxol binding to an easily accessible site. *J Biol Chem*, 273(50):33803–33810, 1998.
- [121] S Ray, E Meyhöfer, R A Milligan, and J Howard. Kinesin follows the microtubule’s protofilament axis. *J Cell Biol*, 121(5):1083–93, May 1993.
- [122] T Shida, J. G Cueva, Z Xu, M. B Goodman, and M. V Nachury. The major α -tubulin K40 acetyltransferase α TAT1 promotes rapid ciliogenesis and efficient mechanosensation. *Proc Natl Acad Sci USA*, 107(50):21517–21522, Dec 2010.
- [123] Adel Aschi, Patrick Calmettes, Mohamed Daoud, Roger Douillard, and Abdelhafidh Gharbi. Micelle formation in beta-casein solutions. *Polymer*, 50(25):6024–6031, Nov 2009.
- [124] R Bhat and S.N Timasheff. Steric exclusion is the principal source of the preferential hydration of proteins in the presence of polyethylene glycols. *Protein Sci*, 1(9):1133, 1992.
- [125] http://www.brocku.ca/researchers/peter_rand/osmotic/osfile.html.
- [126] T Dimitrova and F Leal-Calderon. Colloid forces in model food-type emulsions. *Trends in Colloid and Interface Science XIV*, pages 156–160, 2000.
- [127] DJ Jeffrey and Y Onishi. The slow motion of a cylinder next to a plane wall. *The Quarterly Journal of Mechanics and Applied Mathematics*, 34(2):129, 1981.
- [128] J C Kurz and R C Williams. Microtubule-associated proteins and the flexibility of microtubules. *Biochemistry*, 34(41):13374–80, Oct 1995.
- [129] K Kawaguchi, S Ishiwata, and T Yamashita. Temperature dependence of the flexural rigidity of single microtubules. *Biochem Biophys Res Commun*, 366(3):637–642, 2008.

- [130] A.D Bicek, E Tuzel, A Demtchouk, M Uppalapati, W.O Hancock, D.M Kroll, and D.J Odde. Anterograde microtubule transport drives microtubule bending in ilc-pk1 epithelial cells. *Mol Biol Cell*, 20(12):2943, 2009.
- [131] C.P Brangwynne, FC MacKintosh, and D.A Weitz. Force fluctuations and polymerization dynamics of intracellular microtubules. *Proc Natl Acad Sci USA*, 104(41):16128, 2007.
- [132] V Makrides, M.R Massie, S.C Feinstein, and J Lew. Evidence for two distinct binding sites for tau on microtubules. *Proc Natl Acad Sci USA*, 101(17):6746, 2004.

Appendix A

Reagents

name	supplier	product code
unlabeled bovine tubulin	C	TL238
unlabeled porcine tubulin	C	T240
rhodamine bovine tubulin	C	TL331M
rhodamine porcine tubulin	C	TL590M
biotinilated bovine tubulin	C	T333
biotinilated porcine tubulin	C	T333P
PIPES free acid	SA	P6757
EGTA	SA	E4378
1M MgCl ₂	SA	M1028
KOH pellets	F	P250-500
GTP	SA	G5884
taxol	SA	T1912
DMSO	SA	276855
ammonia 30%	F	A669S500
hydrogen peroxide 30%	F	H325100
11 MUA	SA	450561
NHS	SA	130672
EDC	SA	E7750
D-glucose	F	D16
glucose oxidase	SA	G2133
catalase	SA	C40
hemoglobin	SA	H2500
mPEG-SVA	L	MPEG-SVA-5000-1g
acetone	F	A949
sodium bicarbonate	F	BP328
APTES	SA	440140
GMPCPP	JB	NU-405L
paraffin	F	P31
lanolin	F	S80047
casein	SA	C6905

Table A.1: List of reagents. C: Cytoskeleton Inc, Denver, CO; SA: Sigma-Aldrich Inc, St. Louis, MO; F: Fisher Scientific, Hanover Park, IL; L: Laysan Bio, Arab, AL; JB: Jena Bioscience, Jena, Germany.

Bibliographische Beschreibung:

Taute, Katja Marie

Microtubule mechanics and the implications for their assembly

Universität Leipzig, Dissertation

119 S., 132 Lit., 62 Abb.

Referat:

Mikrotubuli sind Proteinpolymere und Teil des Zytoskeletts eukaryotischer Zellen. Sowohl ihre Polymerisierungsdynamik, welche durch das gebundene Nukleotid GTP und seine Hydrolyse zu GDP reguliert wird, wie auch ihre mechanischen Eigenschaften sind essentiell für ihre Rolle in diversen Zellfunktionen. Trotz ihrer biologischen Relevanz und jahrzehntelanger Forschungen sind diese beiden Eigenschaften von Mikrotubuli bisher noch immer nicht vollkommen verstanden.

In der vorliegenden Arbeit werden hochpräzise Messungen der Mechanik von Mikrotubuli mit verschiedenem Nukleotidgehalt vorgestellt. Steifigkeitsmessungen werden bestätigt durch Relaxationszeitmessungen und diverse Konsistenztests.

Diese resultierenden Daten zeigen eine langenabhängige Biegesteifigkeit für mit Taxol stabilisierte Mikrotubuli. Mit dem nicht hydrolysierbaren GTP-Analog GMPCPP polymerisierte Mikrotubuli weisen dagegen eine konstante, deutlich höhere Steifigkeit auf. Eine Minderung des GMPCPP-Gehaltes stellt allerdings das bei Taxolmikrotubuli beobachtete Verhalten wieder her.

Unter Heranziehung neuer Polymermodelle wird abgeleitet, dass das gebundene Nukleotid einen starken Effekt hat auf die Steifigkeit der lateralen Kontakte zwischen den Protofilamenten, aus denen sich Mikrotubuli zusammensetzen. Physikalische und biologische Implikationen werden diskutiert.

